Diffusion of proteins inside crowded structures generated using microemulsions

Dissertation

zur Erlangung des akademischen Grades eines Doktors der Naturwissenschaften (Dr. rer. nat.) im Fach Chemie an der Fakultät für Biologie, Chemie und Geowissenschaften der Universität Bayreuth

vorgelegt von

Ralph Neubauer

geboren in Eschenbach

Bayreuth, der 27. Februar 2013

Die vorliegende Arbeit wurde in der Zeit von August 2009 bis Januar 2013 an der Universität Bayreuth am Lehrstuhl für Physikalische Chemie I unter Betreuung von Herrn Prof. Dr. Thomas Hellweg angefertigt.

Vollständiger Abdruck der von der Fakultät für Biologie, Chemie und Geowissenschaften der Universität Bayreuth genehmigten Dissertation zur Erlangung des akademischen Grades eines Doktors der Naturwissenschaften (Dr. rer. nat).

Dissertation eingereicht am: 27.02.2013
Zulassung durch die Prüfungskommission: 13.03.2013
Wissenschaftliches Kolloquium: 28.10.2013

Amtierender Dekan:
Prof. Dr. Rhett Kempe

Prüfungsausschuss:
Prof. Dr. Stephan Förster (Erstgutachter)
Prof. Dr. Thomas Hellweg (Zweitgutachter)
Prof. Dr. Jürgen Senker (Vorsitz)
Prof. Dr. Werner Köhler

Contents

1 Summary

Microemulsions are thermodynamically stable mixtures of water, oil and surfactant. In the case of microemulsions based on sugar surfactants a cosurfactant as an additional component is necessary, most often a short-chain alcohol. In this thesis mainly pure surfactants are used. The focus is on *n*-nonyl-β-d-maltosid and *n*-dodecyl-β-d-maltosid as model systems for microemulsions based on technical grade surfactants.

Depending on the ratio of the components microemulsions form different structures. In the bicontinuous phase continuous oil and water domains are present separated by a surfactant/cosurfactant film. At higher surfactant amounts the bicontinuous structure passes over to a droplet phase. The size of these structures is in the scale of up to 100 nm, therefore microemulsions look transparent for the human eye.

Bicontinuous microemulsions are a promising carrier medium for decontamination applications. Chemical warfare agents are mainly lipophilic, in contrast degradation agents are hydrophilic. A microemulsion is able to solubilize lipophilic and hydrophilic molecules. At the interface the warfare agent is close to the degradation agent and can be eliminated.

The protein diisopropyl-fluorophosphatase (DFPase) is a promising candidate for decontamination applications and is able to degrade different warfare agents. Therefore, the knowledge of the dynamics and properties of enzymes inside a bicontinuous structure is of big importance. In this thesis different microemulsion systems based on C_9G_2 or $C_{12}G_2$, water, cyclohexane and 1-pentanol are systematically characterized by X-ray and neutron scattering experiments. By using an improved Green Fluorescent Protein (GFP+) as a counterpart of DFPase with a similar size, the diffusion inside a microemulsion can be studied with the fluorescence correlation spectroscopy (FCS) method. Here, fluorescent impurities in the used components are a problem. By the choice of a suitable concentration of GFP+ and regarding the dynamics of the microemulsion structure, it could be shown that the protein is able to move inside the microemulsion structure. Hence, microemulsions are interesting model systems to produce crowding effects in a controlled way. This is probably the most important result of this thesis. In the C_9G_2 system a bicontinuous phase is present. At small oil/water ratios Φ with a high water amount big water domains exist with length scales of approximately 10 nm, which allows protein diffusion. With increasing oil/water ratio the protein diffusion is more and more hindered. This results in an

increase of the diffusion time and a decrease of the anomalous diffusion exponent. At even higher oil/water ratios the diffusion of the protein is nearly identical with the microemulsion dynamics. The length scales are too small to allow protein diffusion, therefore it is stuck in the structure.

The $C_{12}G_2$ system shows an oil-in-water droplet phase which also hinders the GFP+ diffusion due to crowding effects. For small oil/water ratios nearly free diffusion is present, at $\Phi = 0.3 - 0.5$ the diffusion is hindered, the anomalous diffusion exponent decreases. At $\Phi = 0.6$ the protein diffusion reflects the microemulsion dynamics. Again at higher values of Φ, GFP+ is stuck in the structure because of the high oil fraction.

Two microemulsion systems with different structures were studied, which allow protein diffusion due to their length scales. These results are related to applications: For the formulation of decontamination media the knowledge of the dynamics of the decontaminating protein is of importance. Moreover, pure surfactants can be easily replaced by technical grade surfactants. This enables cheap systems for a production-scale. Furthermore, the situation in living cells can be simulated by a microemulsion structure, where a confined diffusion is present as well.

Additional neutron spin echo experiments emphasize the complexity when studying a microemulsion system based on four components. The contrast matching procedure, which is necessary when protein dynamics inside the microemulsion are investigated, is very difficult and requires a high amount of surfactant.

2 Zusammenfassung

Mikroemulsionen sind thermodynamisch stabile Mischungen aus Öl, Wasser und Tensid. Im Falle von Mikroemulsionen auf Zuckertensidbasis wird zusätzlich ein Cotensid benötigt, in den meisten Fällen ein kurzkettiger Alkohol. In dieser Arbeit werden überwiegend reine Tenside verwendet, das Hauptaugenmerk liegt dabei auf *n*-Nonyl-β-d-Maltosid (C_9G_2) und *n*-Dodecyl-β-d-Maltosid ($C_{12}G_2$) als Modellsystem für Mikroemulsionssysteme mit technischen Zuckertensiden.

Mikroemulsionen können je nach Zusammensetzung der Komponenten verschiedene Strukturen ausbilden. In der bikontinuierlichen Phase liegen kontinuierliche Öl- und Wasserdomänen vor, die durch einen Tensidfilm getrennt werden. Bei höheren Tensidanteilen geht die bikontinuierliche Struktur in eine Öl-in-Wasser bzw. Wasser-in-Öl Tröpfchenstruktur über, je nach vorliegendem Öl/Wasserverhältnis. Die Größenordnung von Strukturen in Mikroemulsionssystemen liegt im Bereich von einigen nm bis zu 100 nm, weswegen sie optisch transparent erscheinen.

Bikontinuierliche Mikroemulsionen sind ein vielversprechendes Trägermittel für Dekontaminationsanwendungen. Chemische Kampfstoffe sind überwiegend lipophiler Natur, wohingegen übliche Dekontaminationsmittel hydrophilen Charakter besitzen. Eine Mikroemulsion ist in der Lage, sowohl liphophile als auch hydrophile Moleküle zu solubilisieren. An der Grenzfläche können Kampfstoff und Dekontaminationsmittel interagieren, der Kampfstoff kann somit abgebaut werden.

Das Protein DFPase ist ein aussichtsreicher Kandidat für Dekontaminationsanwendungen und ist fähig, verschiedene Kampfstoffe unschädlich zu machen.

Deswegen ist es von großem Interesse, die Dynamiken und Eigenschaften dieses Enzyms innerhalb einer bikontinuierlichen Struktur zu erforschen. In dieser Arbeit werden zwei verschiedene Mikroemulsionssysteme basierend auf C_9G_2 bzw. $C_{12}G_2$, Wasser, Cyclohexan und 1-Pentanol mit Röntgen- und Neutronenstreuung systematisch charakterisiert. Mit Hilfe des grün fluoreszierenden Proteins in einer verbesserten Version mit erhöhter Fluoreszenz (GFP+) als Pendant zur DFPase mit ähnlicher Größe kann die Diffusion eines Tracer-Proteins mittels Fluoreszenz-Korrelations-Spektroskopie innerhalb einer Mikroemulsion untersucht werden. Dabei stellen fluoreszierende Verunreinigungen in den verwendeten Komponenten ein Problem dar. Durch geeignete Wahl der Konzentration von GFP+ in der Mikroemulsion und durch Berücksichtigen

der Eigendynamik der Mikroemulsion konnte gezeigt werden, dass sich das Protein innerhalb der Mikroemulsionsstruktur bewegt. Damit stellen Mikroemulsionen interessante Systeme dar, um in kontrollierter Weise “crowding” Effekte zu produzieren und zu untersuchen. Dies ist vermutlich das wichtigste Ergebnis der vorliegenden Arbeit.

Im C_9G_2-System liegt eine bikontinuierliche Phase vor. Bei geringen Öl/Wasser-Verhältnissen Φ mit hohem Wasseranteil existieren große Wasserdomänen mit Längenskalen von ca. 10 nm, die eine Proteindiffusion erlauben. Für steigende Φ wird durch kleinere Wasserdomänen die Proteindiffusion zunehmend eingeschränkt, was sich in einer Vergrößerung der Diffusionszeiten und in einer Verringerung des anormalen Diffusionsexponenten zeigt. Bei höheren Φ ist die Diffusionszeit nahezu identisch mit der Dynamik der Mikroemulsion. Dies ist mit dem Festsitzen des Proteins in der Mikroemulsionsstruktur zu erklären, die Längenskalen sind zu gering für eine selbstständige Diffusion.

Im $C_{12}G_2$-System hat man eine Öl-in-Wasser Tröpfchenphase, die wiederum die GFP+-Diffusion innerhalb der kontinuierlichen Wasserphase durch Crowding-Effekte einschränkt. Beobachtet man bei geringen Φ noch nahezu ungehinderte Diffusion, wird diese ab Φ 0.5 erheblich eingeschränkt, um dann ab Φ 0.6 in eine der Mikroemulsionsdynamik entsprechende Diffusion überzugehen. Somit wurden in der vorliegenden Arbeit zwei Modellsysteme mit unterschiedlichem Strukturverhalten erforscht, die aufgrund ihrer Längenskalen die Diffusion des verwendeten Proteins GFP+ erlauben. Diese Ergebnisse sind relevant für verschiedene Anwendungen: Für die Formulierung von Dekontaminationsmedien ist die Kenntnis der Dynamik des dekontaminierenden Proteins von großer Wichtigkeit. Außerdem können reine Tenside leicht durch technische erstezt werden, dies ermöglicht günstige Systeme für einen größeren Produktionsmaßstab. Darüberhinaus kann mit Mikroemulsionen die Situation innerhalb Zellen simuliert werden, wo ebenfalls oft eine eingeschränkte Proteindiffusion vorliegt.

Zusätzlich durchgeführte Neutronen-Spinecho Messungen verdeutlichen die Komplexität von Untersuchungen an einem Zuckertensid-Mikroemulsionssystem mit vier Komponenten. Dabei ist die nötige Angleichung des Streukontrasts durch Variation der Deuterierung der Komponenten überaus kompliziert.

3 Introduction

A first look at the word “microemulsions” doesn’t tell the real nature of the structure of such systems. In principle emulsions consist of two in-miscible fluids (oil and water). With the help of surfactants, oil-in-water or water-in-oil droplets can be formed, separated by a surfactant film. In the case of microemulsions one would suppose, that these droplets exist on a micrometer scale. But in reality the structures are three orders of magnitude smaller, for instance several nanometers for sugar surfactant microemulsions. And, moreover, the phase behavior is much more complex - there are more than just droplets. Such a rich phase behavior is the base for different kinds of applications and interesting phenomena. In 1948 Winsor *et al.* discussed [1] the phase behavior of microemulsion systems, while they launched the term “Winsor I...I” phases, which characterizes the one-, two- and three-phase occurrence.

The expression “micro emulsion” goes back to 1959 when it was first introduced by Schulman *et al.* [2] and the research on these systems started in 1943 [3] when a dispersed phase with sub-microscopic micelles was discussed. The phase behavior of microemulsions was observed in detail in the 1960s and 1970s by Friberg *et al.* [4–6] and Shimoda *et al.* [7–9].

The commercial use of microemulsions started in the 1970s, when enhanced oil recovery was a big topic [10]. In the meantime, the application fields of microemulsions are widely spread [11, 12]. In the pharmaceutical area drug delivery is an ubiquitous issue; in biotechnology microemulsions are used for enzymatic reactions and immobilization of proteins. Reaction media [13, 14], [15] for polymerization or producing nanoparticles and the implementation in cosmetics, foods and agrochemicals are further examples.

Especially in the decontamination field the interest in microemulsions as carrier media has increased in the last decades. One of the remarkable features the nano-scale structure of microemulsions plays a big role for effective decontamination applications.

In World War I warfare agents were increasingly used from both sides with the consequence of many victims [16]. The production and development of chemical weapons was raised during the World War II and the Cold War. Even after the Cold War a terroristic attack in the subway of Tokyo [17] in 1995 was a danger for the community. Therefore the development of an all-purpose decontamination system which can neutralize as much warfare agents as possible is unavoidable.

In the 1980s, already the German armed forces used macroemulsions for decontamination based on Marlowet IHF, tetrachlorethylene and calciumhypochloride, but they are not stable, harmful and a danger to the environment [18]. Therefore microemulsions as carrier media for degradating agents are a distinguished alternative for decontamination applications. They offer an oil and a water phase - a lipophilic and hydrophilic part in one system. Moreover, sugar surfactant microemulsions can be composed with biocompatible components which is another big advantage for decontamination purposes [19]. Furthermore, the temperature stability is an important fact for the use in different climatic regions.

Studying the structure of these systems requires big efforts in theoretical considerations and in experimental activities, many publications on this research area are a consequence. Due to the nanometer scale and therefore the need of expensive methods like neutron scattering methods the research is sometimes complicated.

The present thesis deals with the introduction of another technique for observing microemulsion structure and dynamics, FCS. On the one hand, the diffusion of the microemulsion structure can be measured, namely the collective breathing motion [20], on the other hand the dynamics of particles inside this structure can be investigated. The knowledge of these processes is important: The protein diisopropyl-fluorophosphatase (DFPase) is a famous candidate for decontamination applications, the assignment in a microemulsion system is a promising combination [21]. Moreover, another aim of this paper is the implementation of new microemulsion systems mainly based on pure surfactants that play a role as model systems for technical grade systems and show a higher purity, which is crucial for fluorescence methods.

But FCS is not the only method to look inside nano-scale structures. Also small angle scattering (SAS) techniques like small angle X-ray scattering (SAXS) and small angle neutron scattering (SANS) are used to characterize the structure. neutron spin echo (NSE) and pulsed-field-gradient nuclear magnetic resonance (PFG-NMR) provide information on the dynamical behavior of microemulsion systems.

4 Theoretical background

The main concepts for microemulsions and their abilities will be treated in this chapter. Firstly, the important role of surfactants and of the interfacial film will be discussed, further several different methods are used to observe structure and dynamics of microemulsion systems. To understand these applications, the background of these techniques will be explained in the following chapters.

4.1 Microemulsion

Microemulsions show interesting structures, although they look transparent for the human eye, which is caused by the small structure sizes about 50 times lower than the visible light wavelength.. But on a closer examination, they feature for example a sponge-like structure in the nanometer-scale for a suitable mass ratio of components. Moreover, the phase behaviour is very rich and shows more different structures [22], which have to be discussed in more detail (see chapter 4.1.3).

4.1.1 Surfactants

Amphiphilic molecules with a hydrophobic and a hydrophilic part are called surfactants or detergents and are the base of microemulsions. Normally, the hydrocarbon residue is the hydrophobic part and the hydrophilic part determines the kind of the surfactant. **Anionic surfactants**, where the hydrophilic part is anionic (for example sulfate, sulfonate and phosphate), are commonly used in washing, and cleaning agents [23], **cationic surfactants** have a cationic hydrophilic group and are applied in cosmetics, fabric conditioners, and sanitizers [24]. In a **zwitterionic surfactants** molecule a positive and negative charge is present, because of the skin friendliness this detergents are used in shampoos, body care products, bath additives and household detergents [25, 26]. Furthermore, **nonionic surfactants** have hydrophilic polar groups without any charge (hydroxyl-, carboxyl-, ester-, amide- and polyalkyl-groups). Also alcylpolyglycosides (APG©), known as sugar surfactants are part of the non-ionic detergents and are composed of renewable resources (sugar and fatty alcohol can be used as raw materials), these surfactants are the foundation of the microemulsions used in this work. The APG© components are Glucose and an alkyl-residue with chain lengths of six up to 14 carbon atoms. Longer carbon chains

implicate a high hydrophobicity and the formulation of a microemulsion is difficult, because the surfactant is not soluble in water.

4.1.2 Micelles

Because surfactants are molecules with an amphiphilic ability, they are able to form micelle in solution, if a critical micell concentration (CMC) is reached. Micelles are a cluster of molecules caused by reversible aggregation. The geometrical form of such particles must not be sphere-like, a micelle can also exist as cylindrical, plate- or rod-like objects.
The CMC is the concentration of surfactant, when the surface or the interface is completely covered with surfactant molecules, below the CMC the surface tension of the fluid is decreased, above the CMC more micelles emerge and the surfactant has no influence on the surface tension anymore. Micelles can also change macroscopic parameters like flow properties [23].

4.1.3 Structure and dynamics

Microemulsions based on sugar surfactants are composed of water, oil, sugar surfactant (C_iG_j) and co-surfactant (alcohol). Such systems thermodynamically stable. Different phases occur for certain mass ratios of these components. To quantify the amount of constituents, the following definitions will be used:

$$\text{fraction of oil: } \Phi = \frac{m_{\text{oil}}}{m_{\text{w}} + m_{\text{oil}}} \tag{1}$$

$$\text{fraction of surfactant: } \gamma = \frac{m_{\text{surf}}}{m_{\text{w}} + m_{\text{oil}} + m_{\text{surf}}} \tag{2}$$

$$\text{fraction of co-surfactant: } \delta = \frac{m_{\text{cosurf}}}{m_{\text{w}} + m_{\text{oil}} + m_{\text{surf}} + m_{\text{cosurf}}} \tag{3}$$

Due to the number of four components, the phase behavior can be described by a phase tetrahedron (compare fig. 1). When instead of a sugar surfactant a C_iG_j-surfactant is used, the tetraehedron changes to a phase prism, where the height corresponds to the temperature axis. For C_iE_j-systems, no co-surfactant is necessary to achieve a 1-phase structure. The temperature plays the role as a tuning parameter and acts like the co-surfactant in a C_iG_j system.
For a cut in the phase tetrahedron at a certain oil/water ratio Φ (fig. 1) the phase behavior is illustrated by a two-dimensional graph with the axis γ and δ (fig. 2).

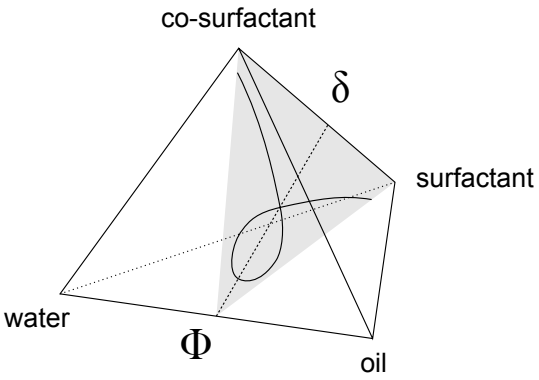

Figure 1: Phase tetrahedron of a sugar-surfactant based microemulsion with a cut for a water/oil ratio Φ *and the resulting Kahlweit-fish in reference to [22].*

The resulting image looks like a fish, known as "Kahlweit-fish". The one phase structures are located in the fish-tail: bicontinuous, oil- and water continuous, and lamellar phase [27]. The phases are also called Winsor-systems [1]: Type I with a water phase where the surfactant and oil is solubilised and an oil phase (located below the fish-body). Type II is an oil phase with solubilised surfactant and water and a water excess phase (region in the phase diagram above the fish body).

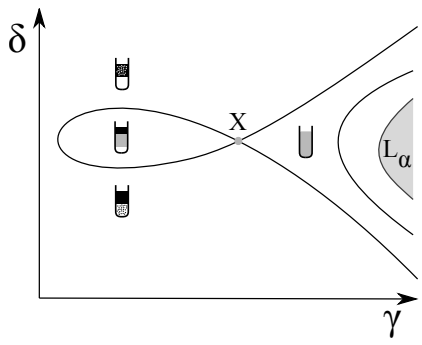

Figure 2: Kahlweit-fish of a sugar surfactant system with the so called X-point, fish-head (3-phase region), fish tail (1-phase) and water excess phase below, oil excess phase above the fish, in reference to [22].

Type III consists of 3 phases, a water phase, a microemulsion phase and a oil phase (in the fish-head). In the case of type IV only one phase is present, were all components are solubilised.

The lamellar region is a single phase area indicated by L_α in fig. 2. The L_α-phase and the

bicontinuous region are separated by a two phase coexistence zone [22].

- **bicontinuous phase (L_3 phase):** Behind the X-point, sponge-like structure with oil and water domains, seperated by the surfactant/co-surfactant interface.
- **lamellar phase (L_α phase):** Oil and water layers interrupted by the interfacial film. The L_α is a smectic type C liquid crystal.
- **oil in water microemulsion:** Oil droplets in water with a radius of some nm, below the lamellar region.
- **water in oil microemulsion:** Water droplets in oil, above the lamellar region.

What kind of structure emerges, depends on the composition of the components (Φ, γ) and on the shape of the amphiphilic film, which is mainly determined by the alcohol content δ.

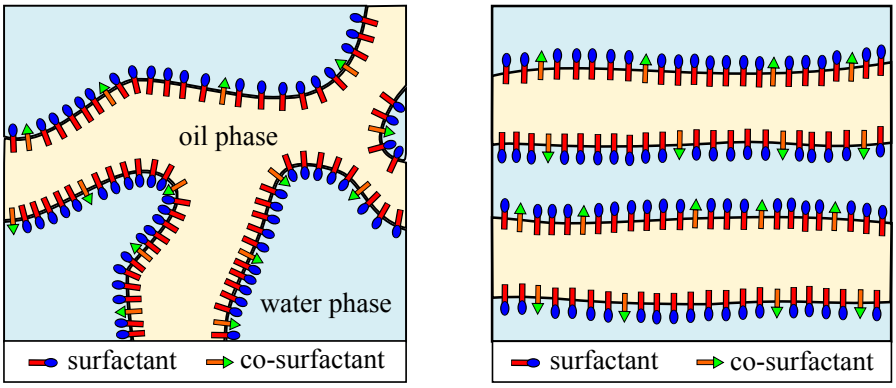

(a) (b)

Figure 3: Sketch of a (a) bicontinuous microemulsion and (b) lamellar phase

A common method to investigate the structure is measuring the conductivity of a sample [28]. In water continuous structures (oil in water) and in the bicontinuous phase the conductivity is relatively high: The water phase is continuous over the whole sample. On the other hand for water in oil phases, the conductivity is low. For lamellar structures the conductivity is lower than in the bicontinuous phase , if the conductivity is measured perpendicular to the interfacial film. However, if the conductivity can be measured in plane of the lamellae it will be higher compared to the bicontinuous phase [29]. The surfactant film and the oil phase hinders the conduction perpendicular to the lamellae.

4.1.4 The bicontinuous phase

This phase occurs close to the X-point in the fish tail of a Kahlweit-fish phase diagram (figure 2). The structure can be imagined as a sponge-like pattern and can be visualized by freeze fracture electron microscopy (FFEM) ([30]). The bicontinuous phase offers a huge internal interface, which is beneficial for decontamination applications. The oil and water component exist as interlaced continuous phases, separated by a surfactant/co-surfactant film. The bicontinuous structure appears preferably at equal oil/water fraction, meaning $\Phi = 0.5$ [31]. Bicontinuous phases can be detected by electrical conductivity measurements [32] and length scales can be obtained by SANS and SAXS experiments (chapter 4.1.6). The dynamic of such structures is often called "collective breathing motion" [33, 34] and can be measured by NSE, dynamic light scattering (Dynamic Light Scattering (DLS)) and PFG-NMR methods.

4.1.5 Curvature of the interfacial film

The interfacial film in the microemulsion systems studied here consists of a C_iG_j surfactant (hydrophilic) and a co-surfactant (alcohol, hydrophobic surfactant). The curvature H of the film depends on the amount of co-surfactant at the interface. Because of the smaller co-surfactant head group compared to the sugar surfactant, H changes from positive to negative values when co-surfactant is added.

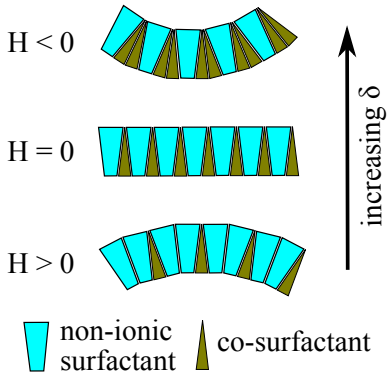

Figure 4: Non-ionic surfactant film in a sugar surfactant microemulsion: The curvature H depends on the amount of co-surfactant δ (hydrophobic), in reference to [22].

H can be calculated with the local curvatures $c_1 = \frac{1}{R_1}$ and $c_2 = \frac{1}{R_2}$, located at a point of the

surfactant film (with R_1 and R_2: radius of the curvatures):

$$H = \frac{1}{2}(c_1 + c_2) \tag{4}$$

For $H > 0$, oil in water droplets are formed. When H reaches negative values, the structure changes to water-in-oil droplets. If $H = 0$, there is no curvature of the film, the Gaussian curvature K has to be considered:

$$K = c_1 \cdot c_2 \tag{5}$$

When K is negative, the bicontinuous structure appears, for positive values the surface is planar and the structure is lamellar. This curvature can be affected with the type and amount of the surfactant and co-surfactant, temperature and addition of polymers. In such a bicontinuous structure, the length scales can be described according to Strey [35] by the characteristical length ξ:

$$\xi = \sqrt{\frac{2}{c_1^2 + c_2^2}} \tag{6}$$

In experiments it was observed that ξ is approximately half the periodicity d [36], which is a value for the domain size of the oil and water domain.

4.1.6 Length scales in microemulsions

Because of the structural dimensions in the nano-meter scale, a microemulsion looks transparent to the human eye. Hence, the structure cannot be observed by optical techniques. Light scattering methods would reveal the bulk-dynamics of the structure, therefore technologies with smaller wavelengths have to be used: X-ray or neutron scattering. SAXS and SANS experiments yield the dimensions of microemulsion systems (compare scattering theories in chapter 4.5). Another possibility is FFEM, for such measurements the sample has to be frozen very fast. But in a freezing process, the structure of the system might be changing and the appearing structures might not reflect the real state at normal temperatures.

Dimensions in a bicontinuous structure are characterized in terms of correlation lengths ξ and domain sizes d (equations 44, 45). These dimensions depend on the chain-length of the used surfactant and on the mass ratios Φ and γ. For sugar surfactant systems, the correlation length is between several nanometers up to nearly 100 nm. For $\Phi_{\text{volume}} = 0.5$ the oil and water domains show a similar size - at smaller Φ, the water domain size increases and decreases for $\Phi > 0.5$.

4.2 Decontamination applications

Chemical warfare agents are a big danger in times when terrorist attacks are a daily issue in several regions on earth. Therefore it gets more and more important that effective decontamination media are available. A couple of features are required for a adequate decontamination system: Ability to penetrate different kinds of surfaces, nontoxic, storable, noncorrosive and cheap to fabricate. Microemulsions can be composed of various different components and offer in the suitable composition all of these preconditions.
Most toxic chemicals and warfare agents have hydrophobic abilities. But in contrast the majority of degradation agents are hydrophilic. In a microemulsion, both features are present with a structure on the nanometer scale.
Furthermore, a decontamination medium should be able to wet surfaces. The human skin or coatings of military equipment are hydrophobic, therefore a fluid in form of a microemulsion can penetrate such surfaces to bring the decontamination agent close to the warfare substance. Nevertheless, also for hydrophilic surfaces, the media should be capable of wetting these surfaces.
Environmental compatibility is another important feature of decontamination media. On the one hand, when media are spread on military vehicles, they come also in contact with the environment. On the other hand, when media are applied on soldiers, it must not be toxic or harmful. A first approach is the composition of biodiesel based microemulsions [37] and systems are currently developed with components approved for cosmetic applications.
For a low-cost production it is important, that the necessary amount of surfactant is as small as possible. Therefore the X-point has to be shifted to small γ. Efficiency boosting by block co-polymers plays a major role for existing microemulsion systems, with only small amounts of block copolymers a much bigger amount of surfactant can be replaced [38–40].
Enzymes with decontaminating abilities solubilised in the water phase of a microemulsion are promising candidates for decontamination purposes. Especially the enzyme DFPase (see figure 5) of the squid Loligo vulgaris is able to detoxify nerve agents [18, 21, 22].

A recently presented decontamination process works as follows: In a first step the warfare agents are solubilised by the oil phase of the microemulsion, where they can get to the interface to come near the degradation agents which are solved in the water phase and the decontamination can

take place [41].

Figure 5: X-ray structure of DFPase of the squid Loligo vulgaris [42], with a molecular weight of 35 kDa. *[43]*

Another important ability of microemulsions is the structural stability over a huge temperature range (-20°C to 50°C) [44, 45], which is a crucial feature for applications in the military field. The length scales of the water and oil domains stay nearly constant determined by SANS and the bending elastic constant is temperature independent measured in NSE experiments.

4.3 Proteins in microemulsions

In the last subsection the use of proteins for decontamination applications was discussed already. Knowing the dynamics of such particles inside a bicontinuous phase of a microemulsion is important for designing efficient decontamination media. One question is, if the enzyme is moving inside e.g. the water domain or if it sticks to the surfactant interface. The dynamics of DFPase with a hydrodynamic radius of 2.34 nm [34] are hard to observe with inhouse-methods like photon correlation spectroscopy. Moreover, the microemulsion structure scatters light as well and overlays the signal of the protein. Therefore, we use proteins comparable in size, which are fluorescent and can be directly observed in a more simple way with fluorescence correlation spectroscopy. Green Fluorescent Protein (GFP) is a famous protein used for many applications in science by taking advantage of the fluorescent behavior without the need of labeling (chapter 5.2.3). Besides the questions relate to the use of microemulsions as reaction medium for enzymes, it is also possible to use the microemulsion as model system for the study of sub-diffusive behavior. The domain sizes in a bicontinuous microemulsion or the volume fraction in a droplet system can be easily controlled. Hence, such a system can be used to generate crowding in a well defined way.

4.4 Fluorescence correlation spectroscopy

This method exploits the fluorescence ability of molecules and is used to measure particle dynamics down to the nanometer scale [46]. The advantages are that one can decide, what dynamic is measured by specific labeling and that time ranges from microseconds up to 100 ms can be covered. But not only diffusion times, also concentration can be measured by FCS. In this section first the effect of fluorescence is discussed and afterwards the theoretical backgrounds will be covered.

4.4.1 Fluorescence

When a molecule is excitated into a higher energy state, the energy can be released again in different ways. The fastest process is the vibration relaxation with a half-life period of 10^{-12} s, then the molecule can fall back to the ground state by emitting light, which is called fluorescence [47], or it can perform inter-system crossing into a triplet state (figure 6), called phospho-

rescence [48]. Fluorescence has a lifetime of around 10^{-8} s and the wavelength of the emitted radiation is higher than the excitation wavelength because of the energy dissipation for vibration relaxation, which is a much faster process. Due to the high number of vibration and rotation states of fluorescent molecules, the emitted light has a broad wavelength distribution. Phosphorescence lifetimes are higher compared to fluorescence, starting at microseconds up to minutes or days, due to the small probability of the inter-system crossing.

The efficiency of fluorescent dyes is described by the quantum yield:

$$\Phi_Q = \frac{N(\text{photons emitted})}{N(\text{photons absorbed})} \tag{7}$$

For an ideal dye, $\Phi_Q = 1$, for example, Rhodamine B has a Φ_Q of 1, fluorescein 0.79 [49] and GFP 0.79 [50]. A high quantum yield is beneficial for a measurement, because the higher Φ_Q, the less laser power is needed for excitation. The used dye concentration has to be very low, because high concentrations might perturb the sample and more important might lead to cross-correlations. Ideally FCS is performed as a single molecule technique.

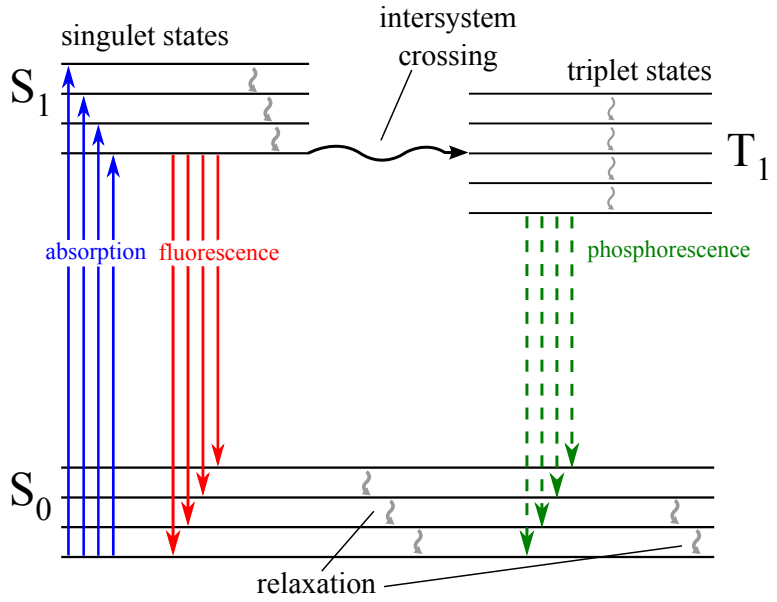

Figure 6: Jablonski diagram for a molecule which absorbs light and is excitated from the ground state S_0 into a higher energy state S_0 and partially undergoes inter-system crossing to the triplet state T_1.

4.4.2 FCS setup

FCS is a very sensitive technique to measure dynamics of fluorescent particles. A confocal setup is used in two different ways: First, to focus a laser beam and second, to detect the light emitted by a particle. Only light with a higher wavelength than the laser-light can pass a beamsplitter before the detector, which consists of two avalanche photo diodes for different wavelength ranges.

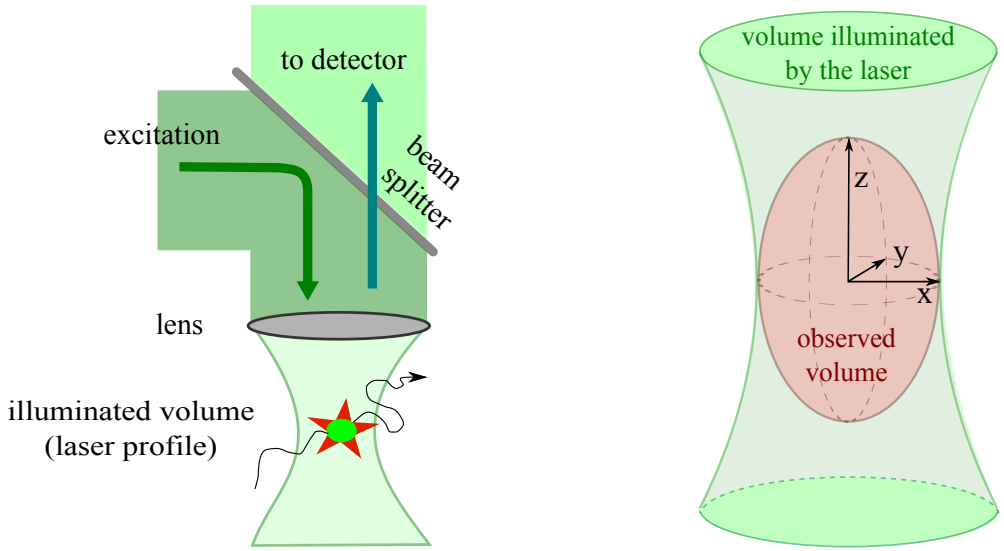

Figure 7: (a) Beampath in a FCS experiment: The laser is focused in the sample and excites fluorescent particles in the illuminated volume. These emit light collected by the confocal setup (b) Illustration of the observation volume and illuminated volume in the sample for an FCS experiment.

This technique requires fluorescent particles, in most cases the observed sample or the molecule has to be labeled with a fluorescent dye. In the case of microemulsions, there are several possibilities for labeling. An amphiphilic dye reflects the dynamics of the surfactant interface, a hydrophilic particle (fluorescent or labeled) can be used to observe the dynamics when diffusing in the water domain.

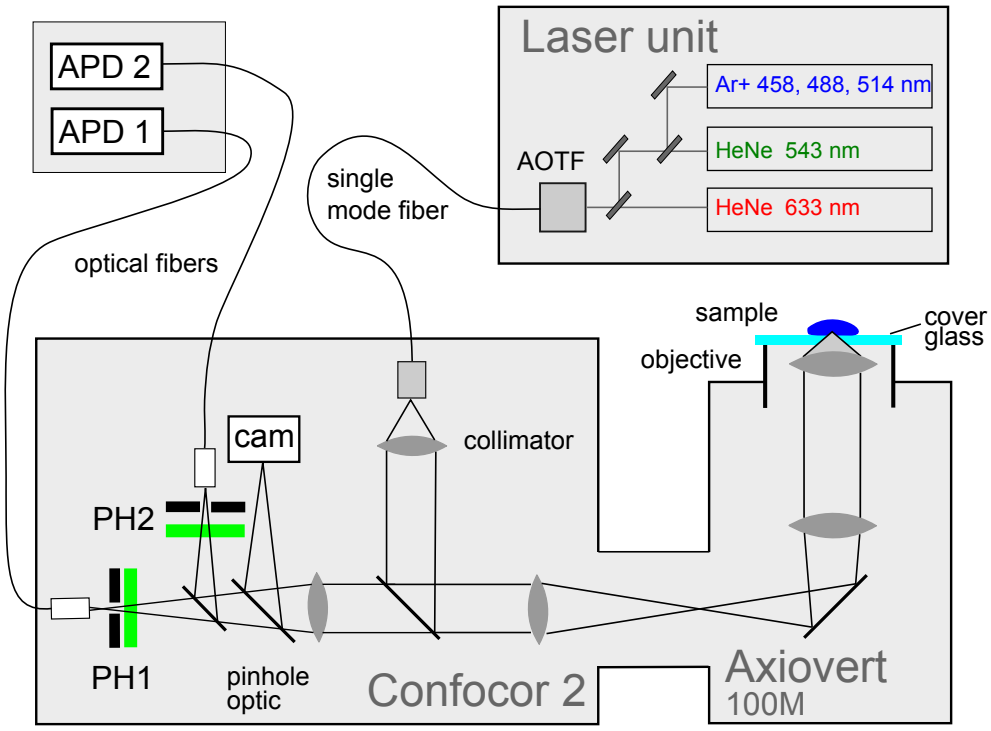

Figure 8: Beampath of the Zeiss Confocor 2 FCS system, which consists of several components. PH1 and PH2 are the pinholes for the particular beampaths, compare [51].

The commercially available device Zeiss Confocor 2 microscope is used for the measurements. It consists of modular components: Axiovert 100M (confocal microscope), the FCS part and a laser section with three different lasers for several wavelengths. The laser light is guided through a single mode fiber into the Confocor 2 unit and reflected by a dichroic mirror to the Axiovert 100M. The laser light is lead to the confocal microscope (fig. 7 a) and is focused into the sample (illuminated volume). The fluorescent particle emits light with a higher wavelength homogeneously in all directions. Some of the fluorescence light is collected by the microscope optics and is lead back into the Confocor 2 unit. Depending on the used beampath, it passes the emission filter and the pinhole 1 or 2 and reaches the detector. Only light with a higher wavelength than the laser will be detected, according to the chosen emission filter. Various excitation wavelengths are available: 458 nm, 488 nm, 514 nm, 543 nm and 633 nm. Appropriate emission filters (bandpass or longpass) can be selected.

4.4.3 Observation Volume

To obtain an autocorrelation function, the theoretical description of the measured intensity is important. The intensity depends on the geometry of the observed volume and on the diffusive movement of the fluorescent particles ($C(\vec{r},t)$) and the detection-efficiency function $W(\vec{r})$ [52]:

$$I(t) = \int_R W(\vec{r})C(\vec{r},t)d^3\vec{r} \tag{8}$$

The volume illuminated by the laser (fig 7 b) has a Gaussian shape in the $x-y$-plane and a Lorentzian shape in the z-direction.

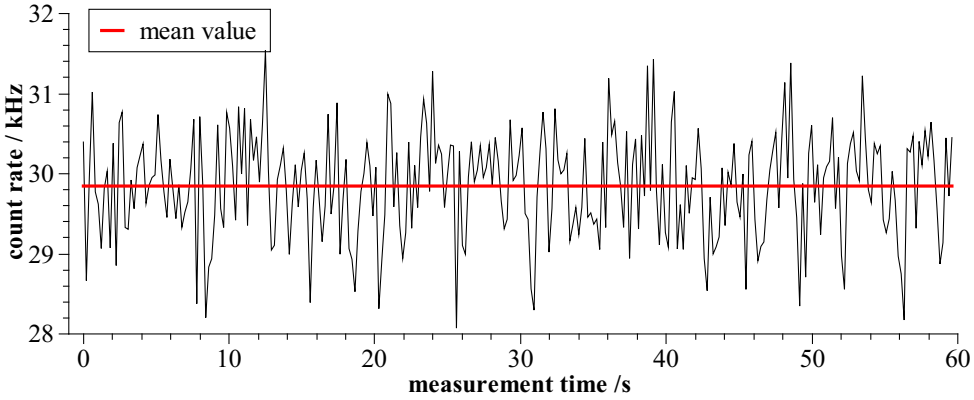

Figure 9: Time dependent intensity of a FCS measurement which reflects the diffusion of the fluorescent particles.

Considering the collection efficiency of the used lens (C-Apochromat 40x/1,2 W), the following function can be obtained, which describes the detection-efficiency of the used Confocor 2 setup:

$$W(r) = W_0 \cdot e^{-2\frac{x^2+y^2}{r_0^2}} \cdot e^{-2\frac{x^2}{z_0^2}} \tag{9}$$

This volume has the shape of a Gaussian ellipsoid with radius r_0 and the length z_0 in the z-direction.

$C(\vec{r},t)$ is given by the sum of infinitesimal small fluorescent points k located at $\vec{r_k(t)}$. Therefore a δ-function can be used for its description:

$$C(\vec{r},t) = \sum_k b_k \delta(\vec{r} - \vec{r_k(t)}) \tag{10}$$

The brightness of the fluorophore is given by b_k and depends on the quantum efficiency and the excitation profile.

The intensity (equation 8) can now be calculated, important is the autocorrelation $g_2(t)$:

$$g_2(t) = \frac{\left\langle I(t')I(t'+t)\right\rangle_{t'}}{\left\langle I(t')^2\right\rangle_{t'}} \tag{11}$$

With $W(r)$, $C(\vec{r},t)$ and the Fourier transformation of the deltafunction, $g_2(t)$ can now be calculated, the result is [52], [53]:

$$g_2(t) = 1 + \frac{1}{< C > V_{\text{eff}}} \frac{\int \Phi(\boldsymbol{q}) C(\boldsymbol{q},t) d^3\boldsymbol{q}}{\int \Phi(\boldsymbol{q}) d^3\boldsymbol{q}} \tag{12}$$

with the effective observation volume $V_{\text{eff}} = \pi^{3/2} r_0^2 z_0$, $< C >$ the mean particle density and $C(\boldsymbol{q},t)$ the reciprocal particle density. $\Phi(\boldsymbol{q})$ is a function which describes the observation volume in the reciprocal space and can be calculated for the Confocor 2 setup with $W(\boldsymbol{q})$, the Fourier transform of eq. 9:

$$\Phi(\boldsymbol{q}) = W(\boldsymbol{q})W(-\boldsymbol{q}) = \frac{W_0^2}{64} r_0^4 z_0^2 \cdot e^{-\frac{1}{4}r_0^2(q_x^2+q_y^2)} \cdot e^{-\frac{1}{4}z_0^2 q_z^2} \tag{13}$$

The term $C(\boldsymbol{q},t)$, which describes the fluctuating particle density, can be derived from the Fick's law of diffusion:

$$\frac{\partial C(\vec{r},t)}{\partial t} = D\nabla^2 C(\vec{r},t) \tag{14}$$

With the use of the Fourier transformation $C(\boldsymbol{q},t)$ the differential equation 14 can be solved:

$$C(\boldsymbol{q},t) = e^{-Dq^2 t} \tag{15}$$

4.4.4 Diffusion of the fluorophore

With equations 13 and 15, the autocorrelation $g_2(t)$ can be calculated:

$$g_2(t) = 1 + \frac{1}{N} \cdot \frac{1}{(1+\frac{t}{\tau}) \cdot \sqrt{1+(\frac{r_0}{z_0})^2 \cdot \frac{t}{\tau}}} \tag{16}$$

This is the FCS fit equation for one particle which shows a free 3D-diffusion. The structure factor $S = \frac{r_0}{z_0}$ reflects the geometry of the detection volume, N is the number of particles in the volume

and τ the diffusion time. For high N the value of the autocorrelation function decreases. Thus a small concentration of fluorophores is favorable for measurements with a high autocorrelation. Concentrations down to $10^{-9}\,\mathrm{mol/l}$ can be detected in a FCS experiment. The best concentration range for a sufficient fluorescence intensity and an adequate autocorrelation value is $10^{-7}\,\mathrm{mol/l}$ to $10^{-8}\,\mathrm{mol/l}$.

If the excitation laser power is to high, the dye could be bleached when passing the illuminated volume. This effect influences the autocorrelation function, because the molecule gets dark. For example, rhodamine 6G has a higher photostability compared to fluorescein [54].

4.4.5 Triplet decay

Most of the commonly used dyes for FCS experiments show the inter-system crossing effect (compare fig. 6), which results in a triplet decay in the range of some μs. The 10^{-8}s fluorescence lifetime cannot be detected by the FCS equipement, but the triplet decay is in the range of the FCS time-resolution. This effect appears as an additional decay at low autocorrelation timescales (compare figure 10. This decay can be described by the triplet autocorrelation part [55]:

$$G_{\mathrm{triplet}} = \frac{T}{1-T} e^{-\frac{t}{\tau_T}} \tag{17}$$

τ_t represents triplet time and T the triplet factor. Applied to the 3D diffusion equation 16:

$$g_2(t) = 1 + \frac{1}{N}\left[1 + \frac{T}{1-T} e^{-\frac{t}{\tau_T}}\right] \cdot \frac{1}{(1+\frac{t}{\tau}) \cdot \sqrt{1+(\frac{r_0}{z_0})^2 \cdot \frac{t}{\tau}}} \tag{18}$$

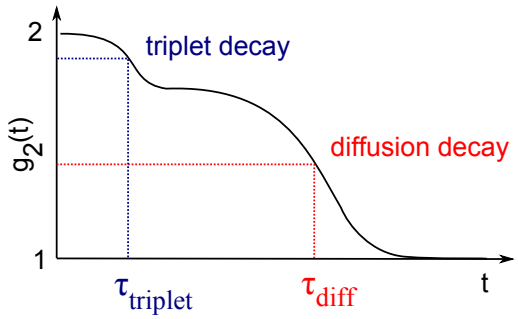

Figure 10: Illustration of the FCS autocorrelation curve with triplet decay of the fluorescent dye. τ_{triplet} is located at 1/e and τ_{diff} at 1/2 of $G(0)$.

The model can be adapted to more components with different size and diffusion times, which are detected simultaneously:

$$g_2(t) = 1 + \frac{1}{N}\left[1 + \frac{T}{1-T}e^{-\frac{t}{\tau_T}}\right] \cdot \sum_{i=1}^{N}\left[\frac{1}{(1+\frac{t}{\tau_i}) \cdot \sqrt{1+(\frac{r_0}{z_0})^2 \cdot \frac{t}{\tau_i}}}\right] \tag{19}$$

k_i is the ratio of particle i. The diffusion times τ_i have to differ sufficiently from each other, to be distinguished using a fit according to equation 19, normally by a factor of 2. The higher the number of diffusing components in the equation, the more parameters influence the fit. Therefore a maximum of three components is reasonable, when other boundary conditions like particle ratio are known.

4.4.6 Anomalous diffusion

In case of confinement or crowding effects, the diffusion can be anomalous. In this case, the mean square displacement σ_r is not linear in time anymore:

$$< s^2 >= \sigma_r = D \cdot t^{\alpha} \tag{20}$$

The anomalous diffusion exponent α has to be regarded in equation 16, that leads to [56]

$$g_2(t) = 1 + \frac{1}{N}\left[1 + \frac{T}{1-T}e^{-\frac{t}{\tau_T}}\right] \cdot \frac{1}{\left(1+(\frac{t}{\tau_d})^{\alpha}\right) \cdot \sqrt{1+(S^2 \cdot \frac{t}{\tau_d})^{\alpha}}} \tag{21}$$

If $\alpha < 1$, sub-diffusive behavior is observed. Smaller α means more confinement for the diffusing particle. In the bicontinuous phase of a microemulsion, the diffusion of a particle inside the water domains is hindered by the surfactant/co-surfactant interface.

4.4.7 Calibration of the instrument

τ_D is the time a particle needs to pass the observation volume

$$\tau_D = \frac{r_0^2}{4D} \tag{22}$$

With a dye, where D is known from the literature (often fluorescein for the 488 nm beampath, rhodamine 6G for 514 nm beampath and rhodamine B for 534 nm beampath), r_0 can be calculated and τ_D obtained by a fit of the autocorrelation curve. With r_0 and the fit parameters, also z_0 can be calculated. Then S can be hold constant for measurements with an unknown sample [51].

4.5 Scattering methods

Structures and dynamics of microemulsions can be investigated using different scattering methods. In principle, scattering is the interaction of a particle with an object. Photons with different energies (or wavelengths) are scattered at objects of various size: In light scattering experiments, differences of the refractive index (for example oil $\longleftrightarrow$ water) and the size of particles influence the scattered light. To resolve structures, the used wavelength has to be in the dimension of the structure size.

If the wavelength is smaller (e.g. X-rays) the photon energy is bigger and photon is scattered by the molecule electrons: Therefore, in X-ray scattering applications the distribution of the electrons is crucial. Another commonly used technique is neutron scattering, neutrons have no electric charge and are able to permeate matter and interact with the nucleus of atoms.

Light and X-ray scattering techniques can be accomplished at commercially available or self designed equipment. Neutron scattering experiments have to be performed at a research facility, normally the neutron source is a nuclear reactor and the neutron detection is a sophisticated and expensive technology. For X-ray scattering applications, a research facility with a synchroton source is the superior option, because the flux and the quality of the detector is better compared to inhouse-instruments.

4.5.1 Photon correlation spectroscopy

This technique, also called Dynamic Light Scattering (DLS), exploits the ability of small particles or structures to scatter visible light. In contrast to static light scattering methods, photon correlation spectroscopy (PCS) yields information about diffusion processes. DLS is particularly suitable to measure the dynamics of macro-molecules, provides information about the diffusion coefficient and also the polydispersity of particles.

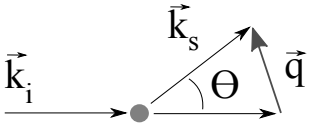

Figure 11: wave vector $\vec{q}$ in a light scattering experiment with incoming wave $\vec{k_s}$, scattered wave $\vec{k_s}$ and scattering angle Θ

Important for light scattering experiments is the wave vector $\vec{q}$ (compare figure 11):

$$q = |\vec{q}| = \frac{4\pi n_0}{\lambda} \sin\frac{\Theta}{2} \tag{23}$$

with: n_0: refractive index of the solvent, λ: wavelength of the scattered light, Θ: scattering angle

The normalized electric field autocorrelation function is given by:

$$g_1(t) = \frac{< E^*(\vec{q},t)E(\vec{q},t+t') >}{< E(\vec{q},0) >} \tag{24}$$

In experiments mostly only the scattered intensity is accessible by a instrument. Thus $g_1(t)$ can not be measured directly. The intensity I is detected time- and q- dependent to calculate the autocorrelation function $G_2(t)$, which measures the correlation at the time t' with itself at a later time $t + t'$:

$$G_2(\vec{q},t) =< I(\vec{q},t+t')I(\vec{q},t) >= \lim_{T\to\infty} \frac{1}{T} \int_0^T I(t+t')I(t')dt' \tag{25}$$

The autocorrelation function ca be normalized:

$$g_2(\vec{q},t) = \frac{G_2(\vec{q},t)}{< I(\vec{q},t') >^2} \tag{26}$$

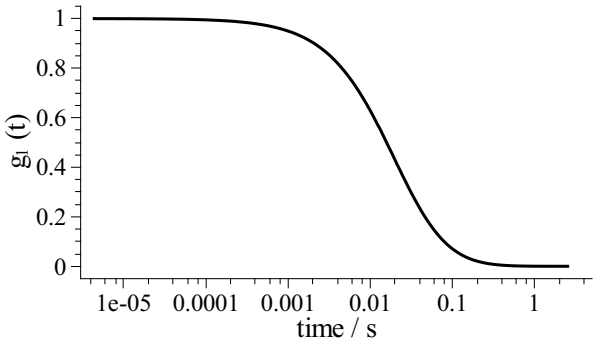

Figure 12: Autocorrelated measurement data from a photon correlation spectroscopy measurement. Time-axis is logarithmic.

The measured intensity provides no information about the electrical field $\vec{E}$, but the Siegert-relation connects the intensity autocorrelation and $g_1(t)$:

$$g_2(t) = 1 + \beta |g_1(t)|^2 \tag{27}$$

β depends on the used measurement instrument. In a monodisperse system (e.g. spherical particles), $g_1(t)$ can be calculated by using a monoexponential function:

$$g_1(t) = e^{-Dq^2 t} = e^{-\Gamma t} \tag{28}$$

The diffusion coefficient D gives information about the particle radius.
For polydisperse systems, a distribution function $G(\Gamma)$ is implemented, which gives information about polydispersity:

$$g_1(t) = \int_0^\infty G(\Gamma) e^{-\Gamma t} dt \tag{29}$$

$G(\Gamma)$ can be regarded as a sum of single contributions [57]:

$$G(\Gamma) = \sum_{i=0}^{N} a_i \delta(\Gamma - \Gamma_i) \tag{30}$$

applied to eq. 28:

$$g_1(t) = \sum_{i=1}^{N} a_i e^{-\Gamma_i t} \tag{31}$$

There are different possibilities to compute the dynamics of a polydisperse system. One is the method of cumulants [58]. Another suitable approach for this problem with more species is the

method of the inverse Laplace transformation. The CONTIN program [59], [60] exploits this procedure and can be used to analyze measured light scattering data. The output of CONTIN is a value of Γ_i, which depends on q. With

$$\Gamma = Dq^2 \tag{32}$$

a linear regression when Γ is plotted as a function of q^2 (q calculated by eq. 23) leads to D.

When spherical particles are observed (which is not the case in a bicontinuous structure), the hydrodynamic radius R_H can be estimated by the Stokes-Einstein equation:

$$D = \frac{k_B T}{6\pi\eta R_H} \tag{33}$$

Here, η is the viscosity. With equation 33 the hydrodynamic radius of e.g. proteins can be estimated (compare chapter 5.2.2).

4.5.2 Setup of the PCS experiment

The PCS measurements were performed on an ALV-5000 [61] instrument. In fig. 13 the setup for photon correlations spectroscopy is shown. The light from a Nd:YVO_4 laser (green, 532 nm) or a Helium-Neon laser (red, 633 nm) passes a neutral density filter (ND filter, to adjust the laser intensity), a lens and a Glan Thompson Prism and is scattered by the sample. The sample located in a temperature controlled bath filled with toluene scatters the laser light.

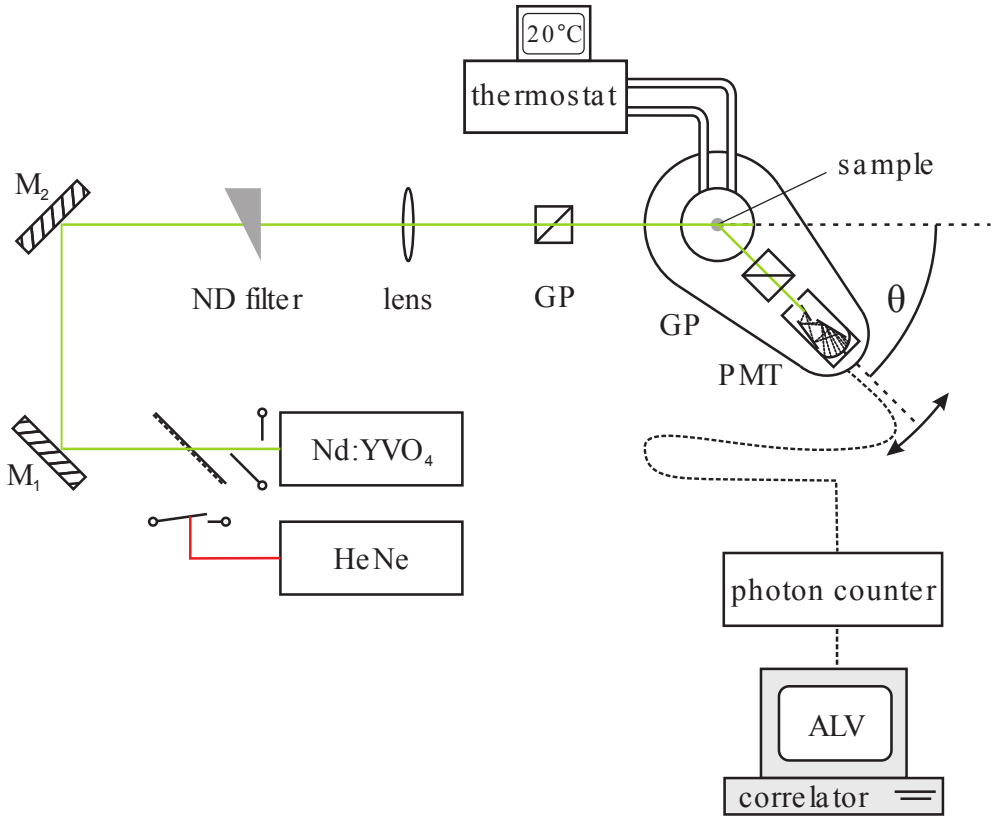

Figure 13: ALV-5000 Photon Correlation Spectroscopy setup, M_i: mirror, GP: Glan Thompson Prism, PMT: Photo Multiplier Tube

Toluene is used for matching the refractive index of the glass cuvette. The scattered light is detected by a photomultiplier mounted on a goniometer, where the scattering angle Θ and therefore q can be adjusted. With a photon counter and a correlator, the signal of the PMT is registered by the computer with the ALV software.

4.5.3 Small angle neutron and X-ray scattering

For SAS experiments, the scattering intensity and the scattering vector q are important parameters. The scattering intensity from a single particle depends on the scattered amplitude $F(q)$:

$$I(q) = |F(q)|^2 \tag{34}$$

$F(q)$ is the Fourier transform of the mass distribution (SANS) or electron distribution (SAXS) $\rho(r)$:

$$F(q) = \int_V \rho(r) e^{-iqr} dr \tag{35}$$

$$\Rightarrow I(q) = \left| \frac{1}{V} \int_V \rho(r) e^{-iqr} dr \right|^2 \tag{36}$$

In the case of N identical particles, the intensity is given by:

$$I(q) = \frac{N}{V} (\rho_p - \rho_0)^2 V_p^2 \left| \frac{1}{V_p} \int_V \rho(r) e^{-iqr} dr \right|^2 \tag{37}$$

with ρ_0: mass/electron density of the solvent, ρ_p: mass/electron density of the particle, V_P: particle volume, V: illuminated volume, $\rho_0 - \rho_0$: scattering contrast and the *form factor* $P(q) = \left| \frac{1}{V_p} \int_V \rho(r) e^{-iqr} dr \right|^2$

But also interactions between the particles have to be considered, the total scattering intensity is now calculated by [62] ($F_k(q)$: electrical field contribution of particle k):

$$I(q) = \frac{1}{V} \sum_{k=1}^{N} \left\langle \left| F_k(q) \right|^2 \right\rangle + \frac{1}{V} \left\langle \sum_{k=1}^{N} \sum_{\substack{j=1 \\ j \neq k}}^{N} F_k(q) F_j^*(q) e^{-iq(r_k - r_j)} \right\rangle \tag{38}$$

When the particles are monodisperse and spherical, the intensity can be simplified to:

$$I(q) = n \left\langle \left| F_k(q) \right|^2 \right\rangle \left\{ 1 + \left\langle \sum_{k=1}^{N} \sum_{\substack{j=1 \\ j \neq k}}^{N} e^{-iq(r_k - r_j)} \right\rangle \right\} \tag{39}$$

$$I(q) = nP(q)S(q) \tag{40}$$

The first term $P(q)$ (**form factor**) reflects the contribution of one particle, the second term, $S(q)$ (**structure factor**) is based on the contribution of the particle interaction: spatial arrangement

of the particles relative to an arbitrary origin. $S(q) = 1$ in a dilute solution, where the particles do not "feel" their neighbors.

4.5.4 Teubner Strey approximation

SANS and SAXS scattering measurements of a bicontinuous phase show a typical broad peak when $I(q)$ is plotted. M. Teubner and R. Strey developed a theory to describe this peak [36], based on an order expansion of the Landau free energy F, which is given by:

$$F = \int f(\psi, \nabla\psi, \Delta\psi) d^3r \tag{41}$$

free energy density f:

$$f = a_0 + a_1\psi + a_2\psi^2 + a_3\psi^3 + a_4\psi^4 + \cdots + c_1(\nabla\psi)^2 + c_2(\Delta\psi)^2 + \ldots \tag{42}$$

In the case of microemulsions, $a_2 > 0$, $c_1 < 0$ and $c_2 > 0$, all other parameters $= 0$. This yields the scattering intensity distribution:

$$I(q) = \frac{8\pi/\xi \left\langle (q-\bar{q})^2 \right\rangle c_2/V}{a_2 + c_1 q^2 + c_2 q^4} + bkg \tag{43}$$

with: $\left\langle (q-\bar{q})^2 \right\rangle$: mean square fluctuation of the scattering density ρ.

domain size (quasi periodic repeat distance of the oil and water domains):

$$\frac{d}{2\pi} = \left[\frac{1}{2} \left(\frac{a_2}{c_2} \right)^{1/2} - \frac{c_1}{4c_2} \right]^{-1/2} \tag{44}$$

and the correlation length ξ (dispersion of d):

$$\xi = \left[\frac{1}{2} \left(\frac{a_2}{c_2} \right)^{1/2} + \frac{c_1}{4c_2} \right]^{-1/2} \tag{45}$$

For fitting SANS and SAXS data, eq. 43 will be simplified, the constants in the numerator are summarized in k:

$$k = 8\pi/\xi < n^2 > /V \tag{46}$$

dividing eq. 43 by kc_2:

$$I(q) = \frac{1}{\frac{a_2}{kc_2} + \frac{c_1 q^2}{kc_2} + \frac{q^4}{k}} = \frac{1}{r_2 + t_1 q^2 + t_2 q^4} \tag{47}$$

When ξ is calculated similar to eq. 45, k is eliminated and the result is equal to eq. 45:

$$\xi = \left[\frac{1}{2}\left(\frac{r_2}{t_2}\right)^{1/2} + \frac{t_1}{4t_2}\right]^{-1/2} = \left[\frac{1}{2}\left(\frac{a_2 k}{kc_2}\right)^{1/2} + \frac{c_1 k}{4kc_2}\right]^{-1/2} = \left[\frac{1}{2}\left(\frac{a_2}{c_2}\right)^{1/2} + \frac{c_1}{4c_2}\right]^{-1/2} \tag{48}$$

Hence, there are only three parameters left (with an additional background parameter) for fitting SANS and SAXS curves with eq. 47.

4.5.5 Droplet structures

Droplet structures can be approximated by a fitting model of polydisperse hard spheres. According to equation 40 the scattering intensity of a sample can be calculated by regarding the structure factor and form factor.

In the case of spheres, the form factor can be calculated by (η: scattering length density difference between particle and matrix, R: Radius of the spheres):

$$P(q,R) = \frac{4}{3}\pi R^3 \eta \cdot 3\frac{sin(qR) - qRcos(qR)}{(qR)^3} \tag{49}$$

In microemulsion systems the droplets are polydisperse, therefore a Schultz-Zimm $SZ(R)$ distribution can be assumed (R_a: scaling parameter - maximum of the distribution for large k, $k = 1/\sigma^2$, σ. variance, $\Gamma(k)$: Gamma-function):

$$SZ(R) = \frac{N}{R_a}\frac{R}{R_a}^{k-1}\frac{k^k exp(-k * R/R_a)}{\Gamma(k)} \tag{50}$$

Regarding a monodisperse approximation for the hard sphere structure factor $S(q,R)$ (given by a hard sphere potential which depends on the volume fraction of the spheres and the sphere radius), the intensity can be calculated by:

$$I(q) = < P(q,R)^2 > S(q) \tag{51}$$

These calculations with the above mentioned assumptions can be done using the SASfit [63] or the GIFT [64,65] software.

4.5.6 Neutron-spin echo

With this technique the dynamics of particles or structures can be measured based on neutron scattering [66, 67]. The accessible time range is 0.001 to 250 ns at a wavelength of 6 to 25 Å .

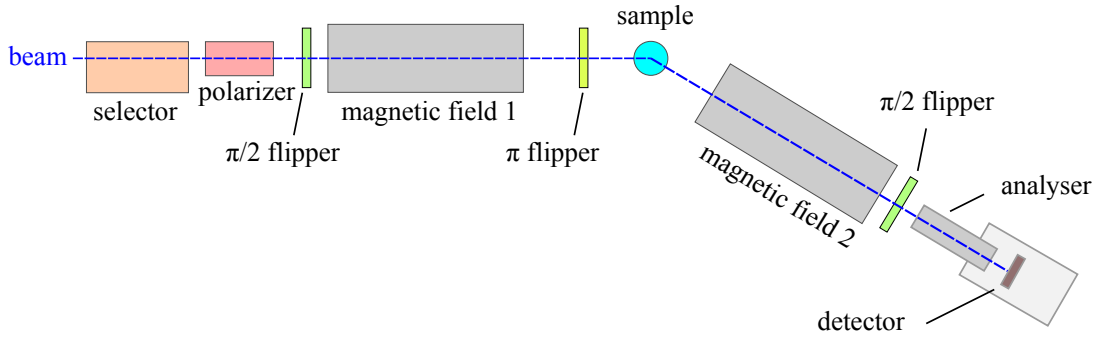

Figure 14: Simplified setup of a NSE experiment in reference to [68].

A polarized neutron beam is wavelength selected and enters a magnetic field B_1 (length L_1) which is orientated perpendicular to the neutron polarization. In the magnetic field 1 the neutrons undergo *Larmor precession*. After the magnetic field, the neutron spins have a specific phase depending on their velocity v. The Larmor frequency ω_L is defined by:

$$\omega_L = \gamma B \tag{52}$$

and the neutron spin $\varphi(v)$:

$$\varphi(v) = \omega_L t = \omega \frac{L_1 B_1}{v} \tag{53}$$

The polarization P_x in the x-direction is calculated by:

$$P_x = \langle cos\varphi \rangle \tag{54}$$

In the case of elastic scattering in the sample, the neutrons enter the second magnetic field B_2 (length L_2), which is oriented antiparallel to B_1. After B_2, the spin phase is:

$$\varphi = \gamma \frac{L_1 B_1}{v} - \frac{L_2 B_2}{v} \tag{55}$$

If $L_1 B_1 = L_2 B_2$, the spin phase is 0 and $P_x = 1$ (maximum value), which is called the spin echo point.

When the scattering of the sample is inelastic, the kinetic energy of the neutrons changes after

the sample, therefore the neutron velocity is different (γ: gyromagnetic ratio):

$$\varphi = \varphi_2 - \varphi_1 = \gamma \left(\frac{L_1 B_1}{v_1} - \frac{L_2 B_2}{v_2} \right) \tag{56}$$

With only small energy transfers dv and $L_1 B_1 = L_2 B_2$:

$$\varphi = \gamma LB \left(\frac{1}{v_1} - \frac{1}{v_2} \right) = \gamma LB \left(\frac{1}{v_1} - \frac{1}{v_1 + dv} \right) \approx \gamma LB \frac{dv}{v_1^2} \tag{57}$$

Energy difference:

$$\hbar\omega = \frac{1}{2} m v_2^2 - \frac{1}{2} m v_1^2 = \frac{m}{2} \left((v_1 + dv)^2 - v_1^2 \right) \approx m v_1 dv \tag{58}$$

Combining equations 57 and 58:

$$\varphi = \frac{\gamma \hbar B L}{m v_1^3} \cdot \omega = \tau \cdot \omega \tag{59}$$

τ is called the *spin echo time*. The polarization P_x is now calculated by:

$$P_{NSE} = \left\langle cos(\varphi) \right\rangle = \left\langle cos \left(\frac{\gamma BL}{m v^3} \hbar\omega \right) \right\rangle \tag{60}$$

With $t = \frac{\gamma \hbar B L}{m v^3}$ the measured signal $S(q, \omega)$ is the Fourier transform of $I(q, t)$:

$$P = \frac{\int S(q, \omega) cos(\omega t) d\omega}{\int S(q, \omega) d\omega} \tag{61}$$

$S(q, \omega)$ is the Fourier transform of $I(q, t)$ and P can be rewritten:

$$P(q, t) = \frac{I(q, t)}{I(q, 0)} \tag{62}$$

P is measured at different spin echo times τ, the result is a descending curve and can be fitted with an appropriate model depending on the observed particle or structure dynamics.

Spherical particles in dilute solution:

According to the methods of cumulants, $\ln \frac{I(q,t)}{I(q,0)}$ can be expanded ([58], [69] and [34]) with $K_1 \dots K_n$ as cumulants:

$$\ln \frac{S(q,t)}{S(q,0)} = -K_1 t + \frac{1}{2} K_2 t^2 - \frac{1}{3!} K_3 t^3 + \frac{1}{4!} K_4 t^4 + \dots \tag{63}$$

When only the first cumulant is considered, the effective diffusion coefficient is calculated by (used in different works for NSE analysis: [70], [71], [72])

$$D_{\text{eff}} = \frac{K_1}{q^2} \tag{64}$$

With equation 33, the hydrodynamic radius can be calculated.

Microemulsion dynamics

Microemulsions show different kinds of motions: The collective motion of the whole bicontinuous structure and the thermal induced undulations of the amphiphilic film [33, 34, 73]. If these motions are combined in an empirical approach, the intermediate scattering function can be described by:

$$\frac{I(q,t)}{I(q,0)} = \exp(-\Gamma_{col}\tau)\left(A + (1-A)\exp(-\Gamma_u \tau)^{\beta}\right) \tag{65}$$

Γ_{col} can be obtained from DLS experiments, Γ_u describes the decay rate of the relaxation of the thermally excited undulations, $\beta = \frac{2}{3}$ is a stretching exponent [34]. The resulting relaxation rate Γ_u is predicted to show a linear dispersion in q^3 and from the slope the bending elastic constant κ can be obtained [58].

5 Experimental section

Before showing results, the microemulsion systems and the used fluorescent probes will be characterized. Fluorescence spectra of the particles show at which wavelengths an optimum excitation is possible. Also the phase diagrams for all used systems are essential.

5.1 Used chemicals

Water was purified by a Millipore^{TM} system. Cyclohexane (chromatographic purity, > 99.7 %) and the amphiphilic dye Rhodamine B octadecyl ester perchlorate (purity > 98 %) were purchased from Sigma-Aldrich/Schnelldorf, and 1-Pentanol (> 99 %) from Merck/Darmstadt. *N*-dodecyl-β-D-maltosid was purchased from Glycon/Luckenwalde, *n*-nonyl-β-D-maltosid and *n*-octyl-d17-β-D-glucopyranoside-d7 from Affymetrix / High Wycombe. The technical grade surfactant Glucopon220 was obtained from Henkel/Düsseldorf and Simulsol SL55 from Seppic (Paris, France). GFP+ and fluorescent protein derived from Discosoma sp (mCherry) were produced at the Bielefeld University, Physical and biophysical Chemistry. The GFP+ stock solution had a concentration of 10 $^{mg}/_{ml}$ in a 50 mM NaH_2PO_4, 300 mM NaCl, 500 mM Imidazol buffer. The mCherry 10 $^{mg}/_{ml}$ stock solution was buffered in a 50 mM K_2HPO_4/KH_2PO_4 (pH 8.0), 300 mM NaCl solution. FITC- and TexasRed-labeled BSA were obtained from Sigma-Aldrich (Schnelldorf, Germany). The enzyme DFPase for the NSE measurements was provided by M.-M. Blum (Blum Scientific, Hamburg) in a buffered (10 mM TRIS, 2 mM $CaCl_2$, pH 7.5) solution with a concentration of approximately 7 $^{mg}/_{ml}$.

5.2 Systems

Commercially available sugar surfactants with a chain length distribution were used as basis in the first approach for composing microemulsion systems. They show a broad bicontinuous regime when the amount of co-surfactant is changed. Unfortunately these systems show a high background fluorescence activity which would be a key problem for FCS experiments. Therefore detergents with a high chemical purity and a fixed chainlength have been used. Moreover, microemulsion systems with a high purity can act as a defined model system for different methods of measurements.

Nevertheless, these model systems show fluorescence activity, too. However the background

intensity is much lower compared to the technical grade surfactant (discussed in 6.1.1). Surfactants with different chain lengths have been used, which revealed an influence on the phase behavior and correlation/domain lengths of the microemulsion. For performing measurements in the bicontinuous regime, a broad lamellar phase is obstructive.
In recent observations, the technical grade surfactants SL55 ($C_{12...14}G_{1.3}$) and Glucopon 220 ($C_{8...10}G_{1.3}$) played the major role [34], [44]. The comparable pure-surfactant derivatives are $C_{12}G_2$ and $C_{10}G_2$.
In recent experiments [74] the alcohol 1-pentanol was found to be the first choice as co-surfactant in sugar surfactant based microemulsion systems. The 1-phase area started at the smallest δ values and was broad compared to other co-surfactants with longer chain lengths or other alcohols.

5.2.1 Recording of phase diagrams

To discover the phase behavior of a microemulsion system, usually the $\delta(\gamma)$ diagram is explored by preparing samples with different γ-values and rising the amount of co-surfactant δ from 0 until the upper end of the 1- or 3-phase region is reached and the system forms an oil-excess phase. This procedure could be very time consuming, because the phase separation in the 2-phase region or in the lamellar part might take several hours, which depends on the used components, especially the surfactant. In addition to that, the γ-steps define the number of samples. In case of technical grade surfactants, they are already available as a stock solution from the manufacturer, where the surfactant is solved. Particularly the solubilisation of long chain surfactants like $C_{12}G_2$ at high γ-values takes a long time, too. Especially in this system the phase separation is very slow (up to some weeks).
The procedure for logging a phase diagram works as follows: First, the samples are prepared by weight, using a micro scale for the solid chemicals like the surfactant and an automatic pipette for the fluid components (water and oil). After a phase separation occurred, the amount of co-surfactant is rised by defined δ steps, usually $\Delta\delta = 0.05$ or 0.1 and mixed with a vortexer. This is repeated, until the 2-phase region above the fish is reached. Nevertheless, the samples have to be checked for the existence of lamellar phases by watching it through crossed polarizers.
This process is done for $\Delta\gamma = 0.02$ steps, the phase borders are extrapolated and the X-point can be estimated. When Φ is also a parameter which should be varied, the number of samples increases further.

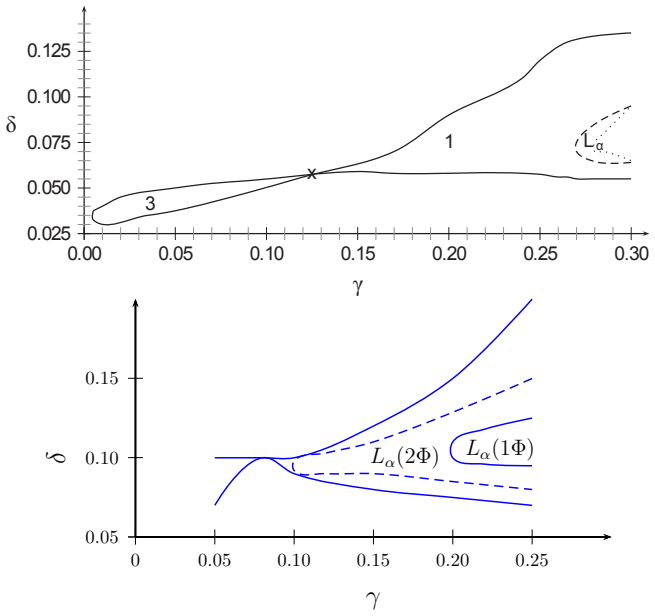

(a) (b)

Figure 15: Comparison of phase diagrams for (a) a technical grade surfactant ([74], Glucopon 220, $C_{8...10}G_{1.3}$) and (b) a pure surfactant ($C_{10}G_2$). Both systems consist of cyclohexane as oil component and 1-pentanol as co-surfactant.

Phase diagrams of pure surfactants compared to related technical grade surfactants, which are a mixture of molecules with different chain lengths, often show another structure behaviour in the fish tail. In figure 15 the Glucopon 220 diagram and the $C_{10}G_2$ diagram are depicted. In the pure surfactant phase diagram a much bigger lamellar phase appears, the L_α (2Φ) region reaches nearly to the X-point, only a small bicontinuous region exists very close to the X-point. This makes the sample preparation sometimes difficult in pure systems compared to technical grade systems.

5.2.2 Proteins in microemulsions

Measuring the dynamics of proteins like DFPase in the water domain (compare figure 16) could be difficult. Knowing these dynamics is important for decontamination applications. The size of the protein is to small for photon correlation spectroscopy for a suitable scattering intensity, especially inside a microemulsion, which shows a higher scattering intensity by itself. The scattering of the protein would be superimposed by the microemulsion. Another method for ob-

taining the protein dynamics is neutron spin echo. But the difficulty here is the need of contrast variation. To measure only the dynamics of the protein, the water- and oil-phase, surfactant and co-surfactant have to be deuterated. Deuterated surfactants are very expensive and not available for every type of sugar surfactant.

Hence, the method of choice is FCS. The components of the microemulsion don't need to be deuterated and compared to other methods, quick measurements are possible. But the main problem withFCS is the need of a fluorescent particle. Normally, a fluorescent label is bound to the tracer particle, which should be observed. However, the ideal way of realizing the FCSexperiment is the usage of a particle, which shows fluorescence itself. This minimizes the problem of an incomplete labeling, where unbound dye-molecules are left and represent an additional dynamical component. This complicates the fitting process of the autocorrelation function.

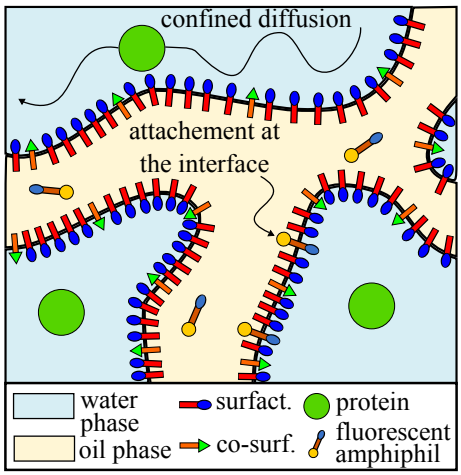

Figure 16: Model for particles in the water domain of a bicontinuous microemulsion. Fluorescent surfactants attach at the interface, hydrophilic proteins are dissolved in the water phase.

An appropriate choice for this work is the GFP (compare figure 17), particularly GFP+. This protein was found in the jellyfish *Aequorea victoria*, which was first extracted at 1962 [77]. GFP+ shows a 320 times higher fluorescence intensity than the wild type protein [78].

Compared to DFPase with a molecular weight of 35 kDa, GFP+ has approximately 27 kDa, therefore the size is similar. The excitation wavelength with maximum absorption is $\lambda_{\mathrm{GFPexc}} = 490\,\mathrm{nm}$, the emission maximum is $\lambda_{\mathrm{GFPem}} = 510\,\mathrm{nm}$. GFP shows quantum yields up to 0.77 [79] and is stable up to 65 °C [80].

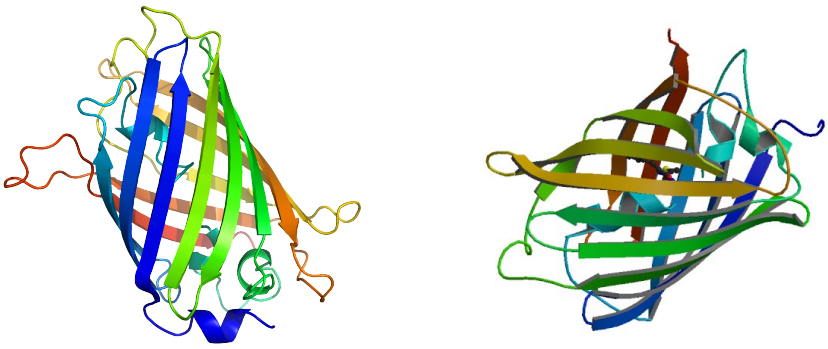

(a) (b)

Figure 17: X-ray structures of (a) Green Fluorescent Protein [75] (b) mCherry Protein [76]. These molecules are used as tracer particles.

An alternative available protein with similar size is mCherry from the coral “Discosoma sp” [81] with a molecular weight of ≈ 27 kDa [76], it shows fluorescence at higher wavelengths than GFP+ (fig. 18). Therefore it can be used with the 543 nm beampath.

5.2.3 Protein fluorescence

To characterize the used fluorescing particles, fluorescence spectroscopy measurements were performed on a *Jasco FP-6500* spectrometer. In addition to normal $I(\lambda)$ fluorescence intensity measurements at a fixed excitation wavelength, so called 3D-measurements are possible. At 3D-measurements different excitation wavelengths are used. The result of these measurements are depicted using a contour plot. Thereby, the maximum excitation/emission can be obtained easily. $\Delta\lambda_{exc}$ was 5 nm in all 3D-measurements.

The 3D plots (fig. 19 and 20) of the fluorescence intensity measurements for GFP+ and mCherry indicate, that the optimum available FCS laser-excitation-wavelength is the Argon-Ion 488 nm line for GFP+ and the 543 nm HeNe line for mCherry. The fluorescence spectra for the excitation with the laser corresponding wavelength are plotted in figure 18.

Both proteins are slightly smaller than the DFPase used for decontamination applications. But their main advantage, the fluorescence, gives the opportunity to observe the dynamics inside the water phase of a bicontinuous phase.

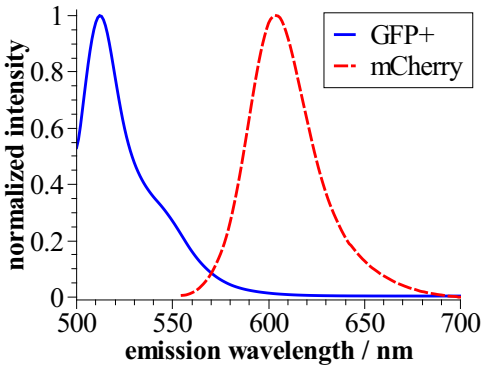

Figure 18: Fluorescence intensity of GFP+ with an excitation wavelength of 490 nm *and the maximum intensity at* 512 nm *and mCherry with an excitation wavelength of* 545 nm *and the maximum intensity at* 604 nm.

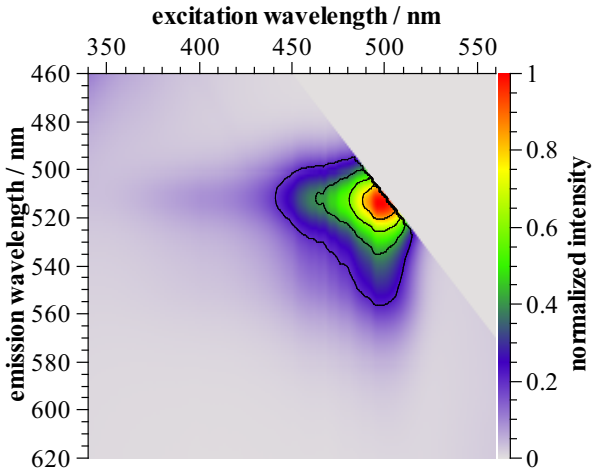

Figure 19: Fluorescence contour plot of the protein GFP+, with an excitation maximum $\lambda_{exc\text{-}max} =$ 490 nm *and emission maximum* $\lambda_{em-max} = 510\,\text{nm}$

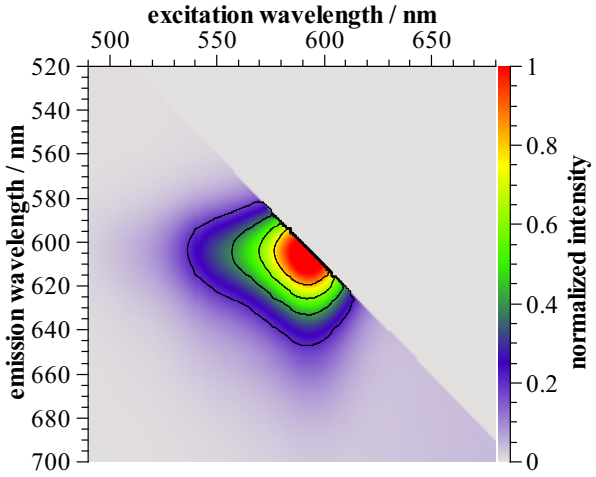

Figure 20: Fluorescence contour plot of the protein mCherry, with an excitation maximum $\lambda_{excmax} = 590\,\text{nm}$ *and emission maximum* $\lambda_{emmax} = 600\,\text{nm}$

5.3 Experimental details of the FCS measurements

The FCS measurements were performed with the *Zeiss Confocor 2* FCS-system. Usually a 0.5 ml sample was prepared and 60 µl were transferred into a sample holder, composed of two steele plates (one plate with a cover glass window, thickness 0.15 mm), compare figure 21, already introduced from H. Zettl [82] at the same FCS-system. The plates are fixed to each other by screws and an O-ring prevents the sample from evaporating. For measurements with GFP+, the excitation wavelength was 488 nm (argon-ion) and for octadecyl-rhodamin B the wavelength was 543 nm (helium-neon).

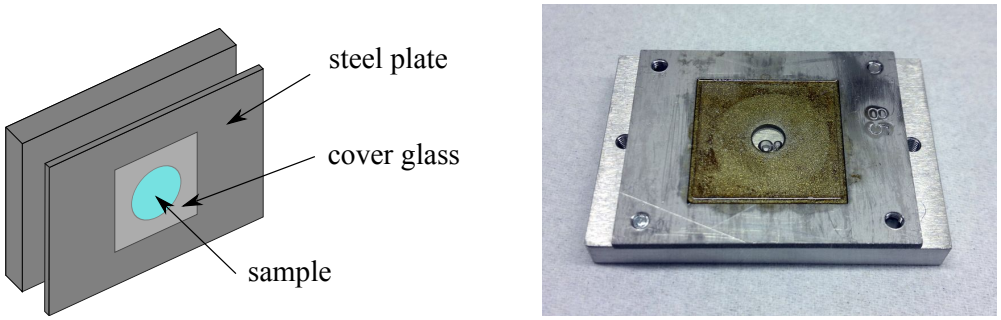

Figure 21: FCS sample chamber, composed of two steel plates with a glued on cover glass.

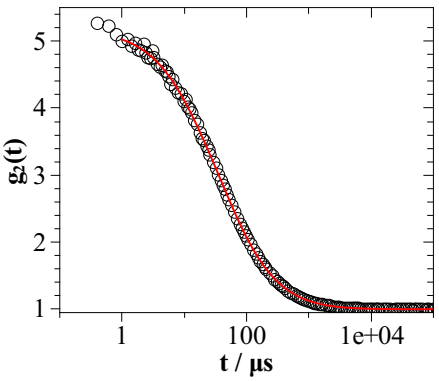

Figure 22: Calibration of the 543 nm *beampath with the dye rhodamin B*

The beam path of the FCS instrument has to be adjusted routinely. Therefore, the pinhole is shifted in the x-, y- and z-direction. This is done in three steps, first x, then y, then z, while the respective other values are hold constant. The intensity is measured during the pinhole is shifted and the positions yielding the maximum values are used for the measurements (compare fig. 23).

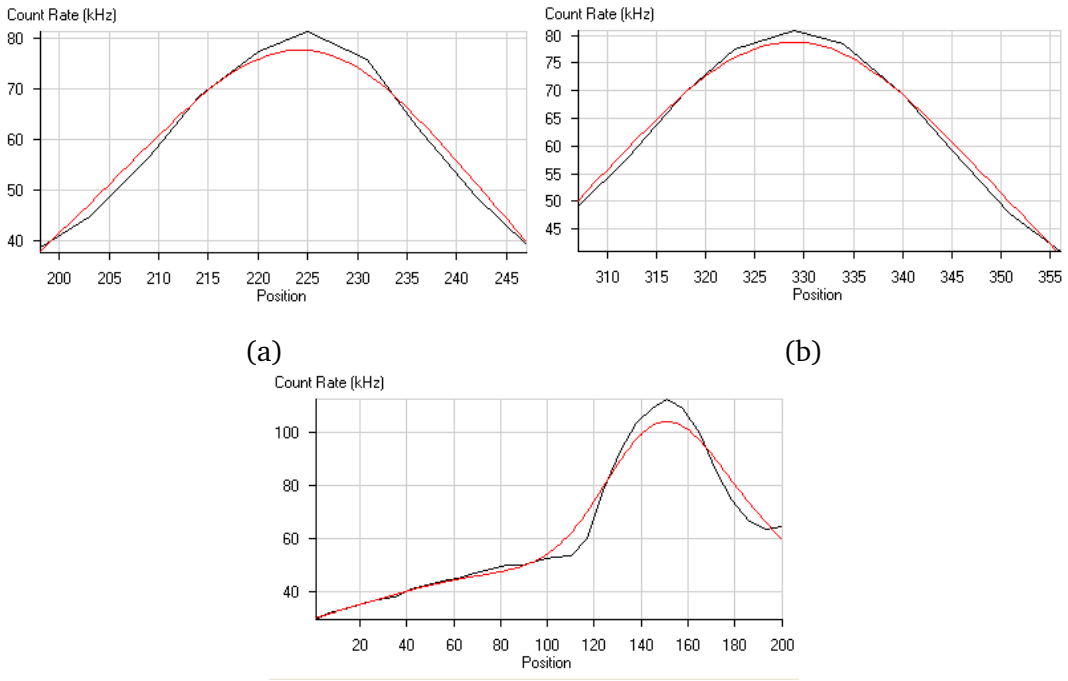

Figure 23: Confocor 2 pinhole adjustment with rhodamin B, (a) x-direction, (b) y-direction and (c) z-direction. The value with the maximum intensity is held constant for the measurements.

To determine the radius of the observation volume, a measurement is performed with a dye of known diffusion coefficient 22, for the 488 nm beampath this yields to $r_0 = 254$ nm and for the 543 nm beampath $r_0 = 261$ nm.

5.4 DLS measurements

For DLS measurements 1 mm samples were prepared and filled in a glass cuvette which is cleaned by ethanol to avoid scattering from dust particles. Measurements are performed at eleven different angles Θ in 10° steps between 40° and 140° with a measurement time of three minutes per angle at a laser wavelength of 543 nm. The laser intensity was adjusted to reach a sufficient countrate ($\approx$ 200 kHz) over the whole angular range. The obtained autocorrelation curves are treated with the CONTIN algorithm which results in different Γ for every Θ. q can be calculated from Θ and a $\Gamma(q^2)$ plot fitted linearly, leads to the diffusion coefficient D.

5.5 SANS/SAXS measurements

The structural dimensions in a microemulsion are on the nanometer scale. Therefore, only a few possibilities exist to investigate these structures. With photon correlation spectroscopy the hydrodynamic radius of geometrically simple objects like spheres would be easy to measure. But in the bicontinuous phase the structure is very complex. One possibility to observe such small structures is constituted by electron microscopy. For that the sample has to be frozen. The freezing process happens not instantly, the structure of the sample may change. Hence, a technique is necessary which enables the observation of the structure in situ.
SAXS is a scattering method with a wavelength much lower than visible light, the microemulsion structures can be measured. X-ray radiation is scattered by the electron shell of the atoms.
In a *SANS* measurement neutrons are scattered by the atom cores. Due to that, one can play with the deuteration of the sample: Either the oil or water component is deuterated, then the structures of the water/oil domains shine out (bulk dynamics), or the water and oil components are deuterated, then the surfactant interface is dominating the signal (film dynamics).
Based on experience, when the water component of a microemulsion is replaced by D_2O, the 1-phase boarder shifts to lower δ-values, which was already observed for C_iE_j microemulsions [83]. This circumstance has to be regarded when a sample is composed for neutron scattering. For droplet microemulsions it was already shown by Huang and Wu [84], that the replacement of H_2O by D_2O does not change the structure sizes of the droplets.
The theoretical basis for SANS and SAXS on the bicontinuous phase was introduced by M. Teubner and R. Strey [36]. The model which describes the scattering behavior of a bicontinuous phase is depicted in 4.5.4. The scattering intensity depending on the scattering vector q pictures a broad peak, where the domain size d and correlation length ξ can be obtained by fitting the data with the Teubner-Strey equation. The fits were performed with the Qtiplot [85] software using the Nelder-Mead Simplex, which generates a sequence of simplexes with decreasing diameter and accumulate around the desired minimum [86].

5.5.1 SAXS setup

The SAXS measurements were performed on a *SAXSLAB Ganesha* instrument [87] (fig. 24) at a sample - detector distance of 1.2 m. It is an inhouse SAXS system which offers a modern

high resolution 2D-*Pilatus* 300k detector, a rotating anode, a pinhole collimation system and a multiple sample holder with automatic alignment. The X-radiation scattered by the sample in an angle of Θ enters an evacuated volume, where a detector can be moved to tune the q-range and resolution. The detected 2D intensity "image" is averaged radially to obtain the intensity data depending on q.

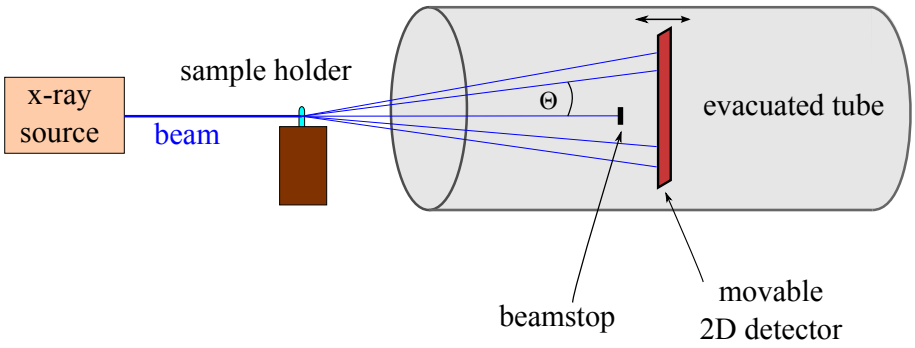

Figure 24: Setup of the Ganesha SAXS system. By moving the detector the observed scattering angle Θ *can be adjusted. In the sample holder more samples can be measured in a row.*

5.5.2 SANS setup

A neutron scattering instrument is comparable to a X-ray scattering setup. In most cases the neutron source is a scientific nuclear reactor, where several beamlines are provided with neutrons of different velocities depending on the experiment. In a small angle measurement, the distance between sample and detector is up to 40 m (D11 / ILL), the desired q-range can be tuned by the distance. The setup is shown in figure 25.

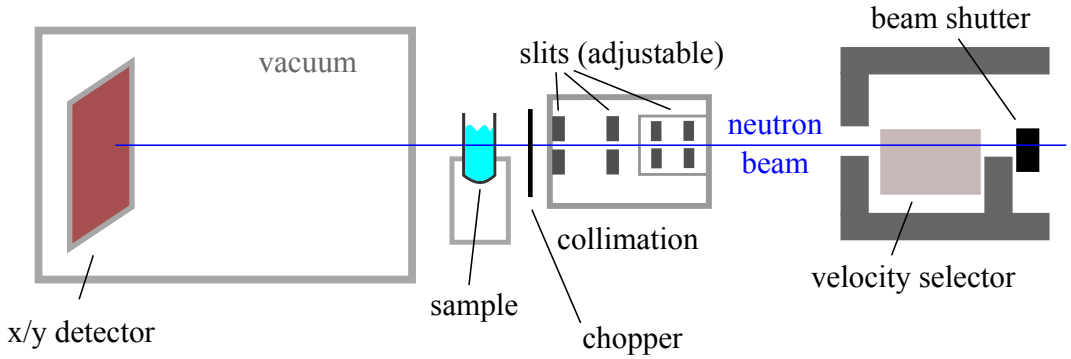

Figure 25: Principal setup of a SANS experiment using the example of the PAXY instrument (LLB Saclay / France, [88])

Normally the intensity is measured for three different distances to obtain a good resolution over the whole q-range. The data evaluation is fundamentally comparable to SAXS scattering, the result is an intensity $I(q)$ plot which can be approximated with an appropriate model.

6 Results and discussion

6.1 Fluorescence measurements

First of all, the problem of fluorescent impurities using sugar surfactant systems will be discussed. Afterwards, the structures of microemulsion systems will be characterized by SAS measurements and finally, diffusion measurements of GFP+ inside the water phase of different bicontinuous structures are shown.

6.1.1 Fluorescent impurities

A central complexity in the work with microemulsions based on a sugar surfactant is the existence of fluorescent impurities. Sugar surfactants and co-surfactants exhibit a weak fluorescent activity in the visible range. FCS and fluorescence spectroscopy measurements show, that the concentration of the impurity-molecules is in the range of $10^{-7} - 10^{-8}\,\mathrm{mol/l}$. This is a problem, because it's an appropriate concentration for FCS-measurements.

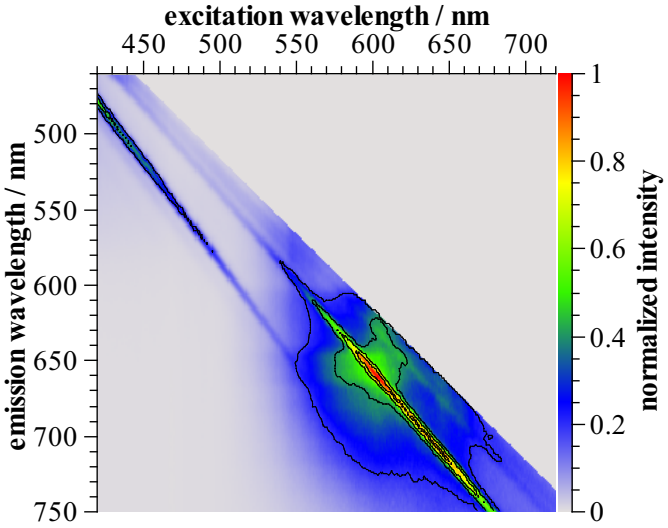

Figure 26: Contour plot of the fluorescence intensity of 1-pentanol in the excitation range from 400 nm *to* 800 nm *without fluorescent label.*

In fig. 26 the fluorescence spectrum of 1-pentanol is shown. No fluorescent label was added to the sample, but still a broad fluorescent activity nearly over the whole visible range is detectable. The lines in the 3D plot reveal Raman scattering, not fluorescence.

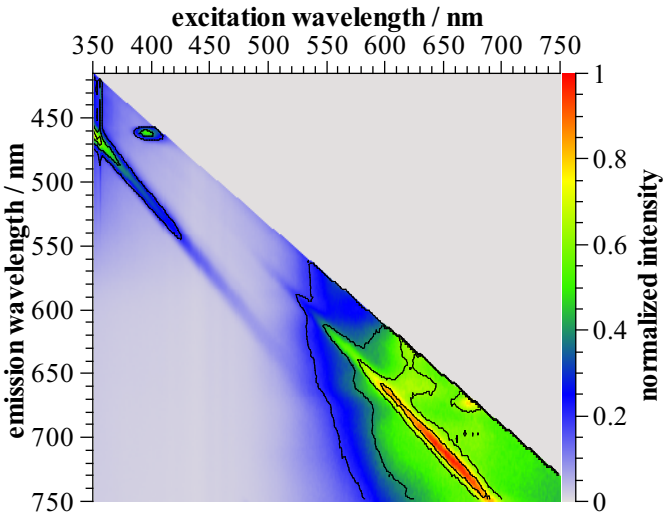

Figure 27: Contour plot of the fluorescence intensity of a C_9G_2 *solution (1 mol/l). Significant fluorescence from* $\lambda_{ex} = 500\,\text{nm}$ *over a broad emission range.*

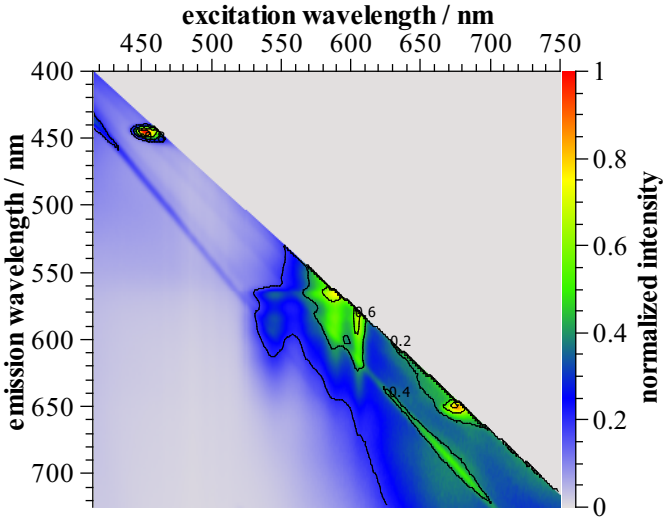

Figure 29: Contour plot of the fluorescence intensity of a $C_{12}G_2$ *microemulsion. Several fluorescence emission peaks appear and indicate fluorescent impurities.*

Fluorescence measurements of different sugar surfactants (fig. 27 and 28) show an activity, although the molecules have no fluorescent characteristics. Therefore this activity stems from impurities which are most likely introduced during the production processes of these sugar surfactants. Even 1-pentanol is contaminated. Different purification methods effected no improve-

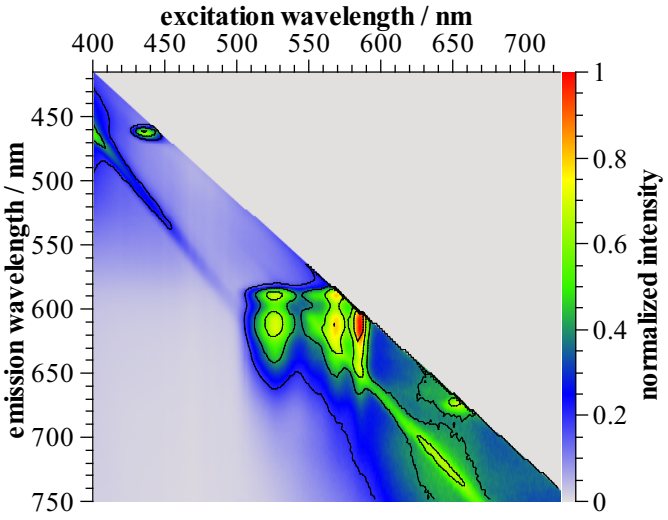

Figure 28: Contour plot of the fluorescence intensity of a $C_{12}G_2$ solution (1 mol/l). Several fluorescence emission peaks appear and indicate fluorescent impurities.

ment: Fractionated distillation, activated carbon treatment and fluorescence bleaching. A minimization of the disturbance of the FCS measurements caused by impurities can be achieved by using a quite high concentration of fluorescent particles , $c_{\text{fluo}} = 10^{-7}\,\text{mol/l}$ This concentration is not too low for a sufficient autocorrelation value. Indeed the measurements of a fluorescent particle in a microemulsion will show the fluorescent background of the microemulsion components, but a 2-component fit is a possibility to account for this additional mode. In addition, the FCS-countrate of a pure microemulsion is about a factor of 10 lower compared to the countrate in the presence of GFP+ at the same laser intensity, therefore the interference of the microemulsion background is low. Furthermore the fluorescence spectroscopy measurements show mainly fluorescence activity starting at an excitation wavelength of 520 nm, which justifies the choice of an excitation wavelength of 488 nm for the FCS measurements and to make use of the protein GFP+.

6.1.2 FCS measurements

Until now, only a few works deal with FCS technique for studying the dynamics of microemulsions [89, 90], although it is a powerful technology with promising different application areas related to microemulsions.

Characterization of the FCS setup

Before performing measurements with a tracer particle, whose diffusion dynamics have to be measured, the FCS setup has to be calibrated. For that reason, a well explored molecule like *rhodamine 6G* or *fluorescein* is measured in aqueous solution. With the known diffusion coefficient, the radius of the confocal volume can be calculated. This has to be done for all used beampaths, in this work for 488 nm and 543 nm.

Diffusion of the microemulsion structure

Due to the impurities discussed in chapter 6.1.1, a pure microemulsion sample already shows autocorrelation in a FCS measurement with a small count rate. The sample can also be labeled with *Octadecyl-Rhodamine B chloride*, which is an amphiphilic molecule because of the long C-chain as a lipophilic part and the hydrophilic Rhodamine B headgroup. Therefore, the molecule binds to the surfactant interface and reflects the structural dynamics. Measurements of the pure microemulsion compared to measurements of a labeled microemulsion show, that there is nearly no difference in the diffusion time. For that reason, the fluorescent impurities are also located in the surfactant interface and reflect the microemulsion dynamics, too.

Self diffusion of fluorescent proteins

To characterize the diffusion behavior of GFP+ and mCherry and to exclude the occurrence of agglomeration, first the self diffusion in buffer is measured by FCS. Fig. 30 shows the FCS measurements for GFP+ in buffer, the fit results in a diffusion time $\tau_D = (137 \pm 6)\,\mu s$ and a diffusion coefficient D of $(1.29 \pm 0.41 \cdot 10^{-10})\,m^2/s$. This indicates that only one component is present in the system, so no agglomerations processes occur. This result is in very good agreement to the literature [91].

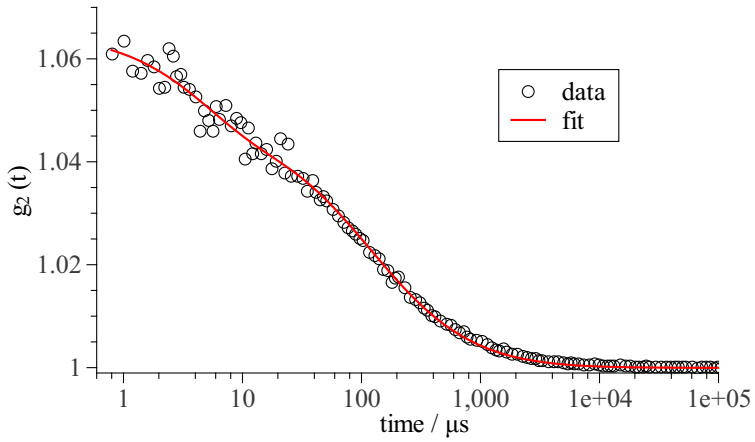

Figure 30: FCS autocorrelation data of GFP+ in buffer, the red line represents a fit with eq. 16

The FCS measurements of the protein mCherry show a slightly larger decay time in the autocorrelation curve (compare fig. 31). A 1-component fit does not match the measured data. Therefore, a 2-component equation (19) has to be used. The successful fit leads to two diffusion times, 78 µs and 739 µs, which indicates the presence of a much bigger diffusing component. This is a hint for emerging agglomerates.

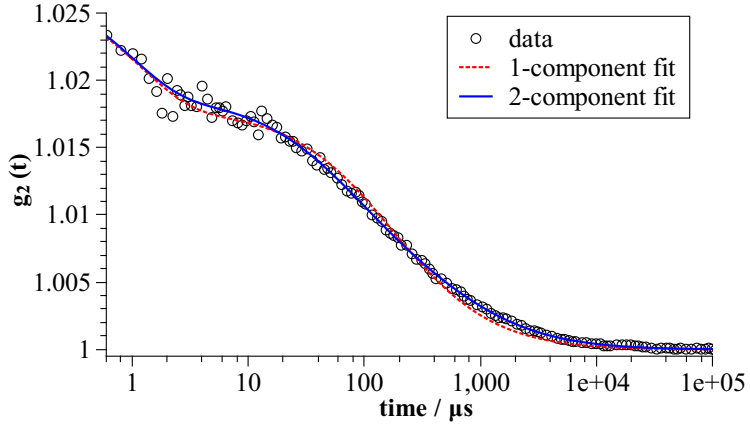

Figure 31: FCS autocorrelation data of mCherry in buffer, the red dashed line represents a fit with eq. 16 (one fluorescing component), the blue line is a fit with eq. 19 (two fluorescing components).

BSA (Bovine Serum Albumin) labeled with fluorescein or Texas red, widely used in scientific studies, was another candidate for diffusion experiments, because of it's high availability and low price. It has a mass of around 65 kDa, which is two times higher than GFP+ with a radius

of approximately 3.5 nm [92]. FCS measurements yielded no diffusion inside microemulsions, besides in the event of a labeled protein unlabeled dye molecules are present, which influence the FCS measurements. Thus GFP+ is the first choice for observing protein diffusion in a microemulsion.

6.2 The C_9G_2 based microemulsion system

This system is composed of water, cyclohexane, C_9G_2 (fig. 32) as surfactant and 1-pentanol as co-surfactant. The amount of co-surfactant is used as a tuning parameter and the system will be observed at different oil/water ratios Φ, hence, the size of the water domains can be tuned.

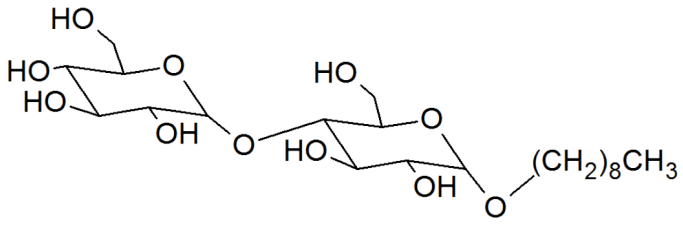

Figure 32: Chemical structure of n-nonyl-β-D-maltosid

C_9G_2 shows a good solubility in water because of the glucose headgroups. This system is used as a model system with a high purity of $> 99\%$ to minimize fluorescence, avoid fluctuations in the production process and preclude different kinds of impurities.

6.2.1 Phase behavior

The sugar surfactant n-nonyl-β-D-maltopyranosid (C_9G_2) with co-surfactant 1-pentanol exhibits a broad 1-phase region with a lamellar phase at high γ (figure 33). At $\Phi = 0.5$, the X-Point is located at $\gamma = 0.105, \delta = 0.12$. With rising amount of surfactant, the one phase region gets wider with respect to the δ-direction.

As expected, the X-points move to lower γ and δ values by decreasing Φ and picture a parabolic pathway. This was already observed for C_iE_j-surfactants by Sottmann and Strey [93]. Furthermore, the γ-width of the 1-phase area decreases when going to higher or lower Φ. Systems with such a small 1-phase area are difficult to handle, especially when cyclohexane is used as oil component. The evaporation of only small amounts of oil can cause a slide into a 2-phase region. Such samples have to be handled carefully.

The structure of this system was observed by small angle scattering experiments and the dynamics by FCS. The samples for the measurements at different oil/water ratios Φ were composed directly behind the X-points in the 1-phase region (compare table 1). At this point the structure is most likely bicontinuous, the higher γ, the more droplet-like structures arise.

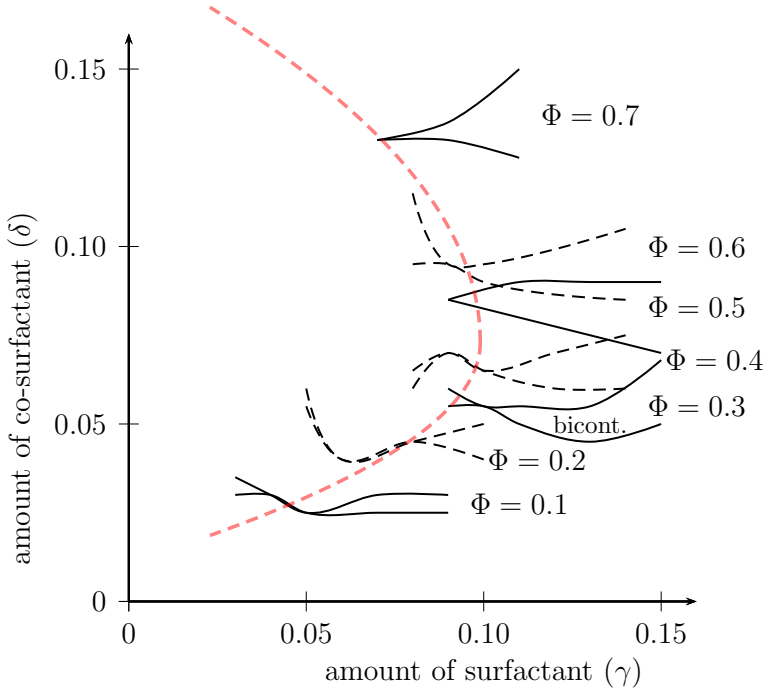

Figure 33: Phase diagrams of the C_9G_2 system for different oil/water ratios Φ, the connection of the X-points describe a parabolic trajectory.

Table 1: Composition of the C_9G_2 microemulsion samples for SAS and FCS measurements

oil/water ratio α	surfactant amount γ	alcohol content δ
0.1	0.08	0.035
0.2	0.11	0.055
0.3	0.12	0.075
0.4	0.14	0.10
0.5	0.12	0.105
0.6	0.12	0.145
0.7	0.11	0.17

6.2.2 Structure sizes

Length scales by SANS

The structure of the presented C_9G_2 system was investigated by scattering methods applied to the samples shown in table 1. The SANS measurements were performed in Saclay/France at

the LLB (Laboratoire Léon Brillouin) and in Berlin at the HZB (Helmholtz-Zentrum-Berlin). The intensity curves shown in figure 34 exhibit a structure peak for oil/water ratios of 0.3 to 0.5. The Teubner-Strey approximation is only suitable for volume fractions close to 0.5, which applies for the $\Phi = 0.3$ to 0.5 samples. Then the correlation length and domain size can be calculated from the fit parameters, discussed in chapter 4.5.4. The results are shown in table 2.

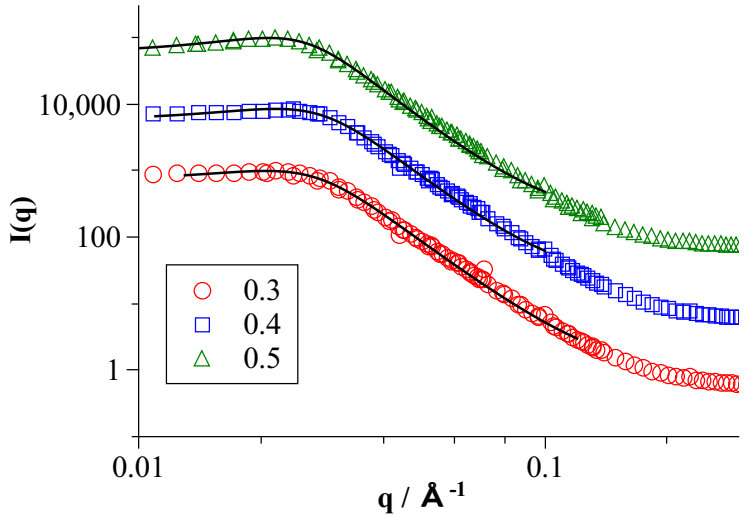

Figure 34: SANS intensity measurement of C_9G_2 microemulsions with varying Φ. The data was treated with the Teubner-Strey approximation. The fitting results are represented by the solid lines.

As a consequence of the deuterated water phase, ξ reflects the correlation length of the oil domains. ξ increases for rising Φ, in return, the water domains shrink (fig. 35). The domain size d stays nearly constant around 25 nm, which reflects the repeating length of the oil and the water domains together. The water domain size could be estimated by subtracting the correlation length from the domain size, but then the surfactant interface is not regarded.

Table 2: Structure sizes for C_9G_2-microemulsions determined by SANS

oil/water ratio Φ	volume ratio	correlation length ξ /nm	domain size d /nm
0.3	0.35	7.7	25.9
0.4	0.46	8.2	24.7
0.5	0.56	9.3	26.7

Also for smaller values of Φ SANS measurements were performed, the intensity curves are shown

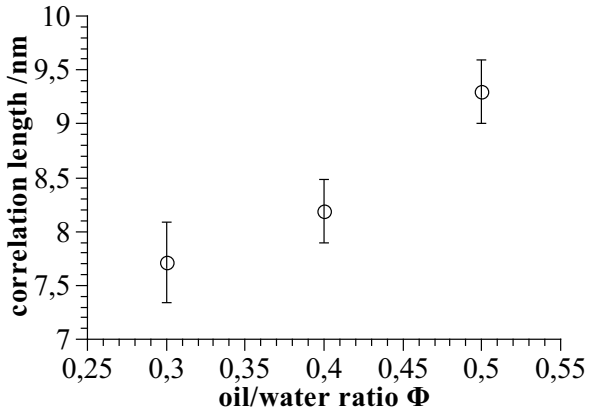

Figure 35: Correlation length which results from the Teubner-Strey approximation for the C_9G_2 *system depending on the oil/water ratio* Φ*. The increase with rising* Φ *means growing oil domains, therefore shrinking water domains.*

in fig. 36. No peak arises in the $I(q)$ plot, therefore Teubner-Strey model is not appropriate. Another way to extract information from the measurements at smaller Φ without structure peak is to take advantage of the Guinier law: The SANS data in a double logarithmic plot follows a linear decrease at low q-values (Guinier-regime) [94].

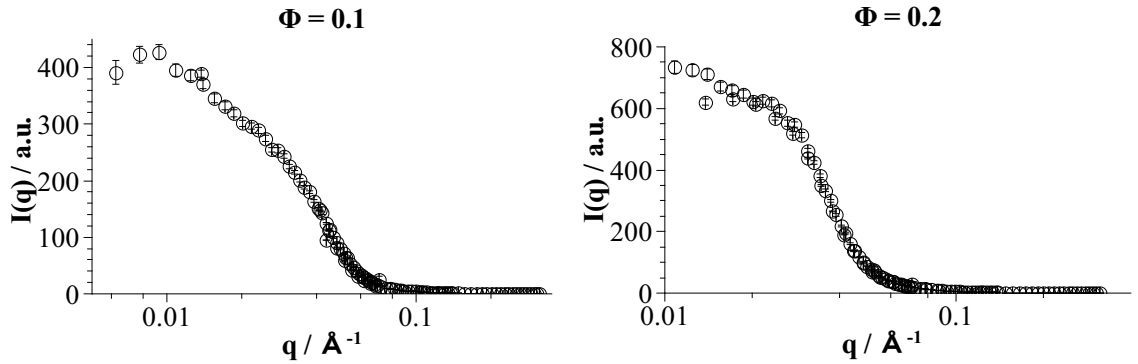

Figure 36: SANS intensity measurement of C_9G_2 *microemulsions with variing* Φ*. The data cannot be fitted with the Teubner-Strey model.*

Table 3: Results from the scaling analysis in fig. 37 for the system C_9G_2 with the resulting slope depending on Φ

Φ	slope m	structure
0.1	-0.64	ellipsoidal
0.2	-0.25	ellipsoidal/spherical
0.7	-0.71	ellipsoidal/cylindrical

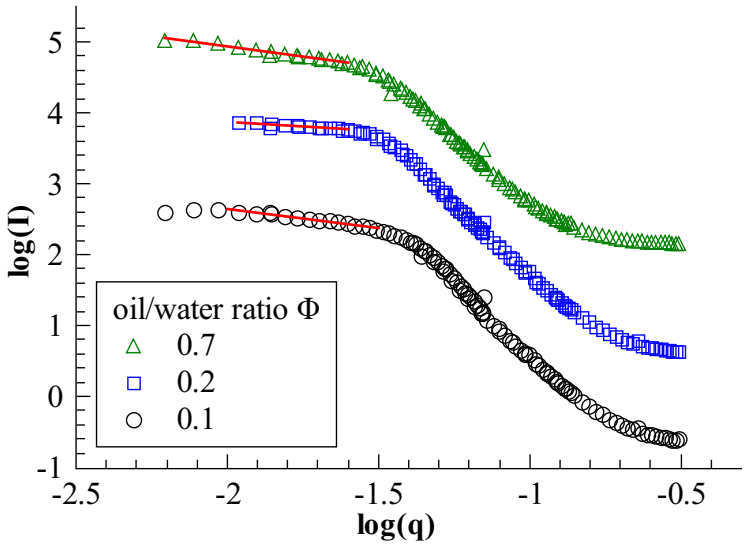

Figure 37: Double logarithmic plot of the SANS measurement of C_9G_2 microemulsions with varying Φ. The slope in the low q-range indicates the shape of observed structure.

The slope in the Guinier-regime shows, what structure is present in this microemulsion samples. Because of the oil/water ratio oil droplets inside a continuous water phase for small values of Φ and water droplets inside an oil continuous phase for high values of Φ occur. The logarithmic plots of the intensity curves are shown in fig. 37. While a slope $m = -1$ indicates cylindrical objects, $m = 0$ means spherical particles and a slope m of 0 to -1 implies ellipsoidal objects. In the C_9G_2 system m is approx. -1 for $\Phi = 0.1$ and 0.7 and near 0 for $\Phi = 0.2$, compare table 3.

Length scales by SAXS

In addition to the SANS observations, also SAXS investigations were performed to verify the SANS results. The electron density is crucial for the scattering process of X-rays. The electron

distribution is different for water domains, oil domains and the surfactant film. In contrast to neutron scattering experiments, where the deuteration is important for the scattering contrast, the electron density cannot be varied without changing the solvents and therefore changing the structure of the microemulsion system.

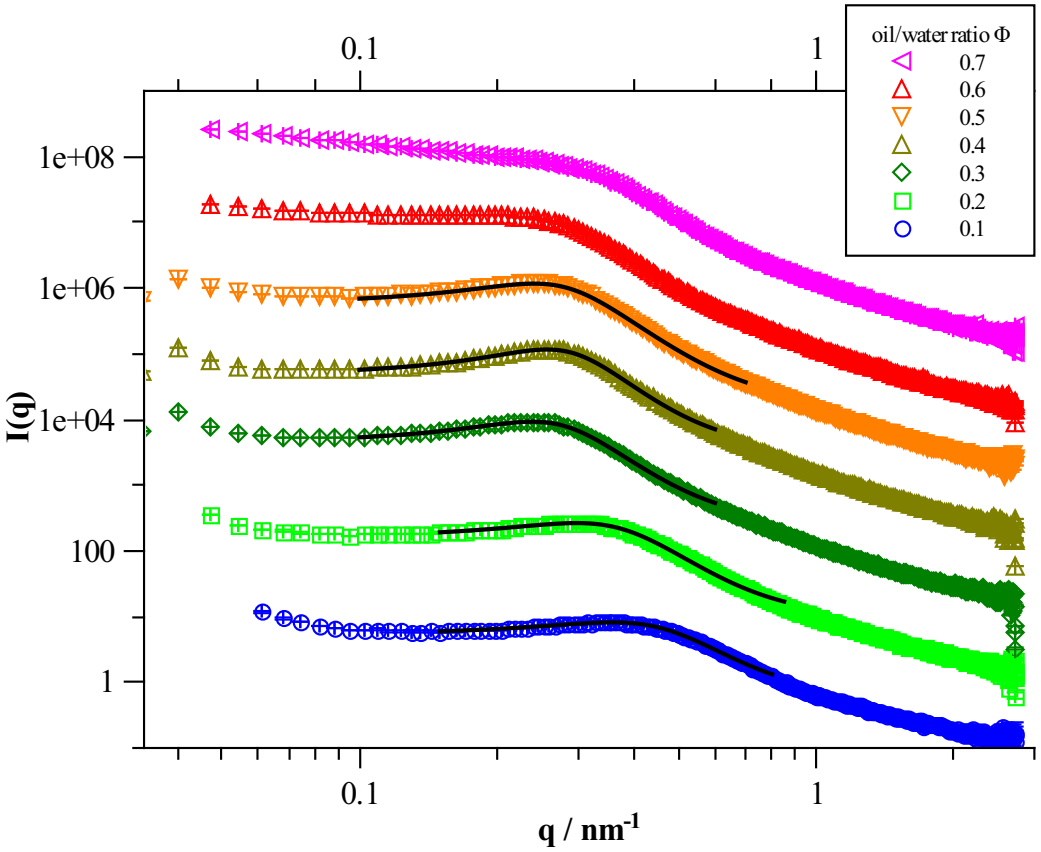

Figure 38: SAXS measurements of series of the different microemulsion C_9G_2 samples with different Φ. *The lines represent fits according to the Teubner-Strey approximation, which is not possible for* Φ *0.6 and 0.7. The intensity of the* Φ *0.2 . . . 0.7 was shifted for clarity reasons.*

For the measurements samples identical to SANS were used (table 1). The intensity curves shown in figure 38 are again fitted with the Teubner-Strey approximation, the results are summarized in table 4. Compared to the SANS results of the analogous samples, the domain sizes obtained from the SAXS measurements are similar. The correlation lengths differ because the deuteration of the water phase in the SANS samples implies, that the correlation length values apply to the oil domains. However, in a SAXS measurement, the oil or water domains cannot be

Table 4: Structure sizes for C_9G_2-microemulsions determined by fitting the SAXS data with the Teubner-Strey approximation.

oil/water ratio Φ	volume ratio	correlation length ξ /nm	domain size d /nm
0.1	0.12	4.55	15.11
0.2	0.24	6.11	18.45
0.3	0.35	9.77	24.21
0.4	0.46	10.27	22.85
0.5	0.56	9.25	23.79

clearly separated. The SAXS-result trend in figure 39 is in good accordance to the SANS results, there is only a small deviation due to the different scattering contrasts.

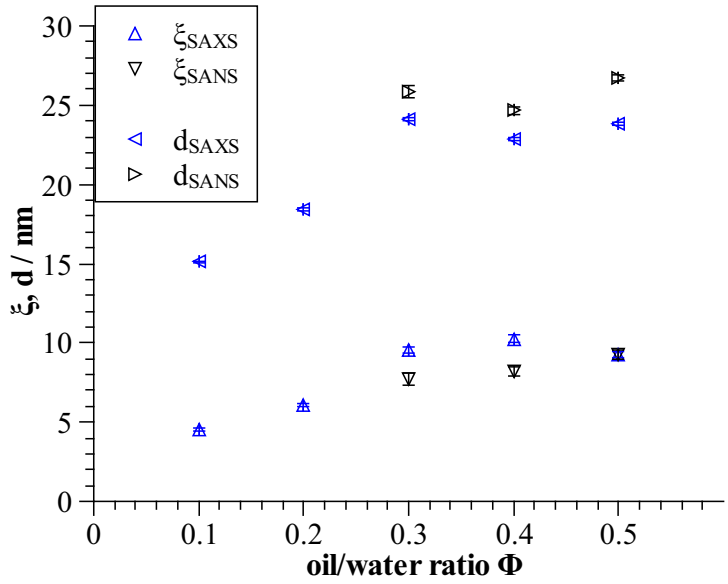

Figure 39: C_9G_2 microemulsion domain sizes d and correlation lengths ξ derived from the Teubner-Strey approximation compared to the SANS results of chapter 6.2.2.

6.2.3 GFP+ dynamics by FCS

The correlation lengths of nearly 10 nm for the oil phase (comp. table 4) imply a similar value for the water domains at $\Phi = 0.5$. These lengths are still big enough to allow diffusion of GFP+ with a diameter of approximately 5 nm. However, the domain size of the water domains is already sufficiently low to produce a notable confinement or crowding effect for the protein. Hence, for the analysis if the data the model introduced by Weiss has to be used [56].

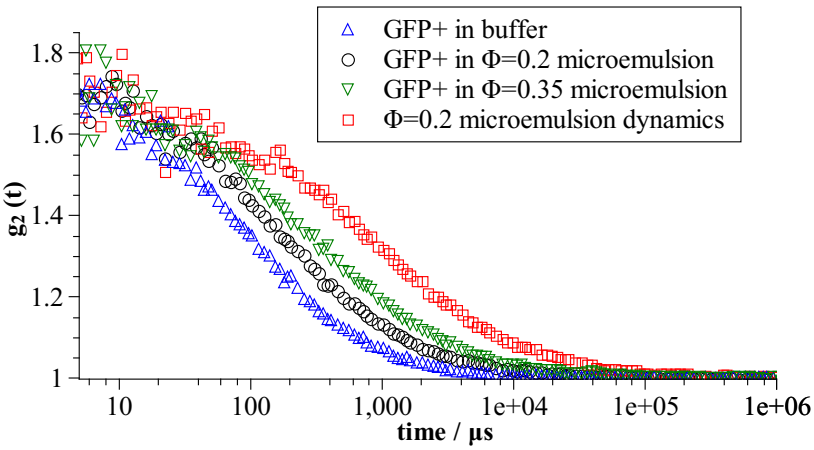

Figure 40: Comparison of FCS autocorrelation curves for GFP+ in a C_9G_2 microemulsion. GFP+ shows a slightly slower diffusion inside the water phase of the microemulsion, but faster than the microemulsion dynamics. The protein is non-polar and mainly hydrophilic. Therefore it is confined to the water domains of the microemulsion.

Figure 40 shows autocorrelation curves for the C_9G_2 system. The protein is able to move inside the water domains, and the diffusion is slower in a bicontinuous structure (Φ 0.3), than in a water continuous structure (Φ 0.1). As expected, the diffusion is hindered by the confinement of the water domains. Crowding effects take place for Φ 0.1, where oil-in-water structures (see table 3) appear, which already results in a slowed diffusion at this low value of Φ compared to GFP+ in buffer.

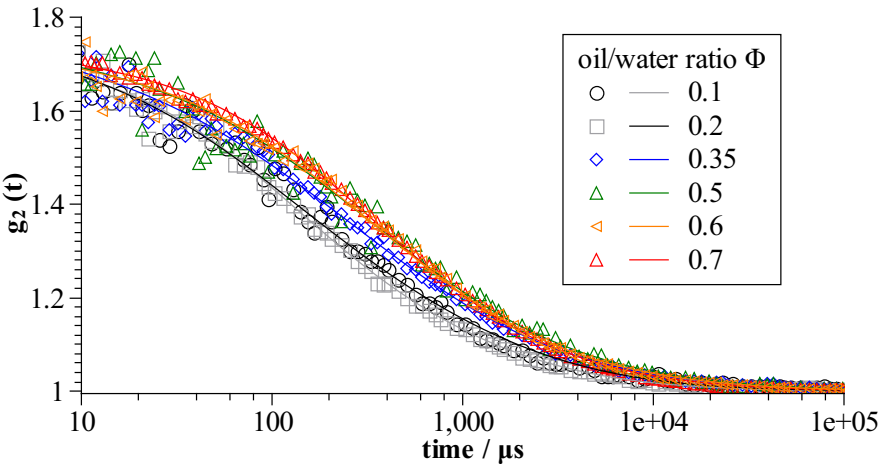

Figure 41: GFP+ FCS autocorrelation curves inside the water domain of the C_9G_2 microemulsion for different Φ. With rising Φ the curves move to bigger timescales. The lines indicate fits according to equation 21.

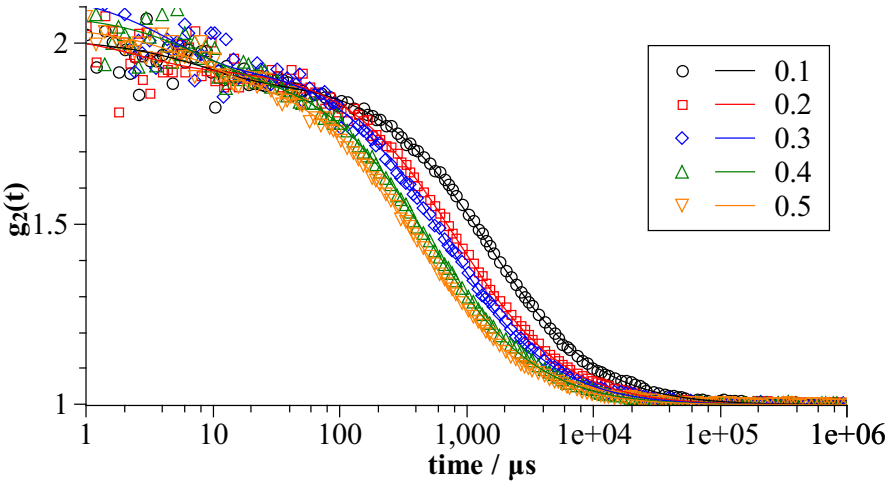

Figure 42: Normalized FCS autocorrelation curves of the C_9G_2 microemulsion for different Φ labeled with octadecyl-rhodamin B. With rising Φ the curves move to smaller timescales. Octadecyl-rhodamin B is amphiphilic and incorporates in the interface. The lines indicate fits according to equation 16.

autocorrelation curves shifting to bigger timescales (figure 42). In fig. 43 the diffusion times τ_{sub} of GFP+ are plotted. The data was fitted with an anomalous diffusion model (equation 21).

For small Φ the diffusion is nearly as fast as in dilute solution.

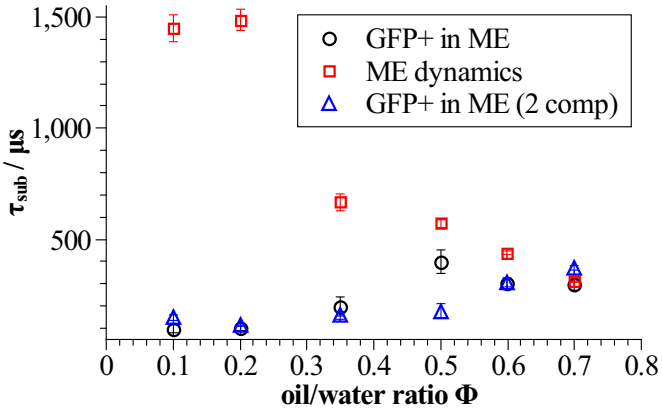

Figure 43: Subdiffusion times τ_{sub} of GFP+ in the water phase of a C_9G_2 microemulsion, calculated from the fit of the FCS autocorrelation curves.

In the range $\Phi = 0.3$ to 0.5, the structure changes to bicontinuous and the diffusion is hindered by the sponge like phase. At $\Phi = 0.6$ and 0.7 τ_{sub} is constant and reflects the dynamics of the microemulsion structure - this is an indicator for the confinement of the protein, it seems to be stuck in the microemulsion and participates in the collective motion of it. When comparing the autocorrelation curves of the microemulsion dynamics and the GFP+ autocorrelation curves in a microemulsion, the GFP+ curves look more shallow. This is an indicator for anomalous diffusion [95]. The anomalous diffusion exponent α can also be extracted from the fit.
Fig. 44 shows the anomalous diffusion exponent. At small Φ α is nearly 1, the protein is hardly confined by the microemulsion structure, which is more droplet-like (slightly elongated drops, see SANS results) than bicontinuous for $\Phi = 0.1$ and 0.2. When the structure is bicontinuous starting at $\Phi = 0.3$, α decreases rapidly and indicates, that the protein is confined by the water domains. From $\Phi = 0.6$ on, α increases again, which shows, that the protein gets now stuck in the structure and participates in the diffusive breathing motion of the microemulsion matrix.

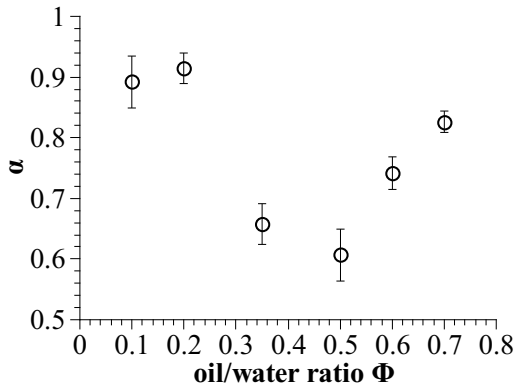

Figure 44: Anomalous diffusion parameter α for GFP+ in the C_9G_2 system. With an $\alpha < 1$ subdiffusion is observed, especially for $\Phi > 0.2$.

6.2.4 Microemulsion dynamics by DLS

When performing DLS measurements, one has to consider, that microemulsions show especially in the case of a bicontinuous phase the so called “breathing motion”. Therefore, only a diffusion coefficient can be calculated. The Stokes-Einstein equation cannot be applied in this case. Only at very low or high Φ, the structure changes from a bicontinuous phase to oil droplets in a continuous water phase or water droplets in an oil continuous phase, respectively. Nevertheless, information regarding the collective breathing motion can be obtained from the diffusion coefficient D [96, 97].

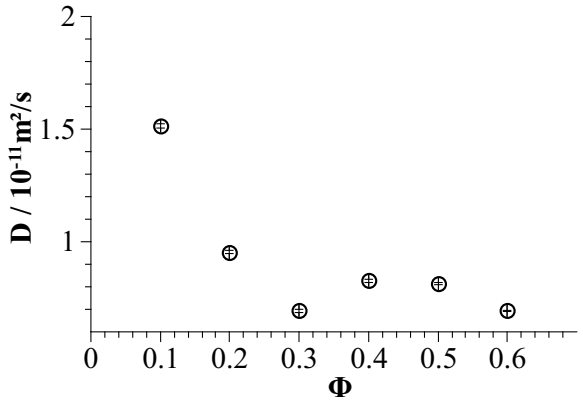

Figure 45: DLS diffusion coefficients D_{DLS} for the C_9G_2 microemulsion system at different oil/water ratios Φ. D_{DLS} decreases rapidly from Φ 0.1 to 0.3, which indicates a change in the structure from oil droplets in a water continuous phase to the bicontinuous phase.

The diffusion coefficients indicate, that there is a structural change from Φ 0.2 to 0.3, which was already observed by SANS measurements. At small Φ values, the structure is more droplet like, with small oil amounts a sponge-like structure is not possible. At higher Φ it changes to a bicontinuous structure, when the oil amount is high enough to form a cross-linked structure.

6.3 The $C_{12}G_2$ based microemulsion system

The sugar surfactant n-dodecyl-ß-d-maltosid has a longer C-chain than C_9G_2, which leads to different structural sizes and another phase behavior tending to a broad lamellar phase. This system is composed of water, cyclohexane, $C_{12}G_2$ and 1-pentanol.

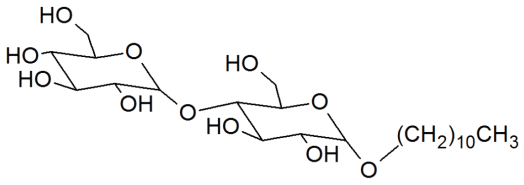

Figure 46: Chemical structure of n-dodecyl-ß-d-maltosid

The water solubility of $C_{12}G_2$ is below C_9G_2 because of the longer C-chain. The measurement of the phase diagrams takes much more time because of the low solubility and the broad 2-phase lamellar regions.
To learn about length scales and structures in this system, again SANS and SAXS measurements were performed. The composition of the measured samples is shown in table 5.

6.3.1 Phase behavior

In contrast to the C_9G_2 based system the $C_{12}G_2$ microemulsion system exhibits a broad lamellar region. 1-phase structures appear only in a small gap between the 2-phase region and the lamellar domain at higher γ (compare fig. 47). Figure 48 indicates, what point in the phase diagram was used for the sample composition.

The X-points shift to smaller δ and γ, which was already observed in fig. 33 for the C_9G_2 system. The hyperbolic trajectory is indicated by a dashed line. Because of the small 1-phase area this system is not relevant for applications. But it shows relatively big structure sizes and a droplet structure (compare chapter 6.3.2) at low γ values. For example, in the C_9G_2 system, such a droplet structure would need high surfactant amounts of $> 25\%$. Comparable technical grade surfactants like *SL55* ($C_{12\text{-}14}G_{1.3}$) have a broader 1-phase area with a similar location of the X-point. The $C_{12}G_2$ system can be seen as a model system for a technical grade microemulsion.

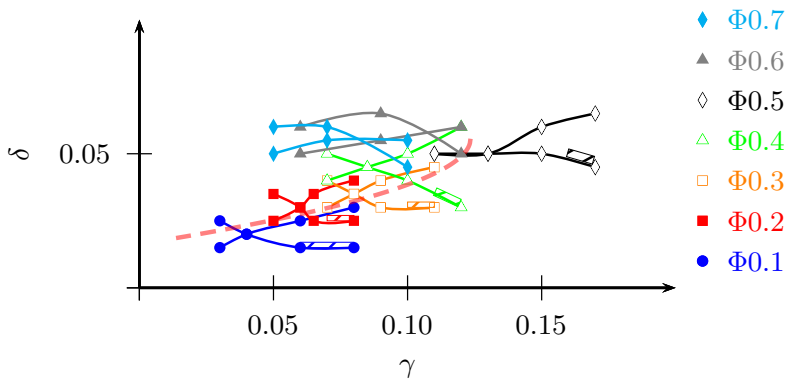

Figure 47: Phase diagrams of the $C_{12}G_2$ system for different Φ. The 1-phase area is only a small stripe between the 2-phase region (oil-in-water) and the lamellar region.

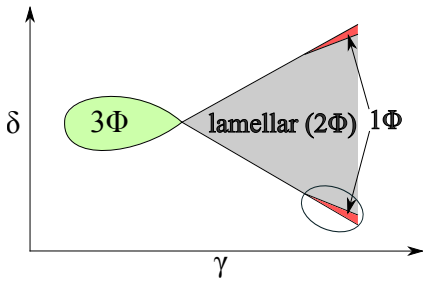

Figure 48: Idealized Kahlweit-fish phase diagram of $C_{12}G_2$. The samples were composed in the small 1Φ region (ellipse) below the broad lamellar area.

Table 5: Composition of the $C_{12}G_2$ microemulsion samples for the SAS and FCS measurements.

oil/water ratio α	surfactant amount γ	alcohol content δ
0.1	0.12	0.015
0.2	0.14	0.025
0.3	0.15	0.03
0.4	0.16	0.035
0.5	0.16	0.05
0.6	0.145	0.055
0.7	0.135	0.06

6.3.2 Size and shape of the microemulsion structures

Length scales by SANS

The SANS measurements were performed in Berlin at the HZB (Helmholtz-Zentrum-Berlin). SANS intensity curves are shown in fig. 49. The Teubner Strey model is not applicable. The data were fitted with a hard sphere form factor and polydisperse spheres using the SASfit-Software [63]. The results are written in table 6. With increasing Φ the droplet radius grows. The volume fraction also increases, but the value for Φ 0.5 is not appropriate compared to the real oil/water volume ratio. For small oil amounts the hard sphere model is suitable. At higher Φ the droplets assume other shapes (elliptic, cylindrical) or interconnect with other droplets. With rising Φ, the structure peak gets more pronounced.

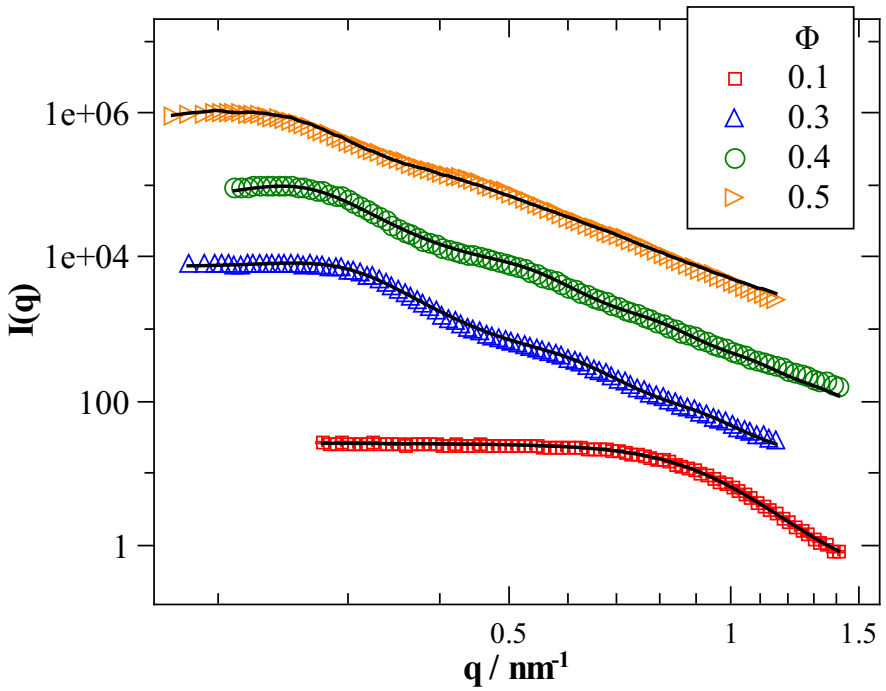

Figure 49: SANS measurement of $C_{12}G_2$ microemulsions with varying Φ. The lines are approximations with a hard sphere form factor and polydisperse spheres with the SASfit-software [63].

The linear dependence in the Guinier regime of the double logarithmic plot was verified for Φ 0.1. Contrary to the small Φ SANS measurements on C_9G_2 with a tendency to elliptic shapes, $C_{12}G_2$ forms spherical micelles indicated by a slope at low q, which is approximately 0 within the experimental precession (-0.10 ± 0.01, fig. 50). This result can be explained taking into

Table 6: Structure sizes for $C_{12}G_2$-microemulsions determined by SANS

oil/water mass ratio Φ	volume ratio	volume fraction (fit)	droplet radius / nm
0.1	0.12	0.15	3.27
0.3	0.35	0.25	10.07
0.4	0.46	0.27	11.57
0.5	0.56	0.21	12.70

account that the system shows a broad lamellar phase without a 1-phase region behind the X-Point. Therefore the samples were positioned in the 1-phase gap below the lamellar region. In this part of the phase diagram droplet structures are expected.

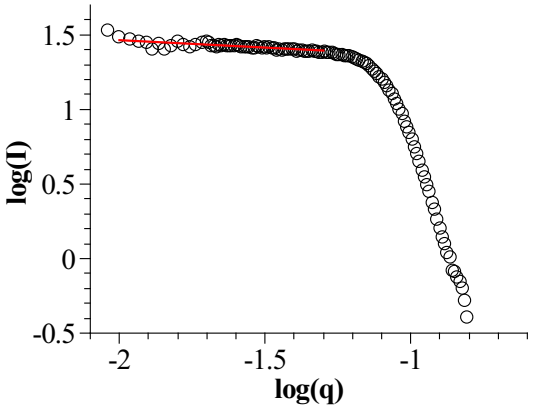

Figure 50: SANS measurements of $C_{12}G_2$, $\Phi = 0.1$ microemulsion, the linear fit of the double logarithmic plot results in a slope of -0.10 ± 0.01. This indicates spherical oil-micelles inside a continuous water phase.

Length scales by SAXS

In contrast to the SANS measurements the SAXS curves (fig. 51) show a structure peak also for samples with $\Phi = 0.1$ and 0.2 followed by a shoulder at higher q. Hence, no bicontinuous phase is present, but a concentrated droplet oil-in-water phase.

The data in figure 51 were fitted with a hard sphere structure factor and a polydisperse Schulz-Zimm distribution of the spheres [98]. The analysis was done using Otto Glatters GIFT software package ([64, 65]) and agrees very well with the experimental data. Also the data from the sample with $\Phi 0.7$ was analyzed in the same way. However, at this high concentration of oil the model does not fully describe the system and the result is only given for the sake of completeness.

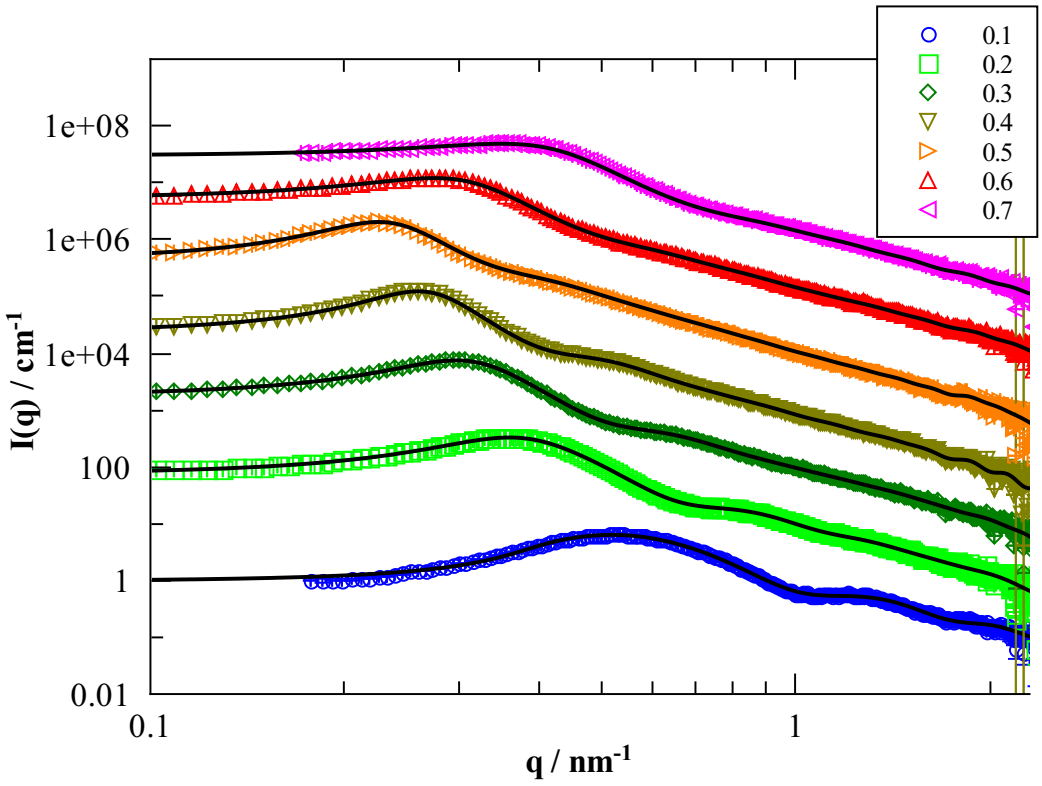

Figure 51: SAXS measurements of microemulsion $C_{12}G_2$ system with different oil/water ratios Φ. The lines are approximations with a hard sphere form factor and polydisperse spheres with the GIFT-software [64, 65].

Volume fraction and droplet radius obtained from the GIFT analysis is depicted in figure 52. The droplet radius increases with Φ because of the rising amount of oil in the system. Also the volume fraction rises, at Φ 0.5 the fraction is ≈ 0.5 which is in good agreement to the oil amount

of 0.56. At Φ 0.6, the radius and the volume fraction suddenly drop to much smaller values. This is due to the inappropriate fit or a structural change to water droplets in an oil continuous phase.

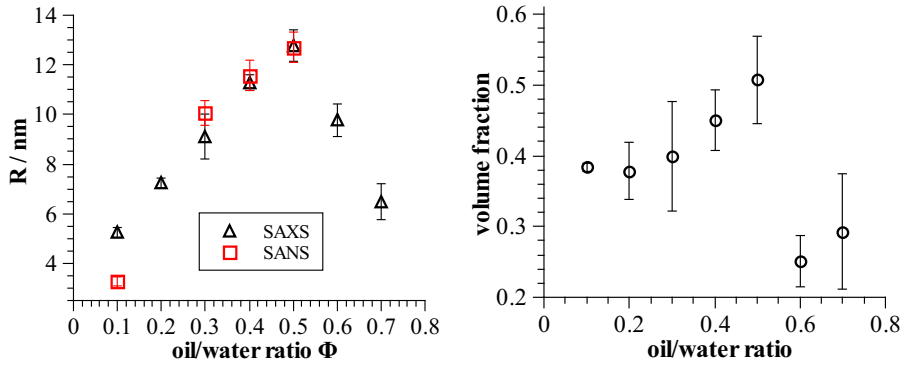

(a) (b)

Figure 52: Results of the GIFT analysis for the $C_{12}G_2$ microemulsion samples, (a) sphere radius R (SANS and SAXS values), increases due to the rising amount of oil and decreases for Φ 0.6 and 0.7 (b) volume fraction of the spheres (SAXS), increases as well up to $\Phi = 0.5$.

The SAXS droplet radius results are in good agreement with the SANS outcomes, except for the Φ 0.1 value. This could be connected to the diverse scattering contrasts and the different analysis methods. The polydispersity is nearly constant at approximately 20%, which is in good agreement with the results of comparable C_iE_j systems [98].

6.3.3 GFP+ dynamics by FCS

The SAS results indicate, that the structure is not bicontinuous, the oil component is located as droplets in a water continuous phase, especially for $\Phi < 0.6$. This should allow GFP+ diffusion inside the water-(buffer-) phase. But with a volume ratio fraction up to 50%, the surrounding of the protein is crowded. Figure 53 shows the situation for a protein diffusing in the water continuous phase of a microemulsion.

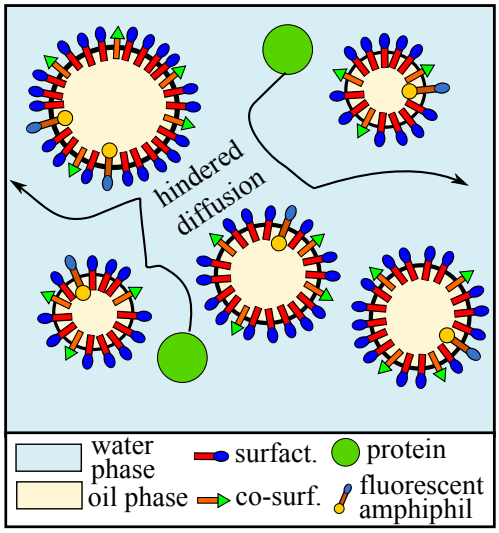

Figure 53: Diffusion model for the $C_{12}G_2$ system, where the structure is not bicontinuous but droplet-like.

The oil droplets in a continuous water phase are polydisperse and bigger than the protein size. At Φ 0.1 the radius is comparable to the GFP+ hydrodynamic radius, the diffusion should be nearly unhindered. For rising Φ the droplets grow and merge with other droplets. The system gets crowded and hampers the diffusion of the protein. To observe the GFP+ dynamics, FCS measurements were performed.

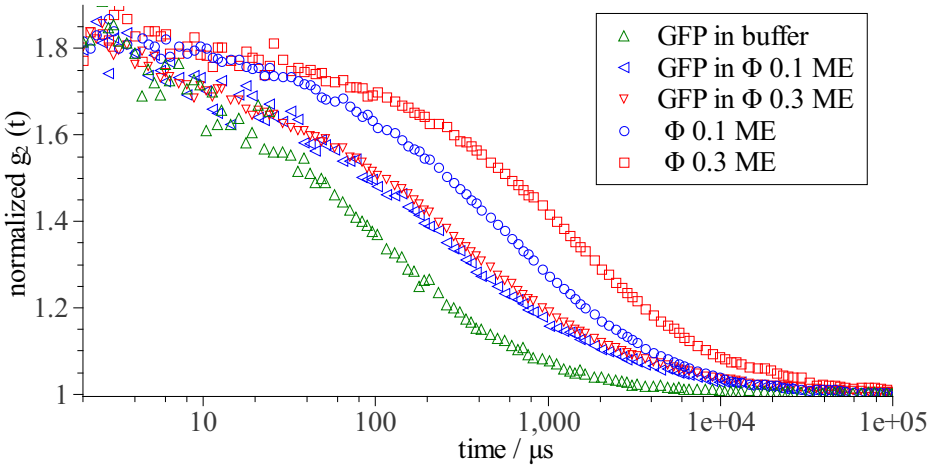

Figure 54: FCS autocorrelation data of GFP+ in a $C_{12}G_2$ microemulsion, compared to GFP+ in buffer and the pure microemulsion dynamics. The curves were normalized for comparison reasons. The microemulsion shows much slower dynamics than GFP+ inside the water domain. Hence, the protein is mobile.

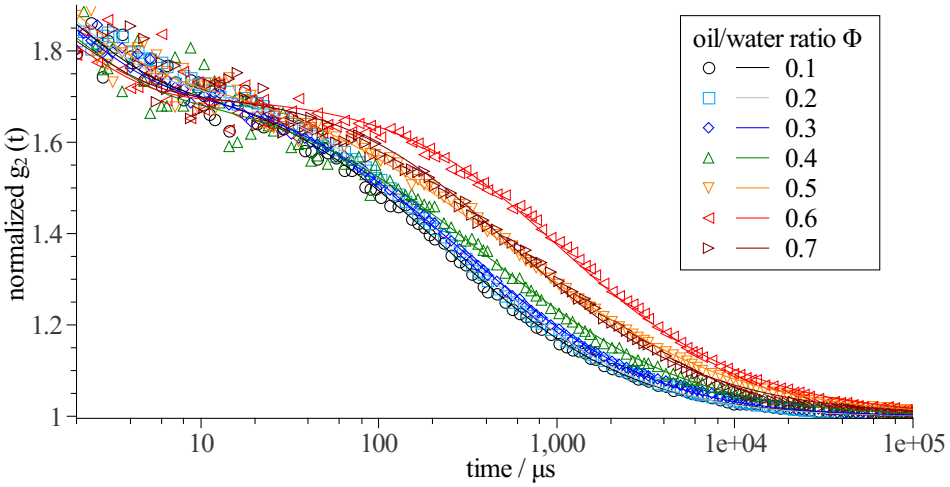

Figure 55: GFP+ FCS autocorrelation curves inside the water domain of the $C_{12}G_2$ microemulsion for different Φ.

As seen in figure 54, the GFP+ measurements show a hindered diffusion for GFP+ inside the microemulsion compared to GFP+ in buffer: The diffusion is hindered by crowding and confinement effects. However, under these conditions the protein moves still significantly faster

compared to the slow collective mode (breathing mode) of the microemulsion.

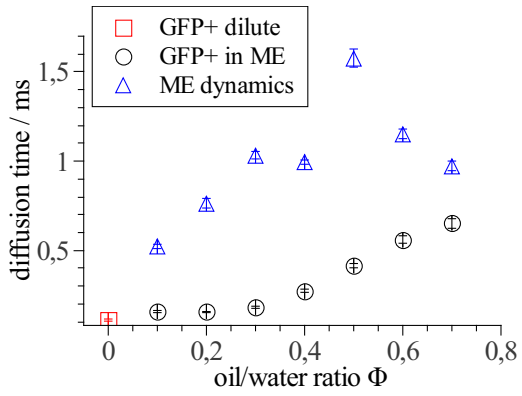

Figure 56: Comparison of the FCS diffusion times in the microemulsion system $C_{12}G_2$ for GFP+ inside the water domain of the microemulsion, GFP+ in buffer and the microemulsion dynamics.

In figure 55 the FCS measurements with samples at different Φ (table 5). In general, the autocorrelation curves move to higher times with increasing Φ. This clearly shows that the dynamic is slowed down. The fit results are summarized in figure 56. For small Φ (0.1 and 0.2), GFP+ shows a good mobility because of small oil droplets in a continuous water phase. These droplets hinder the diffusion of the protein not significantly. For high Φ (0.6 and 0.7), the protein dynamics get similar to the microemulsion dynamics. This clearly shows, that GFP+ is stuck and can only move with the collective breathing motion of the microemulsion structure.

As seen in fig. 57, α is smaller than 1, which indicates subdiffusive behavior. α for the 1-component fit decreases until a minimum at Φ 0.5, the protein gets more and more confined by the shrinking water domains. At Φ 0.6, α increases again, which indicates, that the protein is stuck in the bicontinuous structure leading to the recovery of Fickian diffusion. The breathing motion of the microemulsion structure is a diffusive motion., Hence, α converges to 1.

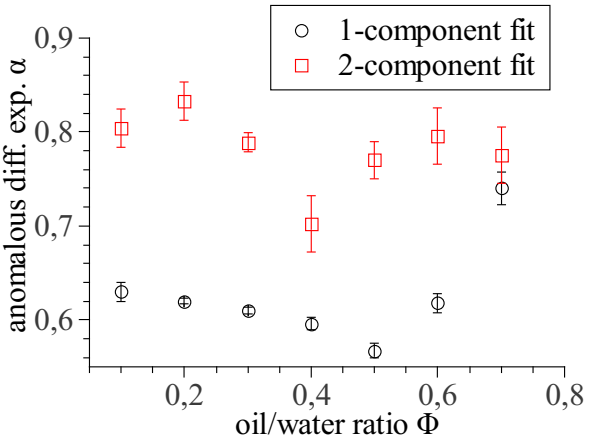

Figure 57: Anomalous diffusion exponent α for GFP+ in the $C_{12}G_2$ system. With an $\alpha < 1$ subdiffusion is observed.

The FCS data can also be approximated with a 2 component model, to regard the microemulsion dynamics, which is measured also, due to the fluorescent impurities, α behaves similar. For small oil/water ratios α is nearly one. This means only minor crowding effects, until $\Phi = 0.4$ it decreases to a minimum. Then α rises again because of the diffusive microemulsion dynamics. But the 2-component fit is not really valid from $\alpha = 0.5$ up to higher values. There the protein is stuck and the diffusion shows only one characteristic time decay.
These anomalous diffusion exponent results are in the same range compared to investigations of proteins in crowded solutions [99], here the authors found α values from 1 to 0.75.

6.3.4 Microemulsion dynamics (FCS)

Knowing that the structure of the $C_{12}G_2$ samples at $\Phi = 0.1 - 0.6$ is droplet-like, more can be extracted from the FCS measurements. The diffusion time obtained from the FCS measurements allows to compute the diffusion coefficient. By using the Stokes-Einstein equation also the hydrodynamic radius of the droplets can be calculated. Figure 58 shows the normalized FCS autocorrelation curves.

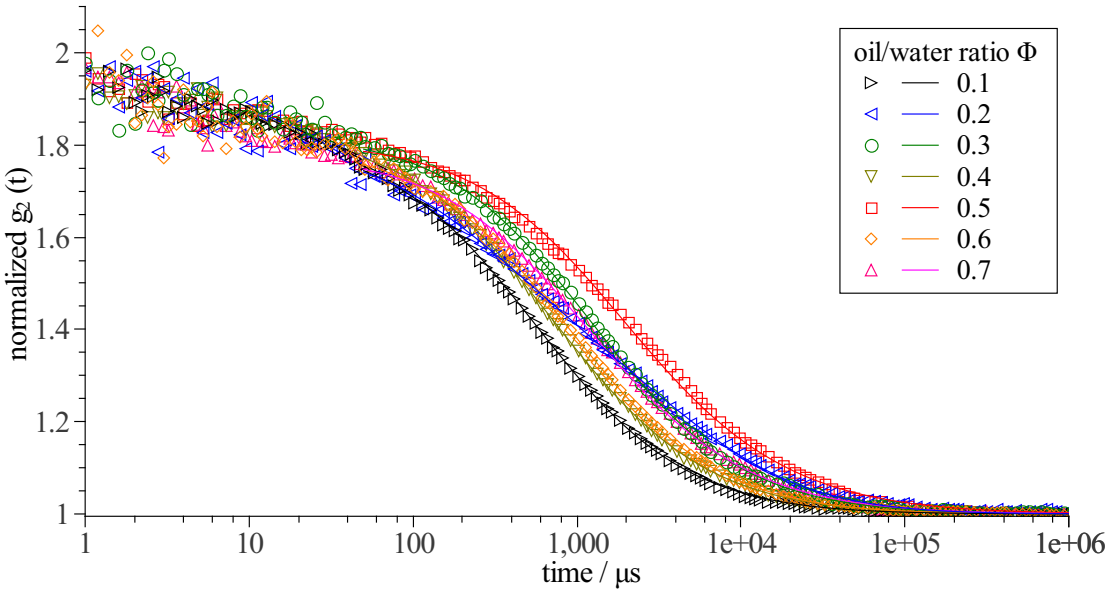

Figure 58: FCS autocorrelation curves of the microemulsion dynamics for different oil/water ratios Φ. The lines represent a 1-component fit.

Because of the high polydispersity of the system the obtained values for the radius of the droplets are only approximated results. The data could also be fitted with a 2- or 3-component model. But for a convincable fit more parameters like polydispersity or the distribution of diffusion times should be known. The results for the hydrodynamic radius compared to values obtained by other methods are plotted in figure 59.

6.3.5 Microemulsion dynamics (DLS)

In the SAS experiments a droplet microemulsion structure was identified. Therefore samples can also be studied by dynamic light scattering. With the resulting apparent diffusion coefficient D_{DLS}, a hydrodynamic radius R_H can be calculated with equation 33. The Stokes-Einstein equation is not fully valid in this case because of polydisperse and interacting spheres. But the hydrodynamic radius can be estimated and therefore it is called *apparent* hydrodynamic radius. The scattering contrast for photons in the visible range is constituted by the refraction index difference in the system. In microemulsions with a bicontinuous or droplet phase, this difference is mainly caused by the oil and water component. Therefore, the obtained diffusion coefficients represent the collective breathing motion of the domains or the movement of oil-in-water or water-in-oil structures, respectively.

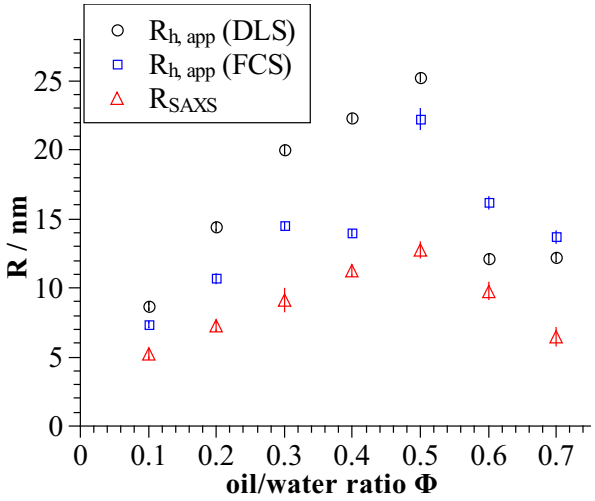

Figure 59: Apparent hydrodynamic DLS and FCS radius and radius of the SAXS measurements determined by the GIFT analysis for the $C_{12}G_2$ microemulsion system at different oil/water ratios Φ. All three methods show an increase of the droplet radius from $\Phi = 0.1$ to 0.5, at 0.6 the radius decreases rapidly to smaller values.

Compared to the SAXS measurements, the DLS results show the same trend. R_h exhibits bigger values because of the crowded droplets which move slower in comparison with a dilute solution. Furthermore, the hydrodynamic radius can not be directly compared to a radius of gyration R_g from the small angle measurements. For hard spheres the ratio R_g/R_h is expected to be 0.778 [100], the results in fig. 59 yield a ratio of approximately 0.6, which is an indication

for spherical droplets. The FCS measurements are in good agreement with the DLS and SAXS results. After $\Phi = 0.5$ there is also a similar drop in the radius.

6.4 Other microemulsion systems

Further work was done aiming at the study of other systems with surfactants having shorter alkyl chain lengths. Namely the surfactants n-hexyl-β-d-glucoside (C_6G_1) and n-heptyl-β-d-glucoside (C_7G_1) were studied using again water, cyclohexane, and 1-pentanol as the other components. It turns out that the phase behavior exhibits no lamellar phase in the γ range, where the systems were scrutinized. The phase diagrams are given in fig. 60. While for C_6G_1 the bicontinuous phase starts at $\gamma = 0.16$, in the C_7G_1 system the X-point is located $\gamma = 0.22$, but less alcohol content is needed to form a single-phase microemulsion. In general, the C_iG_2 microemulsions tend more to form a lamellar phase compared to the C_iG_1 systems.

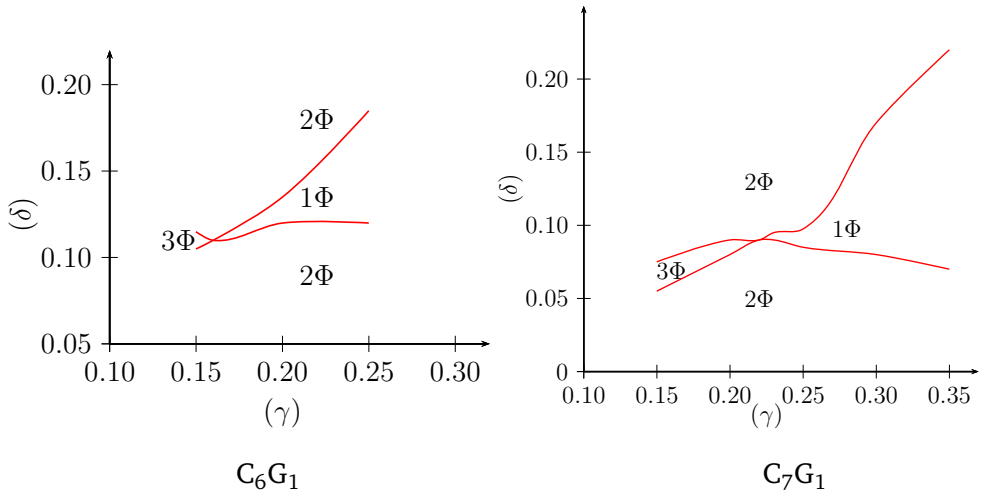

Figure 60: Phase diagrams of C_6G_1 and C_7G_1 microemulsion systems (water, cyclohexane, 1-pentanol), no lamellar phase shows up in the studied γ range.

SANS measurements were carried out for C_7G_1 samples in Saclay/France at the PAXY instrument. Three samples with different γ (0.25, 0.30, 0.35) and constant Φ and δ values were composed. The intensity curves are plotted in fig. 61. The scattering curves exhibit the typical shape obtained for bicontinuous microemulsions. Hence, the Teubner-Strey approximation was applied to obtain length scales.

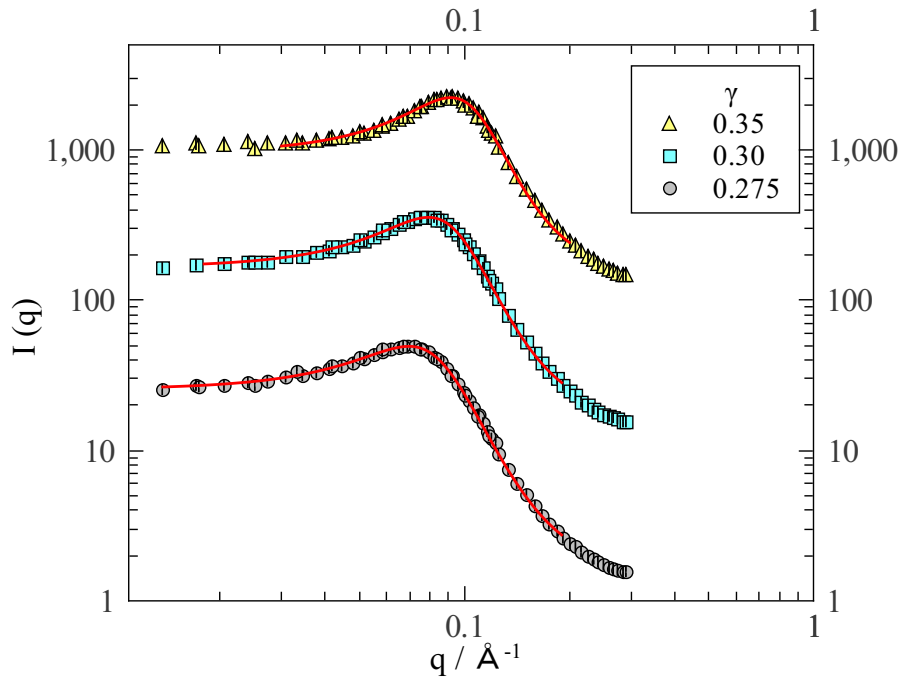

Figure 61: SANS measurements of C_7G_1 microemulsion samples at different γ, Φ 0.5 and δ 0.09. The data was fitted with a Teubner-Strey approximation (equation 43).

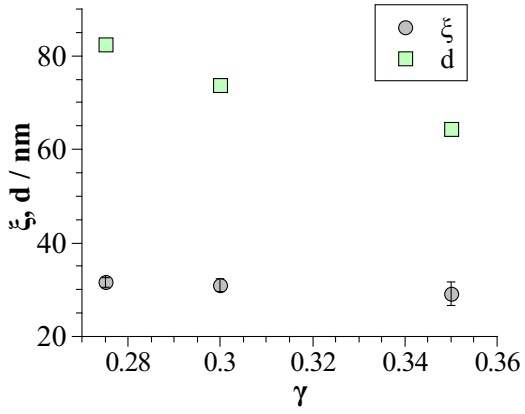

Figure 62: SANS structure sizes derived from the Teubner Strey approximation, ξ: correlation length, d: domain size.

The C_7G_1 based system has a correlation length of 3 nm, the domain size decreases from 8 nm to 6.5 nm for rising γ (compare figure 62). This is due to the rising amount of surfactant in the system which leads to an increase of the interfacial area between water and oil phase, therefore

the water domains shrink. These structure sizes are significantly lower compared to the C_9G_2 and $C_{12}G_2$ system. Thus a diffusion of GFP+ in the water domain is not possible. FCS measurements were accomplished for a $\Phi = 0.1$ and $\gamma = 0.17$ sample, which shows bigger water domains than the length scales measured by SANS. The results are displayed in figure 63.

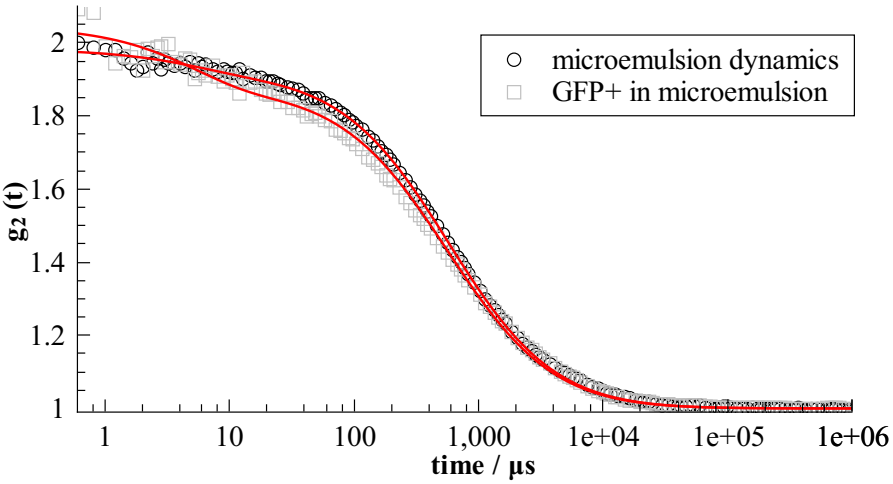

Figure 63: FCS autocorrelation for C_7G_1 microemulsion sample with and without GFP+ at an oil/water ratio of 0.1. The red line indicates a 1-component fit. There is nearly no difference in the timescale.

Even in a $\Phi = 0.1$ microemulsion, no difference in the FCS diffusion time between protein and microemulsion is visible within the experimental error: GFP+ shows a diffusion time of $\tau_{\text{GFP+}} = 565 \pm 5\,\mu\text{s}$, the pure microemulsion dynamics lead to $\tau_{\text{ME}} = 576 \pm 10\,\mu\text{s}$. This implies, that the $\Phi = 0.1$ correlation length is not big enough to allow protein diffusion, which has to be confirmed by SANS measurements.

6.5 Other methods for measuring protein dynamics

Labeling a sample with a fluorescent dye or using a fluorescent molecule is not the only way to follow selectively the dynamic of interest. Neutron spin echo is another option to measure designated dynamics of particles or structures. However, the drawback of this method is its complexity and moreover, the need to have a sample with an appropriate deuteration.
Pulsed-field-gradient nuclear magnetic resonance (PFG-NMR) is another method, but here a high protein concentration, much higher compared to FCS measurements is required.

6.5.1 DFPase NSE measurements

Neutron spin echo is a very sensitive technique to measure dynamics of molecules. In this method the deuteration is the key to highlight the diffusion process of interest. The NSE measurements were performed using the IN15 instrument at the Institute Laue-Langevin in Grenoble/France [68]. Our group already performed NSE measurements [34] with the protein DFPase (used in decontamination applications), where the influence of the protein on the dynamics of the microemulsion was observed. In contrast, here only the diffusion of the protein inside a microemulsion was examined. But the difficulty is, that a fully deuterated microemulsion system is mandatory to fade out the microemulsion structure in the scattering contrast. The initial plan was to use a C_iE_j microemulsion system to get rid of one dynamical component. Additionally, the phase behavior could have been driven by the temperature. But a fully deuterated C_iE_j unfortunately was not available. Therefore, another deuterated surfactant and co-surfactant had to be used. The only commercially available fully deuterated sugar surfactant so far is n-octyl-β-D-glucopyranoside-d17, so the C_8G_1 microemulsion system had to be used with a composition of $\Phi = 0.65$, $\gamma = 0.2$, $\delta = 0.075$.

Diffusion of the protein in dilute solution

By measuring the NSE polarization for different spin-echo times, the data can be plotted logarithmically and fitted linearly. Then the diffusion coefficient can be calculated from the slope for different values of q according to equation 64. The measurements in figure 64 yield a diffusion coefficient of $(6.5 \pm 0.4) \cdot 10^{-11}\,\mathrm{m^2/s}$ and a hydrodynamic radius of $(2.4 \pm 0.2)\,\mathrm{nm}$. This value is in good agreement with the sizes obtained in [34].

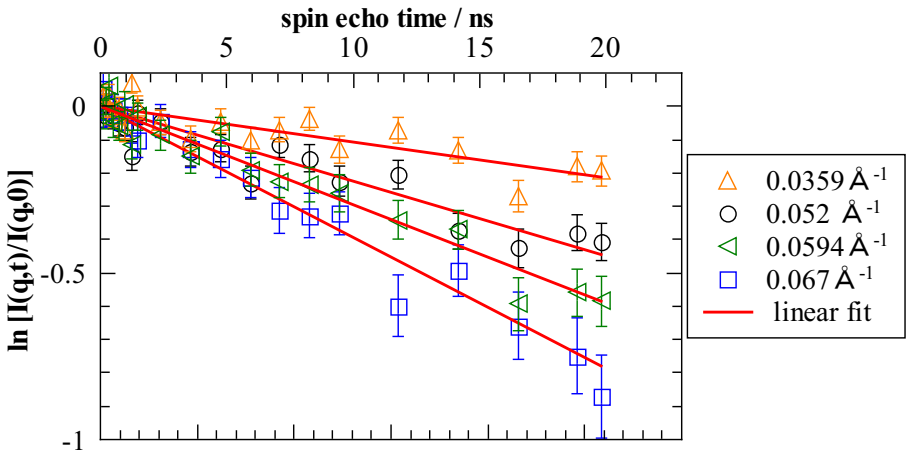

Figure 64: Logarithmic plot of the intermediate scattering function $I(q,t)/I(q,0)$ for DFPase in buffer solution.

Diffusion of the protein inside the microemulsion

To see only the protein diffusion the fully deuterated microemulsion has to be measured with and without the protein. Because of the four microemulsion components, a matching of the scattering contrast is very difficult and requires a high number of samples and therefore a high amount of expensive surfactant. Even in the case of a 3-component microemulsion, with three possible parameters can be varied, the 2D contrast variation is complicated [101]. With one more component a 3D contrast matching is nearly impossible. Thus only the oil and water phase contrast was matched, so the film and protein dynamics are measured. But when a microemulsion without protein is measured, too, it can be used as a background measurement. Hence, two samples were prepared, to minimize the needed amount of surfactant, one with 100 % C_6D_{12}, the other with 100 % C_6H_{12} oil component. By combination of these two samples it was possible to do measurements with four different deuteration ratios. The measured intensity plotted as a function of the volume ratio of C_6H_{12} can be fitted with a parabola to find the contrast matching point.

It turned out, that the matching point is located at nearly 0% (compare figure 65), therefore samples were chosen with 100% C_6D_{12}, to avoid a rising number of components, which is near enough at the matching point. But because of the not perfect contrast variation the dynamics of the film are still visible. Because of that the membrane measurements (microemulsion without

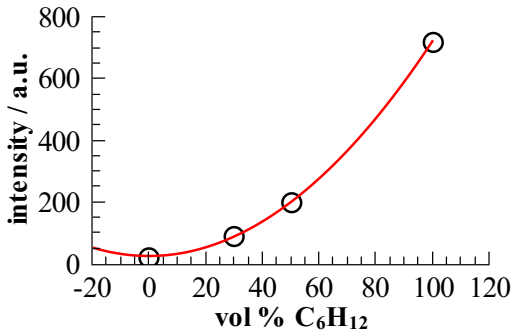

Figure 65: Contrast variation for the spin echo sample with a parabolic fit to find the contrast matching point.

protein) were subtracted from the protein-in-microemulsion measurements. The result is the dynamics of the protein inside the water domain.

The data in fig. 66 was fitted with equation 65. When comparing the subtracted and the membrane measurements, there is nearly no difference between the slopes, only for the $q = 0.052$ Å measurement there is a slight difference. Therefore the protein seems to reflect the dynamics of the microemulsion film. This corresponds to the findings of the FCS experiments for higher Φ. The smaller length scales of the C_8G_1 system are already too small to allow diffusion of the protein inside the water domains. Also in this case the protein (DFPase) is stuck in the microemulsion.

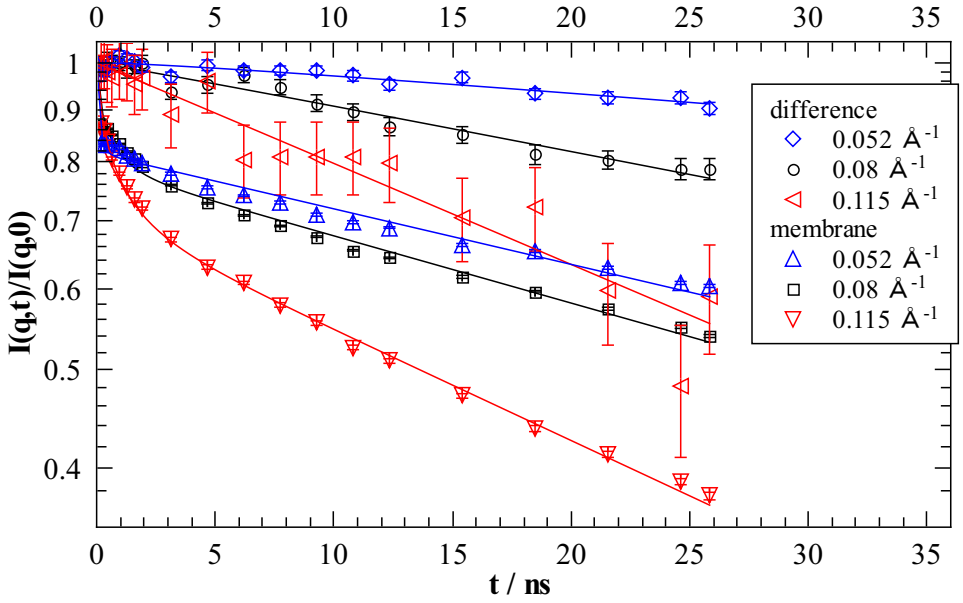

Figure 66: NSE intermediate scattering functions of pure microemulsion samples (film dynamics) and of the difference from the samples with and without protein.

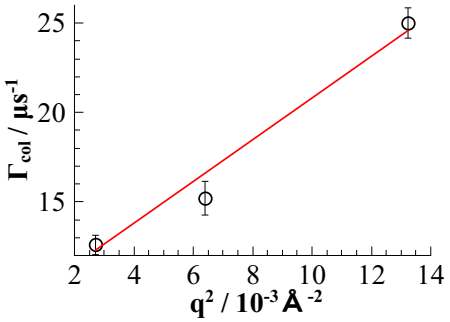

Figure 67: Γ_{col} derived from the approximations of the microemulsion dynamics with equation 65.

From the membrane measurements the dynamics of the film can be extracted. The slope of the calculated Γ_{col} values, figure 65 is the collective diffusion coefficient of the microemulsion: $1.17 \cdot 10^{-11}\,m^2/s$. This result is in the same dimension compared to a Glucopon 220 microemulsion sample used in [34] ($D = 1.75 \cdot 10^{-11}\,m^2/s$). Glucopon 220 ($C_{8\text{-}10}G_{1.3}$) is a technical grade surfactant with chain lengths similar to C_8G_1.

6.5.2 PFG-NMR measurements

Pulsed field gradient NMR is a technique for measuring self diffusion of particles and can also be used to study microemulsion dynamics [102, 103]. PFG is based on a pulsed field gradient spin-echo, instead of a homogeneous magnetic field an inhomogeneous field is used.
The PFG-NMR measurements were performed in collaboration with the group of Cosima Stubenrauch at the Institute for Physical Chemistry (University of Stuttgart).
For the measurements, a high protein concentration and a deuterated solvent are important. Due to that, the protein GFP+ had to be transferred in a deuterated buffer and the concentration was increased to $10\,^{\mathrm{mg}}/_{\mathrm{ml}}$. Compared to the GFP+ FCS-samples, the concentration is 10^4 times higher.
Unfortunately the dynamics of the protein cannot be separated from the dynamics of the microemulsion, although a high protein concentration was used. But even with this big amount of protein only one mode is observed and moreover, this mode is not influenced by the protein concentration and only reflects the microemulsion dynamics.

7 Conclusion and future prospects

Proteins usually do their work in crowded environments inside the cell and the respective organelles. Hence, an understanding of their diffusion is of fundamental importance for the understanding of the processes of life. Moreover, also in technical processes proteins are often used in confined situations. One example is the use of microemulsions as reaction media for decontamination or in chemical production. Hence, observing the diffusion of a protein inside the water domain of a microemulsion is of major importance for improvement of e.g. decontamination applications realized with a protein like DFPase [18, 21, 34]. However, this is not an easy task because the structure of the microemulsion is not much bigger than the particles which shall be traced and the microemulsion matrix gives a kind of "background dynamics" in most of the possible experiments. Therefore methods have to be used, where the structure and respectively the dynamics of the microemulsion is faded out and only the desired particle motion can be followed. Methods like dynamic light scattering are not usable, because the refractive index of the system cannot be changed easily. Thus the method of choice was fluorescence correlation spectroscopy where a fluorescent particle can be traced. However, in this technique other difficulties occurred, and e.g. fluorescent impurities disturb the signal of the particle of interest. Even with components of a high purity $> 99[\%]$ and in 1-pentanol fluorescent impurities were found, in a very low concentration indeed but enough for being detectable by the sensible FCS technique. With technical grade surfactants the fluorescence activity is very high and FCS measurements are not possible. With pure surfactants and a concentration of the fluorescent protein high enough, the detected fluorescent is mainly caused by the protein. Besides the microemulsion dynamics can be taken into account by using a two component model.

With a similar size and therefore comparable hydrodynamic behavior, GFP+ is a suitable model protein to study dynamics with fluorescence correlation spectroscopy. In this thesis the structure of two different sugar surfactant microemulsion systems was studied systematically with small angle x-ray and neutron scattering measurements. It was shown that the dimensions of this microemulsion system allow diffusion of proteins inside the water domain. The FCS results have yielded that GFP+ is mobile depending on the correlation lengths of the water domains. The confinement increases for higher oil volume fraction Φ, meaning smaller water domains. In the present work it could be shown that the diffusion of GFP+ is hindered in the different

microemulsions. This behavior was quantified in terms of the sub-diffusion exponent α and it turns out that α is influenced by the composition of the microemulsion. For smaller water domains α goes down systematically. Hence, microemulsions are well suited as model systems for the study of sub-diffusion in a controlled way. For too high oil/water ratios the protein gets stuck and reflects the dynamics known as the ”collective breathing motion" of the sponge-like structure.

Furthermore, the used system is related to applications. The pure sugar surfactant can be easily replaced by a technical grade surfactant, which leads to cheap microemulsions for commercial use. Studies in the field of skin friendly and environmentally compatible components are already ongoing to provide a system with similar dimensions for wide application possibilities in the decontamination area.

It has to be observed in decontamination experiments which microemulsion systems show the best decontamination ability. In some systems the protein is mobile due to bigger water domains, in other cases at high Φ or with short sugar surfactant systems the protein is stuck in the water phase but near to the oil phase where the toxic agent is located. Thus it has to be observed which influence the protein mobility and the distance to the toxic compound have on the decontamination efficiency and kinetics.

The results related to the sub-diffusion of GFP+ inside the different studies are unique and it remains to be clarified whether the sub-diffusive behavior persists on all length scales or not. Works of Schreiber *et al.* [104] suggest that on very short length scale Fickian diffusion might be recovered. hence, this issue should be addressed using experiments with an appropriate resolution in length. A good choice would be a C_iE_j microemulsion system with a deuterated surfactant in an NSE experiment. Then the phase behavior could be tuned with the temperature. Furthermore, one deuterated component less would be needed and would simplify the contrast matching procedure.

8 Danksagung

In erster Linie bedanke ich mich bei meinem Doktorvater, Prof. Dr. Thomas Hellweg, für die Überlassung des spannenden Themas, das Vertrauen und die vielfältigen Forchungsmöglichkeiten. Großer Dank gilt auch meinen Kollegen Sebastian Höhn, Christoph Angermann, Bastian Wedel, Christoph Schulreich, Michael Zeiser, Katja von Nessen, Susanne Seibt, Yvonne Hertle, Simone Wagner und Ralf Stehle für interessante Diskussionen, diverse Ratschläge, jegliche Unterstützung und die sehr gute Zusammenarbeit.
Herrn Prof. Dr. Stephan Förster danke ich dafür, dass ich meine Arbeit in Bayreuth fertigstellen durfte. Allen "neuen" Kollegen aus der Arbeitsgruppe Förster, insbesondere meinen Bürokameraden Sebastian With und Jan Schröder danke ich für die positive Atmosphäre und die sehr gute Zusammenarbeit. Einen besonderen Dank auch an Karlheinz Lauterbach, der immer ein offenes Ohr hatte und sich unablässig um die einwandfreie Funktion der Lehrstuhlaustattung kümmerte.
Mein Dank gilt auch Herrn Prof. Dr. Matthias Weiss und den Mitarbeitern aus der Experimentalphysik I, für die gute Zusammenarbeit und Möglichkeit der Nutzung des Confocor 2 auch nach dem Umzug des Gerätes.
Vielen Dank an Uwe Güth für Herstellung und Lieferung der Proteinlösungen. Bei Martin Dulle möchte ich mich für die Unterstützung bei den SAXS-Messungen, Mireia Subinyà für die PFG-NMR Messungen und Frank Lüdel für SANS-Messungen bedanken .
Elisabeth Düngfelder und Sandra Gericke will ich für die Hilfe bei allen Themen außerhalb der Forschung bedanken.
Beim wehrwissenschaftlichen Institut Munster möchte ich mich für die Finanzierung des Projektes bedanken. Vielen Dank den Local Contacts Alain Lapp in Saclay/LLB und Peter Falus in Grenoble/ILL für die Untersützung während der Messzeiten.

Von ganzen Herzen möchte ich mich auch bei meiner Familie und bei meiner Freundin Maria bedanken für die Geduld, das Verständnis und dass sie immer an mich geglaubt haben. Meinen Eltern ein herzlicher Dank für die Unterstützung und dass sie mir das Studium überhaupt ermöglicht haben.

A Appendix

A.1 Alternative microemulsion systems

Due to the problem that 1-pentanol and similar alcohols with other chain lengths contain fluorescent impurities which may disturb FCS measurements, it was searched for alternative fluorescent free co-surfactant. One candidate is 1-propanol, this alcohol is available in high purity and shows nearly no fluorescence activity.
Using the components n-dodecyl-β-d-maltoside, cyclohexane and water, the formation of a microemulsion is possible. But the main problem is the high amount of 1-propanol which is needed to reach the 1-phase region, the X-point is located at $\gamma = 0.1$, $\delta = 0.39$.

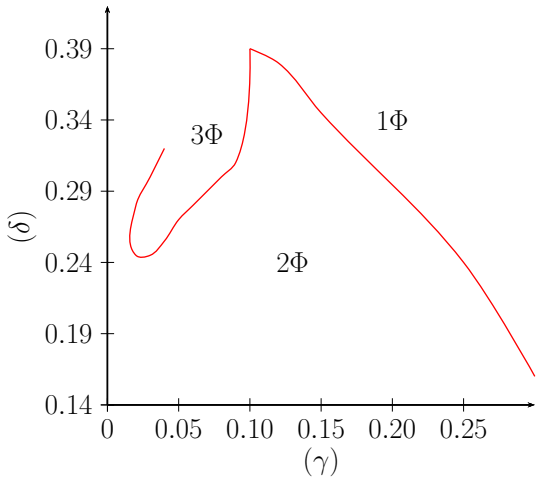

Figure 68: Phase diagram of the system $C_{12}G_2$-propanol-cyclohexane-water, the 1-phase borders are located at high alcohol amounts.

The upper borders of the 1-phase area could not be determined. At such high δ values, there is more propanol present in the system than water and oil, therefore it is uncertain, what kind of structure is obtained. Another possible explanation for the fact that no upper phase boundary could be formed would be refractive index matching with two phases, then the phases cannot be separated by visible inspection. Two get more information about the structure, SANS measurements were performed at the ILL in Grenoble/France, figure 69. The samples were made at constant δ with varying γ starting close to the X-point for a constant oil/water ratio.

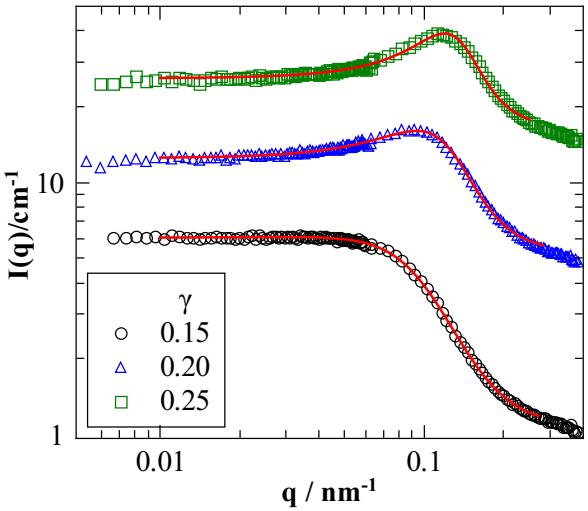

Figure 69: $C_{12}G_2$-propanol microemulsion SANS measurements for different γ values at Φ 0.5 and δ 0.38. The red lines are fits according to the Teubner-Strey approximation.

The scattering curves show structure peaks for higher γ values moving to higher q for rising γ meaning decreasing structure sizes. This is common for bicontinuous microemulsion systems, because with increasing surfactant amount more molecules stay at the interface and are able to form smaller water/oil domains. The SANS data can be fitted with the Teubner-Strey approximation, the results are shown in table 7.

Table 7: Structure sizes for $C_{12}G_2$-propanol-microemulsions determined by SANS at Φ 0.5 and δ 0.38

γ	ξ / nm	d / nm
0.15	2.1	4.9
0.2	1.8	5.8
0.25	1.4	4.6

The structures are very small compared to other systems and at least for $\gamma = 0.15$ it has to be clarified, if the structure is really bicontinuous or droplet-like and where the 1-propanol molecules are located, which are the major component in the system.

A.2 Solvent sensitive fluorescent dyes

Fluorescent dyes can be influenced by the solvent, the consequence is for example a quenched fluorescence or a shift in the emission spectra. nile-red [105,106] is a lipophilic molecule which is sensitive to the polarity of the used solvent. Figure 70 shows fluorescence emission of nile-red in cyclohexane and 1-pentanol.

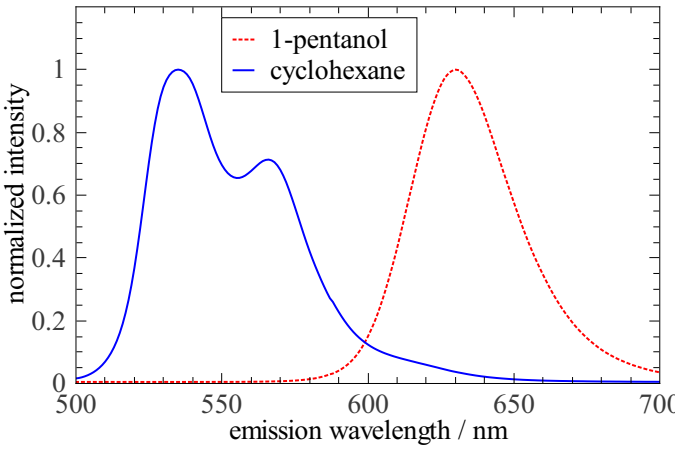

Figure 70: Fluorescence of nile-red in different solvents, cyclohexane and 1-pentanol.

In water, where nile-red is nearly not soluble, the emission maximum is located at 660 nm [105]. The emission maximum is at 535 nm for the unpolar solvent cyclohexane and at 630 nm for 1-pentanol. This is a big solvochromic shift of 95 nm. Nile-red can also be dissolved in a microemulsion, which is plotted in figures 71 (δ variation), 72 (Φ variation) and 73 (γ variation). The influence of a rising content of pentanol in the δ variation shifts the maximum to higher wavelengths.

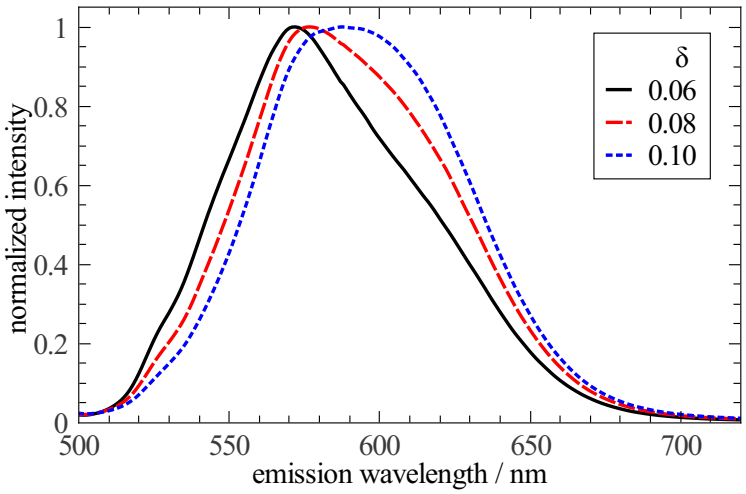

Figure 71: Nile-red fluorescence in microemulsions with different δ ((components: water, Glucopon 220, cyclohexane, 1-pentanol).

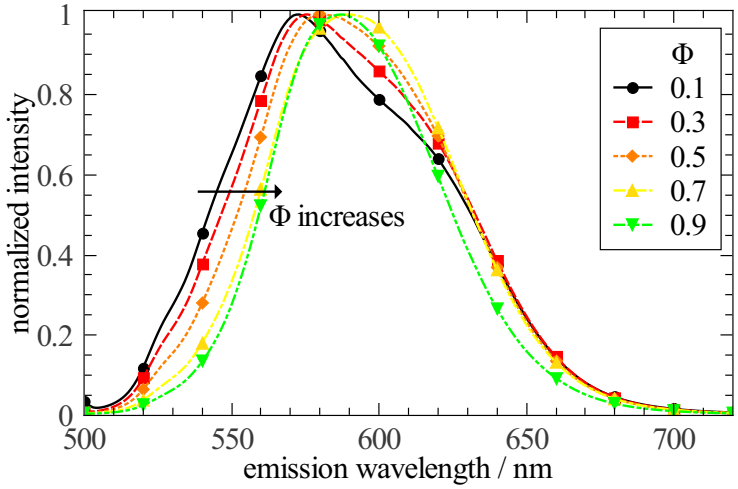

Figure 72: Nile-red fluorescence in microemulsion with different Φ (components: water, Glucopon 220, cyclohexane, 1-pentanol).

When Φ is varied, the emission maximum should increase with shrinking Φ due to the increasing water amount. But this is not the case, with rising Φ the maximum moves to higher wavelength. Most likely, the necessary higher amount of 1-pentanol influences the nile-red emission in the microemulsion. This is an indication, that the pentanol molecules are located in the surfactant interface and diluted in the cyclohexane phase. Therefore, nile-red could be used as a marker

for the distribution of 1-pentanol.

A change of the surfactant content γ hardly affects the emission wavelength, only in a range of 3 nm. For increasing γ, the microemulsion structure morphs from a bicontinuous phase to a droplet structure. Further γ increasing results in smaller droplets. Thus nile-red is located in the oil domains or droplets, where it is serperated from the water phase by the surfactant interface. Also the distribution of pentanol is not changing when γ is increased.

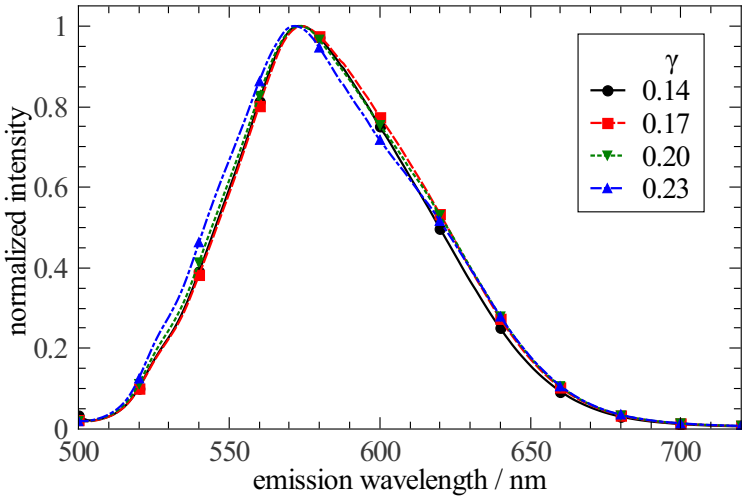

Figure 73: Nile-red fluorescence in microemulsion with different γ (components: water, Glucopon 220, cyclohexane, 1-pentanol).

List of Figures

List of Tables

References

[1] P. Winsor, "Hydrotropy, solubilisation and related emulsification processes," *Transactions of the Faraday Society*, vol. 44, pp. 376–398, 1948.

[2] J. Schulman, W. Stoeckenius, and L. Prince, "Mechanism of formation and structure of micro emulsions by electron microscopy," *The Journal of Physical Chemistry*, vol. 63, no. 10, pp. 1677–1680, 1959.

[3] T. Hoar and J. Schulman, "Transparent Water-in-Oil Dispersions: the Oleopathic Hydro-Micelle," *Nature*, vol. 152, pp. 102–103, 1943.

[4] S. Friberg, *Micellization, solubilization, and microemulsions (Mittal, K.L. and American Chemical Society)*. Micellization, Solubilization, and Microemulsions, Band 1, Plenum Press, 1977.

[5] S. Friberg, *Microemulsions: Theory and practice (Prince, L.M.)*. Academic Press, 1977.

[6] G. Gillberg, H. Lehtinen, and S. Friberg, "NMR and IR investigation of the conditions determining the stability of microemulsions," *Journal of Colloid and Interface Science*, vol. 33, no. 1, pp. 40 – 53, 1970.

[7] K. Shinoda and T. Ogawa, "The solubilization of water in nonaqueous solutions of nonionic surfactants," *Journal of Colloid and Interface Science*, vol. 24, no. 1, pp. 56 – 60, 1967.

[8] K. Shinoda and H. Saito, "The effect of temperature on the phase equilibria and the types of dispersions of the ternary system composed of water, cyclohexane, and nonionic surfactant," *Journal of Colloid and Interface Science*, vol. 26, no. 1, pp. 70 – 74, 1968.

[9] K. Shinoda and H. Saito, "The stability of o/w type emulsions as functions of temperature and the HLB of emulsifiers: The emulsification by PIT-method," *Journal of Colloid and Interface Science*, vol. 30, no. 2, pp. 258 – 263, 1969.

[10] D. Shah, *Surface phenomena in enhanced oil recovery*. Plenum Press, 1981.

[11] C. Solans and H. Kunieda, *Industrial Applications of Microemulsions*. Surfactant Science Series, M. Dekker, 1997.

[12] M.-J. Schwuger, K. Stickdorn, and R. Schomaecker, "Microemulsions in technical processes," *Chemical Reviews*, vol. 95, no. 4, pp. 849–864, 1995.

[13] R. Schomäcker and Bayer-AG, "Mikroemulsionen als Medium für chemische Reaktionen," *Nachrichten aus Chemie, Technik und Laboratorium*, vol. 40, no. 12, pp. 1344–1352, 1992.

[14] M. Pileni, "Reverse micelles as microreactors," *The Journal of Physical Chemistry*, vol. 97, no. 27, pp. 6961–6973, 1993.

[15] J. Sjöblom, R. Lindberg, and S. E. Friberg, "Microemulsions - phase equilibria characterization, structures, applications and chemical reactions," *Advances in Colloid and Interface Science*, vol. 65, no. 0, pp. 125 – 287, 1996.

[16] M. Höfer, "Chemische Kampfstoffe: Ein Überblick," *Chemie in unserer Zeit*, vol. 36, no. 3, pp. 148–155, 2002.

[17] H. Murakami, A. Birnbaum, and P. Gabriel, *Underground*. Vintage International, 2001.

[18] M.-M. Blum and A. Richardt, *Decontamination of Warfare Agents: Enzymatic Methods for the Removal of B/C Weapons*. Wiley-VCH Verlag GmbH & Co. KGaA, 2008.

[19] M. Kahlweit, G. Busse, B. Faulhaber, and H. Eibl, "Preparing nontoxic microemulsions," *Langmuir*, vol. 11, no. 11, pp. 4185–4187, 1995.

[20] S. Wellert, H. Altmann, A. Richardt, A. Lapp, P. Falus, B. Farago, and T. Hellweg, "Dynamics of the interfacial film in bicontinuous microemulsions based on a partly ionic surfactant mixture: A neutron spin-echo study," *The European Physical Journal E: Soft Matter and Biological Physics*, vol. 33, pp. 243–250, 2010. 10.1140/epje/i2010-10668-1.

[21] A. Richardt, M.-M. Blum, and S. Mitchell, "Was wissen Calamari über Sarin? Enzymatische Dekontamination von Nervenkampfstoffen," *Chemie in unserer Zeit*, vol. 40, no. 4, pp. 252–259, 2006.

[22] C. Stubenrauch, *Microemulsions: Background, New Concepts, Applications, Perspectives*. Oxford: WILEY-VCH Verlag, 2009.

[23] W. Pritzkow, "Die Tenside, Herausgegeben von K. Kosswig und H. Stache München," *Journal für Praktische Chemie/Chemiker-Zeitung*, vol. 336, no. 5, pp. 473–473, 1994.

[24] H. Roth and H. Fenner, *Arzneistoffe*. Stuttgart: Thieme, 1998.

[25] *Brockhaus ABC Chemie*. VEB F. A. Brockhaus Verlag Leipzig, 1965.

[26] K. Kosswig and H. Stache, *Die Tenside*. Hanser, 1993.

[27] T. Hellweg, "Phase structures of microemulsions," *Current Opinion in Colloid and Interface Science*, vol. 7, no. 1 - 2, pp. 50 – 56, 2002.

[28] A. Biasio, C. Cametti, P. Codastefano, P. Tartaglia, J. Rouch, and S. Chen, "Phase behavior of dense three-component ionic microemulsions and electrical conductivity in the lamellar phase," *Physical Review E*, vol. 47, pp. 4258–4264, Jun 1993.

[29] A. Biasio, C. Cametti, P. Codastefano, P. Tartaglia, J. Rouch, and S. Chen, "Electrical conductivity in the lamellar phase of a water-in-oil microemulsion," in *Trends in Colloid and Interface Science VII*, vol. 93 of *Progress in Colloid & Polymer Science*, pp. 191–193, Steinkopff, 1993.

[30] S. Burauer, L. Belkoura, C. Stubenrauch, and R. Strey, "Bicontinuous microemulsions revisited: a new approach to freeze fracture electron microscopy (FFEM)," *Colloids and Surfaces A: Physicochemical and Engineering Aspects*, vol. 228, no. 1-3, pp. 159 – 170, 2003. Festschrift for Professor Bjorn Lindman.

[31] N. Freiberger, C. Moitzi, L. de Campo, and O. Glatter, "An attempt to detect bicontinuity from sans data," *Journal of Colloid and Interface Science*, vol. 312, no. 1, pp. 59 – 67, 2007.

[32] M. Kahlweit, G. Busse, and J. Winkler, "Electric conductivity in microemulsions," *The Journal of Chemical Physics*, vol. 99, no. 7, pp. 5605–5614, 1993.

[33] A. Zilman and R. Granek, "Undulations and dynamic structure factor of membranes," *Physical Review Letters*, vol. 77, pp. 4788–4791, Dec 1996.

[34] S. Wellert, B. Tiersch, J. Koetz, A. Richardt, A. Lapp, O. Holderer, J. Gäb, M.-M. Blum, C. Schulreich, R. Stehle, and T. Hellweg, "The DFPase from loligo vulgaris in sugar surfactant-based bicontinuous microemulsions: Structure, dynamics, and enzyme activity," *European Biophysics Journal*, vol. 40, pp. 761–774, 2011.

[35] R. Strey, "Microemulsion microstructure and interfacial curvature," *Colloid and Polymer Science*, vol. 272, pp. 1005–1019, 1994.

[36] M. Teubner and R. Strey, "Origin of the scattering peak in microemulsions," *The Journal of Chemical Physics*, vol. 87, pp. 3195–3200, 1987.

[37] S. Wellert, M. Karg, H. Imhof, A. Steppin, H.-J. Altmann, M. Dolle, A. Richardt, B. Tiersch, J. Koetz, A. Lapp, and T. Hellweg, "Structure of biodiesel based bicontinuous microemulsions for environmentally compatible decontamination: A small angle neutron scattering and freeze fracture electron microscopy study," *Journal of Colloid and Interface Science*, vol. 325, no. 1, pp. 250 – 258, 2008.

[38] T. Sottmann, "Solubilization efficiency boosting by amphiphilic block co-polymers in microemulsions," *Current Opinion in Colloid and Interface Science*, vol. 7, no. 1, pp. 57–65, 2002.

[39] B. Jakobs, T. Sottmann, R. Strey, J. Allgaier, , and D. Richter, "Amphiphilic block copolymers as efficiency boosters for microemulsions," *Langmuir*, vol. 15, no. 20, pp. 6707–6711, 1999.

[40] H. Endo, J. Allgaier, M. Mihailescu, M. Monkenbusch, G. Gompper, D. Richter, B. Jakobs, T. Sottmann, and R. Strey, "Amphiphilic block copolymers as efficiency boosters in microemulsions: a SANS investigation of the role of polymers," *Applied Physics A*, vol. 74, pp. 392–395, 2002.

[41] S. Wellert, H. Imhof, M. Dolle, H.-J. Altmann, A. Richardt, and T. Hellweg, "Decontamination of chemical warfare agents using perchloroethylene - marlowet IHF-H_2O-based microemulsions: wetting and extraction properties on realistic surfaces," *Colloid & Polymer Science*, vol. 286, pp. 417–426, 2008.

[42] E. Scharff, J. Koepke, G. Fritzsch, C. Luecke, and H. Rueterjans, "RCSB protein data bank: 1E1A, crystal structure of diisopropylfluorophosphatase from Loligo vulgaris." http://www.rcsb.org/pdb/explore/explore.do?structureId=1E1A. (01/2013).

[43] E. Scharff, J. Koepke, G. Fritzsch, C. Lücke, and H. Rüterjans, "Crystal structure of diisopropylfluorophosphatase from loligo vulgaris.," *Structure*, vol. 9, no. 6, pp. 493–502, 2001.

[44] C. Schulreich, C. Angermann, S. Hoehn, R. Neubauer, S. Seibt, R. Stehle, A. Lapp, A. Richardt, A. Diekmann, and T. Hellweg, "Bicontinuous microemulsions with extremely high temperature stability based on skin friendly oil and sugar surfactant," *Colloids and Surfaces A: Physicochemical and Engineering Aspects*, vol. 418, pp. 39–46, 2013.

[45] S. Wellert, M. Karg, O. Holderer, A. Richardt, and T. Hellweg, "Temperature dependence of the surfactant film bending elasticity in a bicontinuous sugar surfactant based microemulsion: A quasielastic scattering study," *Phys. Chem. Chem. Phys.*, vol. 13, pp. 3092–3099, 2011.

[46] E. Elson and D. Magde, "Fluorescence correlation spectroscopy. I. Conceptual basis and theory," *Biopolymers*, vol. 13, no. 1, pp. 1–27, 1974.

[47] J. Lakowicz, *Principles of Fluorescence Spectroscopy*. Springer London, 2009.

[48] P. Pringsheim, *Fluorescence and phosphorescence*. Interscience Publishers New York and London, 1963.

[49] R. Kellogg and R. Bennett, "Radiationless Intermolecular Energy Transfer. III. Determination of Phosphorescence Efficiencies," *The Journal of Chemical Physics*, vol. 41, no. 10, pp. 3042–3045, 1964.

[50] A. Follenius-Wund, M. Bourotte, M. Schmitt, F. Iyice, H. Lami, J.-J. Bourguignon, J. Haiech, and C. Pigault, "Fluorescent derivatives of the GFP chromophore give a new insight into the GFP fluorescence process," *Biophysical Journal*, vol. 85, no. 3, pp. 1839 – 1850, 2003.

[51] R. Rigler and E. Elson, *Fluorescence Correlation Spectroscopy: Theory and Applications*. Berlin: Springer, 2001.

[52] S. Keller, *Fluoreszenz-Korrelations-Spektroskopie in Polymerlösungen*. PhD thesis, München, 2004.

[53] J. Ricka and T. Binkert, "Direct measurement of a distinct correlation function by fluorescence cross correlation," *Physical Review A*, vol. 39, pp. 2646–2652, Mar 1989.

[54] J. Widengren and R. Rigler, "Mechanisms of photobleaching investigated by fluorescence correlation spectroscopy," *Bioimaging*, vol. 4, no. 3, pp. 149–157, 1996.

[55] J. Widengren, U. Mets, and R. Rigler, "Fluorescence correlation spectroscopy of triplet states in solution: A theoretical and experimental study," *The Journal of Physical Chemistry*, vol. 99, no. 36, pp. 13368–13379, 1995.

[56] M. Weiss, M. Elsner, F. Kartberg, and T. Nilsson, "Anomalous subdiffusion is a measure for cytoplasmic crowding in living cells.," *Biophys. J.*, vol. 87, pp. 3518–3524, Nov. 2004.

[57] S. Provencher, "Inverse problems in polymer characterization: Direct analysis of polydispersity with photon correlation spectroscopy," *Die Makromolekulare Chemie*, vol. 180, no. 1, pp. 201–209, 1979.

[58] D. Koppel, "Analysis of macromolecular polydispersity in intensity correlation spectroscopy: The method of cumulants," *The Journal of Chemical Physics*, vol. 57, no. 11, pp. 4814–4820, 1972.

[59] S. Provencher, "A constrained regularization method for inverting data represented by linear algebraic or integral equations," *Computer Physics Communications*, vol. 27, no. 3, pp. 213 – 227, 1982.

[60] S. Provencher, "CONTIN: A general purpose constrained regularization program for inverting noisy linear algebraic and integral equations," *Computer Physics Communications*, vol. 27, no. 3, pp. 229–242, 1982.

[61] A. G. Langen/Germany, "ALV-5000 DLS instrument." http://www.alvgmbh.de. (11/2012).

[62] U. Tübingen, "Small-angle scattering and data analysis." http://www.soft-matter.uni-tuebingen.de/teaching/SASTutorial.pdf. (12/2012).

[63] J. Kohlbrecher and I. Bressler, "SASfit." https://kur.web.psi.ch/sans1/SANSSoft/sasfit.html. (01/2013).

[64] O. Glatter, "GIFT: small angle scattering data evaluation software." http://physchem.kfunigraz.ac.at/sm/Index.html. (01/2013).

[65] A. Bergmann, G. Fritz, and O. Glatter, "Solving the generalized indirect Fourier transformation (GIFT) by Boltzmann simplex simulated annealing (BSSA)," *Journal of Applied Crystallography*, vol. 33, pp. 1212–1216, Oct 2000.

[66] F. Mezei, C. Pappas, and T. Gutberlet, *Neutron Spin Echo Spectroscopy: Basics, Trends and Applications*. Lecture Notes in Physics, Springer, 2003.

[67] T. Munich, "RESEDA-Handout." http://www2009.ph.tum.de/studium/betrieb/praktika/fopra/versuche/61/. (12/2012).

[68] "Institut Laue-Langevin, Grenoble, France - IN15." http://www.ill.eu/html/instruments-support/instruments-groups/instruments/in15/. (12/2012).

[69] C. Bargeron, "Measurement of a continuous distribution of spherical particles by intensity correlation spectroscopy: Analysis by cumulants," *The Journal of Chemical Physics*, vol. 61, no. 5, pp. 2134–2138, 1974.

[70] T. Hellweg, M. Gradzielski, B. Farago, and D. Langevin, "Shape fluctuations of microemulsion droplets: A neutron spin-echo study," *Colloids and Surfaces A: Physicochemical and Engineering Aspects*, vol. 183-185, no. 0, pp. 159 – 169, 2001.

[71] S. Milner and S. Safran, "Dynamical fluctuations of droplet microemulsions and vesicles," *Physical Review A*, vol. 36, pp. 4371–4379, Nov 1987.

[72] J. Huang, S. Milner, B. Farago, and D. Richter, "Study of dynamics of microemulsion droplets by neutron spin-echo spectroscopy," *Physical Review Letters*, vol. 59, pp. 2600–2603, Nov 1987.

[73] T. Hellweg and D. Langevin, "The dynamics in dodecane/$C_{10}E_5$/water microemulsions determined by time resolved scattering techniques," *Physica A: Statistical Mechanics and its Applications*, vol. 264, no. 3-4, pp. 370 – 387, 1999.

[74] C. Schulreich, "Bikontinuierliche Mikroemulsionen als neuartige Dekontaminationsmittel: Phasenverhalten und Strukturuntersuchungen in Zuckertensid - Systemen (Zulassungsarbeit)," Bayreuth 2009.

[75] R. Wheeler, "RCSB protein data bank: 1EMA, GFP structure." www.wikipedia.org. (11/2012).

[76] X. Shu, N. Shaner, C. Yarbrough, R. Tsien, and S. Remington, "RCSB protein data bank: 2H5Q, crystal structure of mCherry." http://www.rcsb.org/pdb/explore/explore.do?structureId=2H5Q. (11/2012).

[77] O. Shimomura, F. H. Johnson, and Y. Saiga, "Extraction, purification and properties of aequorin, a bioluminescent protein from the luminous hydromedusan, aequorea," *Journal of Cellular and Comparative Physiology*, vol. 59, no. 3, pp. 223–239, 1962.

[78] O. Scholz, A. Thiel, W. Hillen, and M. Niederweis, "Quantitative analysis of gene expression with an improved green fluorescent protein," *European Journal of Biochemistry*, vol. 267, no. 6, pp. 1565–1570, 2000.

[79] M. Chalfie and S. Kain, *Methods of Biochemical Analysis, Green Fluorescent Protein: Properties, Applications and Protocols*. Methods of Biochemical Analysis, Wiley, 2005.

[80] S. Bokman and W. Ward, "Renaturation of aequorea green-fluorescent protein," *Biochemical and Biophysical Research Communications*, vol. 101, no. 4, pp. 1372 – 1380, 1981.

[81] N. Shaner, R. Campbell, P. Steinbach, B. Giepmans, A. Palmer, and R. Tsien, "Improved monomeric red, orange and yellow fluorescent proteins derived from Discosoma sp. red fluorescent protein," *Nature Biotechnology*, vol. 22, pp. 1567–1572, Dec. 2004.

[82] H. Zettl, *New Applications of Fluorescence Correlation Spectroscopy in Materials Science*. PhD thesis, Bayreuth, 2006.

[83] H. Bagger-Jörgensen, L. Coppola, K. Thuresson, U. Olsson, and K. Mortensen, "Phase behavior, microstructure, and dynamics in a nonionic microemulsion on addition of hydrophobically end-capped poly(ethylene oxide)," *Langmuir*, vol. 13, no. 16, pp. 4204–4218, 1997.

[84] J. Huang, J. Sung, and X.-L. Wu, "The effect of H_2O and D_2O on a water-in-oil microemulsion," *Journal of Colloid and Interface Science*, vol. 132, no. 1, pp. 34 – 42, 1989.

[85] I. Vasilief, "Qtiplot." http://soft.proindependent.com/qtiplot.html. (10/2012).

[86] J. Nelder and R. Mead, "A simplex method for function minimization," *The Computer Journal*, vol. 7, no. 4, pp. 308–313, 1965.

[87] "Ganesha - Small Angle X-Ray Scattering instrument." SAXS LAB / Denmark.

[88] "PAXY instrument at the LLB Saclay/France." http://www-llb.cea.fr/en/fr-en/pdf/paxy-llb.pdf. (11.2012).

[89] G. Burnett, G. Rees, D. Steytler, and B. Robinson, "Fluorescence correlation spectroscopy of water-in-oil microemulsions: An application in specific characterisation of droplets containing biomolecules," *Colloids and Surfaces A: Physicochemical and Engineering Aspects*, vol. 250, no. 1-3, pp. 171 – 178, 2004.

[90] M. Gradzielski, "Recent developments in the characterisation of microemulsions," *Current Opinion in Colloid & Interface Science*, vol. 13, no. 4, pp. 263 – 269, 2008.

[91] E. Potma, W. de Boeij, L. Bosgraaf, J. Roelofs, P. van Haastert, and D. Wiersma, "Reduced protein diffusion rate by cytoskeleton in vegetative and polarized dictyostelium cells," *Biophysical Journal*, vol. 81, no. 4, pp. 2010 – 2019, 2001.

[92] S. Sun, *Physical Chemistry of Macromolecules: Basic Principles and Issues*. Wiley New Jersey, 2004.

[93] T. Sottmann and R. Strey, "Evidence of corresponding states in ternary microemulsions of water - alkane - C_iE_j," *Journal of Physics: Condensed Matter*, vol. 8, no. 25A, p. A39, 1996.

[94] M. Summers, J. Eastoe, S. Davis, Z. Du, R. M. Richardson, R. K. Heenan, D. Steytler, and I. Grillo, "Polymerization of cationic surfactant phases," *Langmuir*, vol. 17, no. 17, pp. 5388–5397, 2001.

[95] N. Malchus and M. Weiss, "Elucidating anomalous protein diffusion in living cells with fluorescence correlation spectroscopy-facts and pitfalls," *Journal of Fluorescence*, vol. 20, pp. 19–26, 2010. 10.1007/s10895-009-0517-4.

[96] T. Hellweg and R. von Klitzing, "Evidence for polymer-like structures in the single phase region of a dodecane/$C_{12}E_5$/water microemulsion: a dynamic light scattering study," *Physica A: Statistical Mechanics and its Applications*, vol. 283, no. 3-4, pp. 349 – 358, 2000.

[97] T. Hellweg and W. Eimer, "The micro-structures formed by Ni^{2+}-AOT/cyclohexane/water microemulsions: a light scattering study," *Colloids and Surfaces A: Physicochemical and Engineering Aspects*, vol. 136, no. 1-2, pp. 97 – 107, 1998.

[98] M. Gradzielski, D. Langevin, and B. Farago, "Experimental investigation of the structure of nonionic microemulsions and their relation to the bending elasticity of the amphiphilic film," *Phys. Rev. E*, vol. 53, pp. 3900–3919, Apr 1996.

[99] D. Banks and C. Fradin, "Anomalous diffusion of proteins due to molecular crowding," *Biophysical Journal*, vol. 89, no. 5, pp. 2960 – 2971, 2005.

[100] W. Burchard and W. Richtering, "Dynamic light scattering from polymer solutions," in *Relaxation in Polymers* (M. Pietralla and W. Pechhold, eds.), vol. 80 of *Progress in Colloid & Polymer Science*, pp. 151–163, Steinkopff, 1989.

[101] H. Endo, M. Mihailescu, M. Monkenbusch, J. Allgaier, G. Gompper, D. Richter, B. Jakobs, T. Sottmann, R. Strey, and I. Grillo, "Effect of amphiphilic block copolymers on the structure and phase behavior of oil–water-surfactant mixtures," *The Journal of Chemical Physics*, vol. 115, no. 1, pp. 580–600, 2001.

[102] B. Lindman and U. Olsson, "Structure of microemulsions studied by NMR," *Berichte der Bunsengesellschaft für physikalische Chemie*, vol. 100, no. 3, pp. 344–363, 1996.

[103] O. Söderman and U. Olsson, "Dynamics of amphiphilic systems studied using NMR relaxation and pulsed field gradient experiments," *Current Opinion in Colloid & Interface Science*, vol. 2, no. 2, pp. 131 – 136, 1997.

[104] F. Roosen-Runge, M. Hennig, F. Zhang, R. M. J. Jacobs, M. Sztucki, H. Schober, T. Seydel, and F. Schreiber, "Protein self-diffusion in crowded solutions," *Proceedings of the National Academy of Sciences*, vol. 108, no. 29, pp. 11815–11820, 2011.

[105] P. Greenspan, E. P. Mayer, and S. D. Fowler, "Nile red: A selective fluorescent stain for intracellular lipid droplets," *Journal of Cell Biology*, vol. 100, pp. 965–973, Jan. 1985.

[106] M. Stuart, J. van de Pas, and J. Engberts, "The use of nile red to monitor the aggregation behavior in ternary surfactant-water-organic solvent systems," *Journal of Physical Organic Chemistry*, vol. 18, no. 9, pp. 929–934, 2005.

List of Publications

1. C. Schulreich, C. Angermann, S. Hoehn, R. Neubauer, S. Seibt, R. Stehle, A. Lapp, A. Richardt, A. Diekmann, and T. Hellweg, "Bicontinuous microemulsions with extremely high temperature stability based on skin friendly oil and sugar surfactant," *Colloids and Surfaces A: Physicochemical and Engineering Aspects*, vol. 418, pp. 39-46, 2013.

2. R. Neubauer, S. Hoehn, C. Schulreich, Martin Dulle, Alain Lapp, and T. Hellweg, "Diffusion of proteins in a bicontinuous microemulsion: Controlling crowding effects by composition", *in preparation*

3. R. Neubauer, S. Hoehn, C. Schulreich, S. Seibt, and T. Hellweg, 'Protein diffusion in a system crowded with monodisperse spheres", *in preparation*

Abbreviations

APG©	alcylpolyglycosides
CMC	critical micell concentration
DFPase	diisopropyl-fluorophosphatase
DLS	Dynamic Light Scattering
FCS	fluorescence correlation spectroscopy
FFEM	freeze fracture electron microscopy
GFP	Green Fluorescent Protein
GFP+	improved Green Fluorescent Protein
NSE	neutron spin echo
mCherry	fluorescent protein derived from Discosoma sp
PFG-NMR	pulsed-field-gradient nuclear magnetic resonance
SANS	small angle neutron scattering
SAS	small angle scattering
SAXS	small angle X-ray scattering

Erklärung zur Dissertation

Hiermit erkläre ich, dass ich diese Arbeit selbständig verfasst und keine anderen als die von mir angegebenen Quellen und Hilfsmittel benutzt habe.

Ferner habe ich nicht versucht, anderweitig mit oder ohne Erfolg eine Dissertation einzureichen oder mich der Doktorprüfung zu unterziehen.

Bayreuth, 28. Februar 2013

Ralph Neubauer